

NSTX-U FY2012 Year End Report

J. Menard, M. Ono, and the NSTX-U Research Team

October 4, 2012 – Version 10

Table of contents

• Summary of FY2012 Notable Outcome	2
• Facility and Diagnostics	3
• Research Results – FY12 Milestones	12
○ R(12-1): Magnetic braking physics for rotation control at low v^*	12
○ R(12-2): Project deuterium pumping using lithium and cryo-pumping	16
○ R(12-3): Simulate confinement, heating, and ramp-up of CHI start-up	22
• Additional Research Highlights	29
○ Boundary Physics	29
○ Materials and PFC Research and Development	53
○ Macroscopic Stability	60
○ Transport and Turbulence	80
○ Energetic Particles	94
○ Wave Heating and Current Drive	99
○ Advanced Scenarios and Control	108
• NSTX-U FY2012 Publications	112

Summary of FY2012 Notable Outcome

The notable outcome for NSTX Program management for FY2012 was to: “Actively manage the utilization of NSTX scientific staff on domestic and international collaborations during the NSTX shutdown.” In preparation for maximizing the productivity of the NSTX research team during the Upgrade outage, outreach to other facilities to identify collaboration opportunities began in March 2011. Presentations were solicited and given by program leaders from DIII-D, Alcator C-Mod, MAST, KSTAR, and LHD. Additional opportunities on EAST and smaller facilities such as Pegasus, LTX, and QUEST in Japan were identified during the fall of 2011. Following identification of a wide range of collaboration opportunities, NSTX researchers (both PPPL and non-PPPL) were asked to identify primary and back-up collaboration topics and to establish research contacts on other facilities. In late 2011, the team was given guidance by the NSTX program and project managers for goals to strive for during collaboration. In particular, collaborations should aim to support the NSTX-Upgrade mission, but also support toroidal physics generally, ICCs, and non-fusion applications. All researchers were asked to view the Upgrade outage as an opportunity to extend and improve ongoing and future research on NSTX, learn about other facilities, bring back knowledge and best practices, and try to learn new physics, diagnostics, and analysis techniques. It was also recommended that researchers aim to form small teams from NSTX and coordinate research plans, analysis, travel, and participation. Researchers were requested to aim for first author publications and invited talks and to present results periodically at NSTX and PPPL research seminars. A key challenge for these collaboration activities was that no additional NSTX funding dedicated to collaboration was provided. However, by working closely with the PPPL off-site research department, strong collaborative activities were supported on DIII-D, C-Mod, KSTAR, and EAST.

With the assistance of NSTX program management, many successful collaboration activities were carried out by NSTX researchers and are described in the NSTX-U FY2012 year-end report. For example, on DIII-D, polarimetry was tested by UCLA for application to NSTX-U magnetic field fluctuation measurements, a DIII-D snowflake divertor configuration was demonstrated for the first time, joint experiments on RWM kinetic stability were carried out, and proxy error-field analysis was performed. On EAST, a lithium granular injector for ELM pacing which was successfully demonstrated and will be utilized on NSTX-U, lithium coating persistence and cryo-pumping effectiveness were measured, NSTX researchers assisted in achieving ICRF-only H-mode plasmas, aided gas-puff-imaging analysis of edge turbulence, and contributed to the design of a multi-energy SXR system for EAST with application to NSTX-U. Collaboration on C-Mod, KSTAR, and other facilities is also described in the NSTX FY2012 year-end report. MAST collaboration was limited in 2012 due to limited MAST operation, but expanded collaboration on MAST is planned for the 2013 run campaign.

NSTX-U FY2012 Year End Report: Facility and Diagnostics

NSTX started the FY 2012 NSTX upgrade outage on Oct. 1, 2011 six months earlier than the original schedule due to the TF electrical short that occurred in FY 2011. After a review by a panel of external magnet experts, the lessons learned on the soft solder flux issue which led to the TF failure was incorporated into the NSTX center-stack upgrade manufacturing process to prevent similar failures for NSTX-U. This early outage start offers an opportunity to accelerate the NSTX Upgrade Project schedule by up to six months. At the start of the outage, the NSTX diagnostics were carefully removed with proper documentation and were stored or shipped to the collaborating institutions as requested. After properly securing the NSTX facility, the NSTX operations technical staff shifted to Upgrade project tasks as rapidly as possible. The NSTX technical staff also supported the NSTX-U infrastructure refurbishments including fault detector and firing generator for rectifier controls, migration of the plasma control system to modern processors, and realignment of the Multi-Pulse Thomson Scattering (MPTS) system. The NSTX technical staff also supported outgoing collaboration activities including lithium granular injectors and droppers on EAST, RFX, and DIII-D. The NSTX Upgrade Project has made excellent progress in FY 2012. The NSTX Upgrade Project team successfully obtained DOE OFES CD-3 approval in Dec. 2011 on schedule. Upgrade project activities are ramping up rapidly in all areas and are currently on pace to be completed in mid-2014 well ahead of the Sept 2015 CD-4 completion target. To provide capabilities needed to carry out the NSTX-U scientific research, the NSTX Team identified high priority facility and diagnostic enhancements for post upgrade operations. These include diagnostics provided by NSTX Research Team members from U.S. laboratories other than PPPL. To facilitate the planning process, facility and diagnostic enhancement brainstorming meetings were held and many innovative ideas were proposed. A theory brainstorming meeting was also held, and this motivated discussion on future experiments and diagnostic needs.

Base Facility and Diagnostics Achievements for FY2012

Facility Milestone F(12-1): Receive CD-3 approval for NSTX-U. (January 2012)

Milestone F(12-1) Report:

The NSTX Upgrade Project to design and construct a new center-stack and a second more tangentially injecting neutral beam injector made excellent progress during FY 2012. After the successful final design review in June 2011 followed by a CD-3 (Critical Decision -3) Readiness Review, CD-3 approval was granted in December 2011 on schedule. In FY2012, having successfully completed all design tasks and obtained the CD-3 approval, the NSTX Upgrade Project began major fabrication and procurement activities. The diagnostics around the machine were removed and stored. The existing center-stack and associated components have been removed from the NSTX device. The project has begun work on the critical path fabrication of the center stack (CS) components including friction stir welding of lead extensions to the inner TF conductors. The procurement of critical and long lead items are being carried out including the center stack plasma facing components, inner PF coils, the center-stack casing, and other TF/OH materials. The 2nd NBI vessel window frame is being completed, and equipment including

racks within the 2nd NBI beam box footprint was removed. The NBI vacuum vessel components are being readied and the FCPC (power system) upgrade has begun during this period. The device support structure enhancement has begun and the new access ports for Bay J, K, and L are being installed, and the 2nd NBI beam box was relocated to the NSTX Test Cell in September 2012.

Center Stack Diagnostics: The center stack (CS) diagnostics provide key information on discharge parameters to characterize NSTX plasmas and guide NSTX operations. They also include sensors for machine protection. The diagnostics on the vacuum side of the CS include thermocouples, Mirnov coils, halo current Rogowski coils, and tile-mounted Langmuir probes. The sensors on the air side of the CS include flux loops and Rogowski coils for measuring the plasma current. Fabrication of the Mirnov coils was completed. The task first involved the fabrication of 80 MACOR cores or mandrels, which were twice the number originally required. A subsequent Lehman review specified the need for additional sensors to provide non-axisymmetric measurements of the halo currents through the CS. The NSTX-U project accommodated the requirement for more sensors by using the extra mandrels to wind a total of 45 coils in the direction of the major mandrel axis (“1D coil”), and 30 coils in both this direction and the axis orthogonal to it (“2D coil”). The additional coils provide spatially-localized signals around the CS, and include redundant sensors to improve the reliability of measurements along the CS axis. Plasma current and halo current Rogowski coils were also fabricated. The new CS can accommodate an additional plasma current Rogowski coil, so three of them were wound for NSTX-U. Continuous halo current Rogowski coils were constructed to encircle the CS, as on NSTX, at three locations. A set of Rogowski coils, however, was made in shorter segments for spatially-localized data at a fourth CS location to enable non-axisymmetric halo current measurements. The CS tiles were designed to include modified tile-mounted Langmuir probes (LPs). They will be machined after the CS tiles are received at PPPL. The new LPs are the same as the flush-mounted type originally used in NSTX, but with smaller diameters. This allows more LPs per tile, and permits increased spatial resolution. The coverage of the divertor region is also increased in NSTX-U, since LPs are located in the vertical as well as horizontal tiles at the top and bottom of the CS. All of the wires were procured for the thermocouples (TCs), flux loops, and connections (“field wiring”) between the Mirnov coils and LPs and their corresponding vacuum feedthroughs. The TC set includes “fast” thermocouples for rapid temperature measurements of the horizontal divertor tiles during plasma operations. One of the main sources of sensor failure in NSTX was damage to the field wiring due to limited space between the tiles, and also their sharp corners. These problems have been mitigated in the NSTX-U tile design with larger channels for the wires, and better chamfering of the tile edges.

Facility Milestone F(12-2): Identify possible high priority facility enhancements for post upgrade operations. (September 2012)

Milestone Description: To prepare for the post upgrade operations, the NSTX program will consider possible key facility enhancements in all of the science areas. An important facility enhancement in the boundary physics area is the divertor heat and particle handling enhancement for higher power long pulse operations. This may include expanded moly-tile divertor coverage and a more closed divertor geometry utilizing a cryo-pump. The HHFW antenna enhancements may be considered which could include an antenna limiter upgrade to handle higher power and

longer pulse NBI power and to accommodate high level of lithium evaporation, the antenna Faraday shields with a less transparent design maybe considered to better shield the antenna radiating elements. In the non-inductive plasma start-up area which is crucial for the ST based fusion nuclear science facility, the most promising approaches will be considered including an extension of the presently tested Coaxial Helicity Injection (CHI) system and implementation of the gun injection approach being developed on PEGASUS. For those NSTX-U facility enhancements, the decisions to proceed will be made by the end of FY 2012 taking into account the NSTX experimental results, available resources, and the established priority order.

Milestone F(12-2) Report:

There are a number of important facility related enhancements which are needed to take full advantage of the NSTX-U device capabilities. In preparation for the NSTX-U operations and for the 2014-18 Five Year Plan, the NSTX-U facility enhancement brainstorming meeting was held on Feb. 7 and 8, 2012. Many innovative ideas were proposed. In the area of solenoid-free start-up, a graphite tile overhang design was developed to cover the exposed stainless steel surfaces in the CHI gap to handle the much higher anticipated heat loads. The plasma gun start-up system is being developed by the PEGASUS group. A multi-MW-class 28 GHz ECH/EBW system is also considered for the start-up, ramp-up and non-inductive current maintenance research in NSTX-U. Addition of a MA-class ECH system should improve the start-up and subsequent ramp-up by HHFW and NBI by increasing the electron temperature of start-up plasmas. The 28 GHz tube being developed by the Tsukuba group is now running at ~ 1 MW level so it should be useful for NSTX-U. Another encouraging result is that the sapphire window is shown to be capable of supporting 2 MW, ~ 5 sec operation planned for NSTX-U, substantially reducing the cost of the tube. For the next generation tube, a design is being developed to increase the tube power toward 2 MW and the pulse length to 5 sec, which would be well suited for NSTX-U.

For boundary physics, a conceptual level design was performed on a closed divertor cryo-pump system. The initial indications are promising for providing divertor pumping for a relatively broad divertor parameter space including the snow-flake configuration. While the baseline NSTX-U operation plan is to start with graphite tiles, we are investigating the possibility of installing the moly tiles manufactured in FY 2011 on the upper in-board divertor region of NSTX-U to test their effectiveness in reducing the carbon impurity influx. If the moly tiles are deemed effective in reducing the carbon influx and compatible with the lithium/divertor operations, it is then logical to further expand the moly tile coverage in the divertor area for NSTX-U. Tungsten is also considered as a PFC material for NSTX-U. The QUEST group is testing an actively cooled tungsten limiter which uses a relatively inexpensive manufacturing technique to fuse a tungsten block to a copper base. It is encouraging that the new water cooled tungsten limiter enabled QUEST to increase their non-inductive operation from 37 sec to 180 sec without melting the tungsten limiter surfaces. For lithium capability, the base line is the dual upper (lower aiming) evaporators and droppers as in NSTX. A design will be developed for an upper aiming evaporator to cover the upper divertor region. The lithium granular injector for ELM pacing which was successfully demonstrated on EAST will be available for NSTX-U. Various concepts are being considered for liquid lithium divertor system. A flowing liquid lithium loop R&D facility (LDRD funded) is being built at PPPL. If successful, the design will

be adapted for NSTX-U. The HT-7 tokamak is also testing liquid lithium PFCs.

For MHD research, the massive gas injector disruption mitigation system will be implemented while the resonant field amplification (RFA) / resistive wall mode (RWM) sensors will be enhanced. For a longer term upgrade, the non-axisymmetric control coil (NCC) system is being considered and a conceptual design of NCC is being developed. In the high harmonic fast wave (HHFW) area, antenna enhancements are being performed to enable the HHWF feed-thru conductor to handle the higher disruption loads ($\sim \times 4$) in NSTX-U. A HHFW poloidal limiter upgrade to handle higher power and longer pulse NBI power is also considered for NSTX-U. For MHD and Advanced Scenario areas, the real time plasma control system will require continued improvements including new processors which is being implemented as noted below.

Diagnostic Milestone D(12-1): Identify possible high priority diagnostic enhancements for post upgrade operations. (September 2012)

Milestone Description: To prepare for post-upgrade operations, the NSTX program will consider possible key diagnostic enhancements in all of the science areas. In the Transport & Turbulence area, the high-k scattering system re-aiming will be investigated to measure both the radial and poloidal components of the high-k turbulence. To support advanced ST operations, a feasibility of implementing real time measurements of plasma pressure and current profiles will be investigated. In the energetic particle area, we will be assessing the need for additional energetic particle diagnostics in addition to the perpendicular and tangential fast ion D-alpha (FIDA) diagnostics. This may include additional SSNPA (Solid-State Neutral Particle Analyzer) channels as the scanning NPA will not be reinstalled for NSTX-U. For those NSTX-U diagnostic enhancements, the decisions to proceed will be made by the end of FY 2012 taking into account the NSTX experimental results, available resources, and the established priority order.

Milestone D(12-1) Report:

The NSTX-U diagnostic planning meeting was held in July 2011 and also in July 2012. Since the 2012-2016 non-laboratory NSTX-U diagnostic grant recipients were decided in FY 2012, they represent a significant fraction of the planned NSTX-U diagnostic capability. The diagnostics which were operational in FY 2011 are generally expected to be available for the NSTX-U operation unless otherwise noted. We note below those diagnostic systems which have strong collaboration components.

In the Transport & Turbulence research area, the high-k scattering system detector array presently located at Bay K will have to be relocated to Bay L after the 2nd NBI installation at Bay K. By re-aiming the microwave beam, it is possible to measure both the radial and poloidal components of the high-k turbulence. The high-k scattering system is being fabricated by the UC Davis group. The group plans to replace the existing 280 GHz system to ~600 GHz system. The higher frequency system is designed to improve high-k resolution and SNR. For low-k turbulence, the beam emission spectroscopy (BES) system with a new generation of BES detector has been developed by the University of Wisconsin group. The group is planning to expand the BES

system to 56 spatial channels. The UCLA group is also planning to install 288 GHz polarimetry system for magnetic fluctuation measurements. This system is presently being tested on DIII-D.

In the energetic particle research area, in addition to the perpendicular and newly implemented tangential fast ion D-alpha (FIDA) diagnostics by the UC Irvine group, additional SSNPA (Solid-State Neutral Particle Analyzer) channels will be implemented since the scanning NPA was removed. The UCLA group will be installing 16 channel reflectometry for the energetic particle mode measurements.

In the boundary physics research area, a major NSTX-U PMI diagnostic addition is the Material Analysis Particle Probe (MAPP) by Purdue University. MAPP is an in-vacuo inter-shot diagnostic capable of correlating surface chemistry evolution with plasma response to PMI conditioning. MAPP utilizes multiple surface-science measurement techniques to characterize a sample material exposed to NSTX-U conditions and assess plasma-surface interactions near the divertor strike point. MAPP includes a manipulator probe to insert a probe head with four samples that can be exposed to plasmas and withdrawn between plasma shots to characterize their surfaces. Techniques for surface analysis currently include: Thermal Desorption Spectroscopy (TDS), X-ray Photoelectron Spectroscopy (XPS), Low energy Ion Secondary Scattering (LEISS), and Direct Recoil Spectroscopy (DRS). The novelty with this design is the ability to apply three separate surface-sensitive characterization techniques promptly under the NSTX-U tokamak and without exposure to air. The NSTX-U MAPP system is being installed on LTX for further testing in preparation for the NSTX-U operations in collaboration with Purdue University. In the area of divertor spectroscopy, two new spectroscopic diagnostics will be installed to study the plasma surface interactions on the liquid lithium divertor by the LLNL group. A 20-element absolute extreme ultraviolet (AXUV) diode array with a 6 nm bandpass filter centered at 121.6 nm (the Lyman- α transition) provides spatially resolved divertor recycling rate measurements in the highly reflective LLD environment, and an ultraviolet-visible-near infrared $R = 0.67$ m imaging Czerny–Turner spectrometer enables spatially resolved divertor spectroscopic emission and ion temperature on and around the LLD module. The use of photometrically calibrated measurements together with atomic physics factors enables studies of recycling and impurity particle fluxes as functions of LLD temperature, ion flux, and divertor geometry. Another important divertor diagnostic recently developed is a two-color or dual-band device developed for application to high-speed IR thermography by the ORNL and University of Tennessee groups. Temperature measurement with two-band infrared imaging has the advantage of being mostly independent of surface emissivity, which may vary significantly for LLD as compared to that of an all-carbon first wall. For a longer term, a divertor Thomson scattering system will be pursued. A pre-conceptual design of a possible system has been performed.

For advanced ST operations, it maybe necessary to control the pressure and plasma current profiles which would require real time measurements of plasma pressure and current profiles. The JHU group is installing 96 channel edge and core tangential multi-energy-soft-x-ray arrays for fast time scale plasma profile measurements. Nova Photonics is implementing real time MSE which can give the real time plasma current profile information in addition to the MSE-CIF and MSE-LIF systems.

Other (Non-Milestone) Base Facility and Diagnostics Achievements for FY2012

Lithium Granules Injector for ELM Control:

The NSTX lithium granule injector (LGI) for ELM control has been completed in FY 2011. The LGI system was shipped to the Chinese Academy of Science, institute of Plasma Physics and installed on the EAST Tokamak. The NSTX LGI system is capable of injecting horizontally redirected spherical Lithium granules (0.6 mm) at speeds approaching 100 m/s. The dropping rates (pacing frequencies) of 500 Hz have been achieved in the laboratory test. A dropper apparatus allows the granule size to be changed between discharges. After an extended shake-down period, the injector was used to trigger/pace ELMs in EAST H-modes. Using Li granules with diameters of several tenths of a millimeter injected at speeds of several tens of meters per second, ELMs were triggered at high efficiency. Pacing frequencies ranging between 10's to 100's of Hertz were observed. It is anticipated that much higher pacing frequencies can eventually be achieved using similar injector technology. A similar LGI system was also sent to RFX in Italy and successfully commissioned. An NSTX lithium dropper was also shipped to DIII-D for divertor recycling control.

Ex-Vessel Diagnostics for NSTX-U Operations:

Modifications to the Multi-Pulse Thomson Scattering (MPTS) diagnostic required for the NSTX Upgrade were designed, and fabrication and procurement of the needed components were started. The larger diameter of the center stack in NSTX-U requires that the MPTS laser beams be re-aimed to avoid striking the center stack, which would cause damage to it as well as an unacceptable level of scattered laser light in the vacuum vessel [DIAG-1]. The re-aiming of the laser beams requires several other changes to the MPTS diagnostic configuration: 1) a new laser beam dump must be provided on a new vacuum vessel port structure on the opposite side of the vacuum vessel (Bay L) from the laser input port; 2) the laser input port on the vacuum vessel must be moved several centimeters on the vacuum vessel and re-aimed to achieve the needed laser beam path; and 3) the MPTS light collection optics must be modified and re-aimed to provide high-resolution imaging of the re-aimed laser beam. This new configuration is shown in Figure DIAG-1. Redesigning the MPTS system to meet these requirements was accomplished and a successful preliminary design review was held. A successful final design review for the modifications to the vacuum vessel was held, and final design reviews for the remaining modifications to the system are planned for early FY13. The new port structure required for the laser beam dump is located at Bay L and includes ports for several other diagnostics. The reconfigured MPTS diagnostic will be installed prior to NSTX-U first plasma and commissioned in early experimental operation following first plasma.

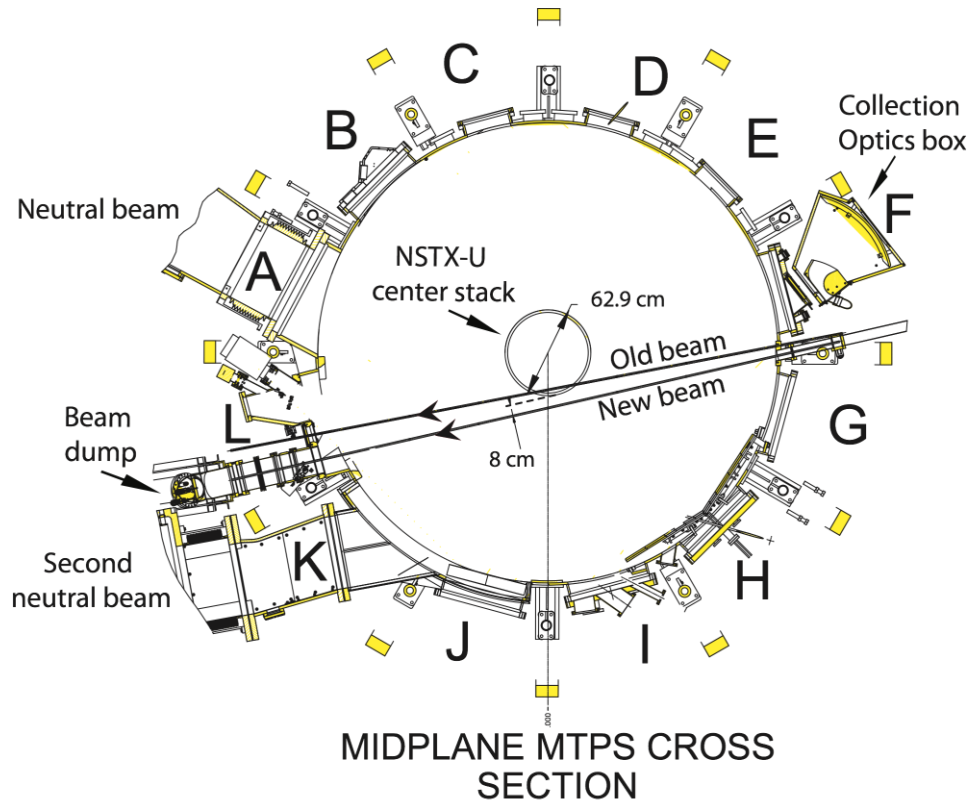


Figure DIAG-1: Midplane cross section of NSTX-U showing old and new MPTS laser beam paths, relocated laser input port on the vacuum vessel, new beam dump, and scattered light collection optics box (from Ref. DIAG-1).

The addition of a second neutral beam as part of the NSTX Upgrade results in a loss of vacuum vessel port space for diagnostics. To take full advantage of available port space a new plan for allocation of the ports to the diagnostics was developed. Ports with the required diameter, field of view, and orientation were identified for all the key diagnostics required for the first year of experimental operation following first plasma.

The high- k microwave scattering diagnostic, for example, has provided valuable measurements of plasma turbulence in NSTX. However, the scattered microwave collection optics were located at the port that will be used for the second neutral beam in NSTX-U and therefore can not remain in that location. To preserve the high- k microwave scattering diagnostic, the system was redesigned to make use of a new receiving window on the new port structure at Bay L. The new configuration of the diagnostic will allow turbulence in a different region of k - (wavenumber) space to be studied because it will provide turbulence measurements with more sensitivity to the poloidal component of k than for the previous system, which was primarily sensitive to the radial component of k .

Liquid Lithium R&D Facility:

Development of flowing liquid lithium PFCs and related technologies is underway at PPPL supported by the LDRD funding which if successful could be adopted to the NSTX-U liquid lithium divertor. The present efforts focus on a capillary-restrained system that incorporates gaseous cooling. In this conceptual diagram, “T-tubes” are considered for the active cooling scheme with either helium or super critical-CO₂ (s-CO₂) as the primary coolant. The PFC includes a porous or textured front face, similar to that used on LLD for liquid lithium stability against disruptive loads. Lithium flow channels are located parallel to the cooling channels with discrete ports to allow the liquid metal to wick quickly to the front-face. In addition to size scaling, an examination of the basic cooling fluid is also being carried out. S-CO₂ has been identified by many in the fission power industry as having favorable properties in a power cycle over helium. Experimental demonstration of liquid metal PFC concepts is currently underway to complement the design studies described above. These begin with the development of a liquid lithium loop which will provide active pumping into and out of vacuum chambers. The facility will be utilized for testing of candidate PFC designs to show such things as (1) stable operation and flow in a tokamak-relevant vacuum environment (10^{-7} to 10^{-6} Torr pressures), (2) restart capability after periodic shut-down and gettering of residual gases, (3) maintainability and reliability in addition to safe operation. Future plans include active purification of lithium inventory and upgrades to include integrated tests with s-CO₂ cooling systems.

Laboratories for Material Characterization and Surface Chemistry:

NSTX-U is collaborating with two new laboratories established at PPPL in collaboration with Princeton University dedicated for materials characterization and surface chemistry experiments. The Surface Science and Technology Laboratory is equipped with three surface analysis systems and an ultrahigh vacuum deposition chamber. Substrates for vapor deposition of metal films can be heated and cooled from 85 – 1500K using liquid nitrogen cooling and resistive and electron-beam heating. These systems have a variety of surface diagnostics, including high resolution electron energy loss spectroscopy (HREELS), which is capable of probing both optical and vibrational excitations over a wide range of 0 - 100 eV with an electron energy resolution of 3 meV, alkali ion-scattering spectroscopy (ALISS), and angle-resolved X-ray photoelectron spectroscopy (XPS). Another instrument has XPS, low energy ion scattering (LEIS), and reflection high-energy electron diffraction (RHEED) capability for thin film growth studies. In this laboratory, the time evolution of the chemical composition of lithium surfaces exposed to typical residual gases found in tokamaks was recently measured. Solid lithium samples and a TZM alloy substrate coated with lithium have been examined using XPS, temperature programmed desorption (TPD), and Auger electron spectroscopy (AES) both in ultrahigh vacuum conditions and after exposure to trace gases. Lithium surfaces near room temperature were oxidized after exposure to 1-2 Langmuirs ($1L=1\times 10^{-6}$ torr s) of oxygen or water vapor. The oxidation rate by carbon monoxide was four times less. An important result of the measurements for NSTX-U is that lithiated PFC surfaces in tokamaks were found to be oxidized in about 100 s depending on the tokamak vacuum conditions which is much less than a typical time duration between the tokamak plasma shots. A second laboratory, the Surface Imaging and Microanalysis

Laboratory, contains a high-performance field emission Auger and multi-technique surface microanalysis instrument with a field emission electron source and lateral resolution of 30 nm for elemental analysis of surfaces of samples on the micro and nano scale.

Rectifier Control Refurbishments: Fault Detector and Firing Generator:

Due to the aging D-site rectifier infrastructure and greater power demands expected for NSTX-U, refurbishments of the TF and PF rectifiers will be performed from within the base program. The NSTX-U PF coil power configurations for day 1 operations have been agreed upon, and engineering work packages to implement are being developed. The TFTR-era rectifier control in the field coil power system rectifiers is being upgraded with a new fault detector and a firing generator. A prototype firing generator has been successfully power tested. Parts for the production units were procured, and the assembly of the new firing generators for the NSTX-U power supplies has started. A prototype field coil power conversion system fault detector is ready to be tested. Installation and test procedures for the prototype fault detector are being developed and reviewed. Strategies for the re-commissioning of the field coil power conversion system are being developed.

Migrate Plasma Control System to Modern Processors:

With the increased plasma control requirements for longer duration plasmas expected in NSTX-U, an upgrade to the existing plasma control system is being implemented. A new Plasma Control System (PCS) platform with increased capabilities (e.g., 64-bit operating system and ability to support additional I/O points and real-time algorithms) is being implemented for NSTX-U. A similar system will be also used for the Digital Coil Protection System (DCPS) for the Upgrade Project. The development of Plasma Control System Algorithms and Data Acquisition System protocols for the proposed power, gas, and magnetic diagnostic system configurations continued in FY 2012.

References

[DIAG-1] A. Diallo et al. Rev. Sci. Instrum. 83, 10D532 (2012)

NSTX-U FY2012 Year End Report: Research Results

In FY2012, the NSTX-U research team contributed experimental data and analysis in support of the 2012 DOE Joint milestone: *“Conduct experiments and analysis on major fusion facilities leading toward improved understanding of core transport and enhanced capability to predict core temperature and density profiles. In FY 2012, FES will assess the level of agreement between predictions from theoretical and computational transport models and the available experimental measurements of core profiles, fluxes and fluctuations. The research is expected to exploit the diagnostic capabilities of the facilities (Alcator C-Mod, DIII-D, NSTX) along with their abilities to run in both unique and overlapping regimes. The work will emphasize simultaneous comparison of model predictions with experimental energy, particle and impurity transport levels and fluctuations in various regimes, including those regimes with significant excitation of electron modes. Along with new experiments, work will include analysis of relevant previously collected data and collaboration among the research teams. The results achieved will be used to improve confidence in transport models used for extrapolations to planned ITER operation.”*

The NSTX-U contributions to the 2012 Joint Milestone are described in a separate report. Summary descriptions of the results of research milestones are provided below. Descriptions of additional selected research highlights are also provided.

FY2012 Research Milestone R(12-1): Investigate magnetic braking physics to develop toroidal rotation control at low collisionality (Target - September 2012. Completed – September 2012)

Milestone Description: Plasma rotation and its shear affect plasma transport, stability and achievable bootstrap current and thereby impact the performance of integrated ST scenarios. In order to explore the role of rotation in transport and stability, the physics governing the plasma rotation profile will be assessed over a range of collisionality and rotation by analyzing 2010 braking experiments with 3D fields as well as error fields produced by scrape-off-layer current (SOLC). The investigation will be performed on NSTX experimental data with density/fueling variation, pumping by lithium, and electron heating by high harmonic fast waves, as well as NSTX-U predicted scenarios based on TRANSP analysis, and new braking experiments in DIII-D and KSTAR. Key aspects of this study include the plasma response and neoclassical toroidal viscosity transport behavior to 3D fields at low collisionality and rotation. Experiments and NTV analyses will be compared with the IPEC and other 3D transport code calculations to improve predictability as well as self-consistency of plasma response modeling. The achieved understanding for magnetic braking physics will be the key to the development of simplified real-time rotation control algorithms, which will be tested in other devices and installed in NSTX-U, and to the optimization of the rotation profile for macroscopic stability including the resistive wall mode (RWM). To determine the optimal rotation profiles, RWM kinetic stability physics will be investigated using the MISK code with various NSTX cases, NSTX-U scenarios, and DIII-D and KSTAR experiments in a wide range of rotation and collisionality. In parallel, the computational capability and predictability of MISK for RWM physics will be strengthened via benchmarking with other codes such as MARS-K and HAGIS. Altogether, this research will provide the required understanding of rotation control and plasma stability critical for NSTX-U, ITER, and next-step STs.

Milestone R(12-1) Report:

Magnetic braking physics to develop toroidal rotation control at low collisionality

Understanding of magnetic braking physics has been largely improved and advanced calculations have been applied to NSTX and KSTAR. First the equivalence between the kinetic stabilization and the neoclassical toroidal viscosity (NTV) has been rigorously proved [R12-1-1], as can be simply represented by the relation, $T_{NTV} = 2in\delta W_k$. This work indicates the achieved understanding and techniques in either kinetic RWM [R12-1-2,3] or NTV physics studies [R12-1-4,5] can be cross-checked and actively utilized to each other. The work also implies the most important part in magnetic braking physics is to obtain the precise perturbed distribution function with distorted orbits on perturbed magnetic field lines.

Based on the implication, we successfully developed a particle simulation code, Particle Orbit Code for Anisotropic pressure (POCA) [R12-1-6], which will be separately described later, to achieve the precise \mathcal{F} without any approximation. The benchmark and the verifications have been performed in terms of every aspect in NTV, such as, δB^2 -dependency, neoclassical offset, superbanana plateau (SBP), bounce-harmonic resonances, etc. Results indicate the combined analytic formula for NTV [R12-1-5], can give a good qualitative guide and even a good quantitative prediction for conventional aspect-ratio tokamaks. For NSTX, the combined analytic theory can be qualitatively reliable within an order of magnitude. A large improvement can be made if the large-aspect-ratio expansion is removed in present formulation. In principle this will give the identical computation to MARS-K or MISK codes. Presently the numerical implementation has been finished and will be under benchmark with MARS-K.

The combined analytic treatment still can provide the fastest computation, and thus has been used to study the magnetic braking in various kinetic regimes of NSTX. Figure R12-1-1 shows the NTV variations in the wide range of the collisionality and rotation, by utilizing and scaling the kinetic profiles in #132725, which corresponds to ν_{exp} and ω_{exp} , when the n=1 and the n=3 RWM EF coil perturbations are used for magnetic braking. One can see different aspects between the n=1 and the n=3. For the n=1, magnetic braking becomes stronger when the collisionality is lower, but only in the particular range of the rotation. The particular range of rotation corresponds

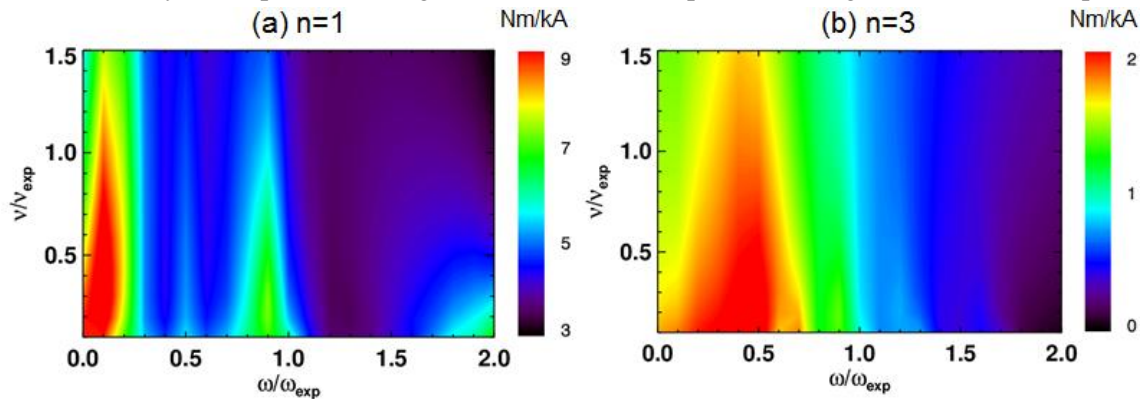


Figure R12-1-1: NTV torque variations vs. collisionality and rotation, for (a) n=1 and (b) n=3. One can clearly see each rotational resonance, SBP, and two bounce harmonic resonances for n=1, but those rotational resonances are collectively combined for n=3 in low rotation. In rotational resonances, NTV increases in low collisionality.

clearly to the SBP, the $\ell=1$, and the $\ell=2$ bounce harmonic resonance, respectively. This is qualitatively very similar to the RWM kinetic stabilization as found by MISK, which manifests the equivalence of the two physics again. For the $n=3$, high ℓ bounce harmonic resonances collectively influence on the magnetic braking, and effectively gives only one rotational resonance when the rotation is low. This is also highly consistent with the experimental observations with the $n=3$ [R12-1-7]. Results indicate the rotational resonances can be utilized to improve the magnetic braking, but should be carefully treated especially in the low collisionality NSTX-U plasmas. In near future, several important target plasmas for NSTX-U will be selected to perform the POCA calculations, to have quantitative predictions for detailed braking profiles.

The same technique has also been actively applied to KSTAR RMP experiments. In the RMP ELM control, it is considered that the magnetic braking effects should be minimized, to produce the sufficient stochastic layers in the edge while reducing the unnecessary neoclassical transport in the core. One can define a figure of merit by combining the two hypothesis, although the precise physics is yet to be determined, by

$F \equiv \sigma^4 / T$, where the σ is the width of the stochastic layer in the edge and T is the NTV torque. The definition is made to remove the δB -scale dependency, as $\sigma \propto \sqrt{\delta B}$ and $T \propto \delta B^2$. The IPEC and NTV analysis shows indeed the figure of merit is maximized in the successful ELM-suppressing RMP configuration (90 phasing) as shown in the Figure R12-1-2. Also, the actual magnetic braking has been observed in the midplane-alone RMP fields, by damping rate $\sim 1/s$, which is also consistent with our NTV damping prediction. In this KSTAR campaign, the first experimental demonstration of the bounce harmonic resonances will be attempted with the $n=1$ midplane RMP, based on these successful applications.

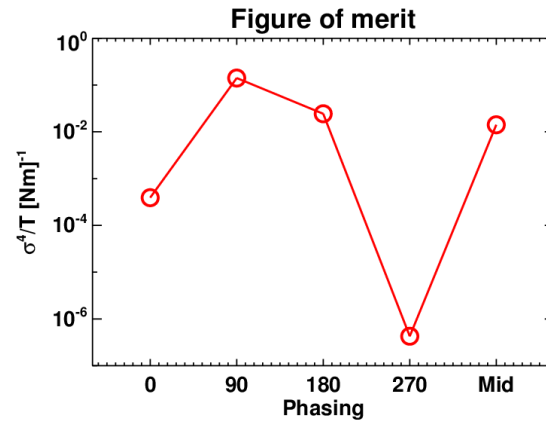


Figure R12-1-2: Figure of Merit factor showing the effectiveness of the stochastic transport in the edge vs. neoclassical transport in the core. The figure of merit is maximized in 90 phasing, which indeed the configuration that only demonstrated the ELM suppression.

The other important subject in magnetic braking physics is to have the reliable calculations of δB from perturbed tokamak equilibria. The IPEC has supplied the δB information to the various analytic formulas as well as to the POCA, but the applicability of this non-self-consistent δB calculation is limited especially in very high beta and with strong braking. Indeed the POCA simulation based on the IPEC field showed larger NTV than the observation, within a factor of 2, which may be due to the non-self-consistent δB without the self-shielding effects of the NTV torque itself. For the self-consistent δB calculation, the combined NTV formalism without the large-aspect-ratio approximation is being integrated to IPEC. Also, we showed the combined NTV formula is exactly identical to the MARS-K if the MARS-K is modified to handle the energy-dependent collisionality. Since the MARS-K is already capable of the self-consistent δB calculation, we will upgrade the MARS-K in parallel with the IPEC upgrade to the general

perturbed equilibrium code (GPEC). The two codes then will be cross-checked and under active benchmark to successfully achieve the self-consistency in $\delta\mathcal{B}$ calculations. Ultimately the POCA will be integrated to IPEC, as the POCA implementation is carefully designed for this future application.

References

- [R12-1-1] J.-K. Park, Phys. Plasmas 18, 110702 (2011)
- [R12-1-2] J. W. Berkery et al, Phys. Rev. Lett. 104, 035003 (2010)
- [R12-1-3] J. W. Berkery et al., Phys. Rev. Lett. 106, 075004 (2011)
- [R12-1-4] J.-K. Park et al., Phys. Rev. Lett. 102, 065002 (2009)
- [R12-1-5] S. Satake et al., Phys. Rev. Lett. 055001 (2011)
- [R12-1-6] K. Kim et al, Phys. Plasmas 19, 082503 (2012)
- [R12-1-7] S. A. Sabbagh et al., Nucl. Fusion 50, 025020 (2010)

Development of δf particle code for NTV calculation and its application to NSTX

A new δf guiding-center particle code, POCA (Particle Orbit Code for Anisotropic pressures) was developed to investigate neoclassical transport in the perturbed tokamaks. POCA tracks the guiding-center orbit motion and solves the Fokker-Planck equation in the presence of the non-axisymmetric magnetic field perturbations. Development and theoretical studies of POCA was recently published [POCA-1].

Benchmarking studies of NTV calculation with POCA have been performed compared with a generalized combined NTV theory [POCA-2]. Figure POCA-1 shows a comparison of NTV profiles between POCA and the theory when applying a single harmonic magnetic perturbation. Overall profiles show very good agreement and the amplitudes agree within a factor of 2. Strong peaks appear at the resonant flux surface and clearly indicate the resonant feature of NTV transport.

Theoretically predicted bounce harmonic resonance has been verified by POCA simulation, which can significantly enhance the NTV torque by resonance between the bounce orbit and electric precessions. A new

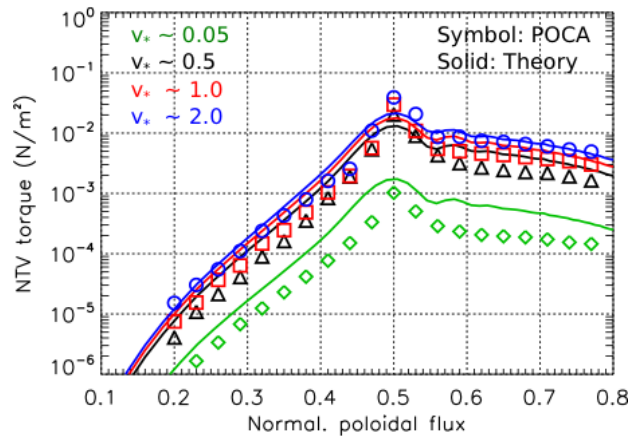


Figure POCA-1: Comparison of NTV profiles between POCA and combined theory in the various collisionalities.

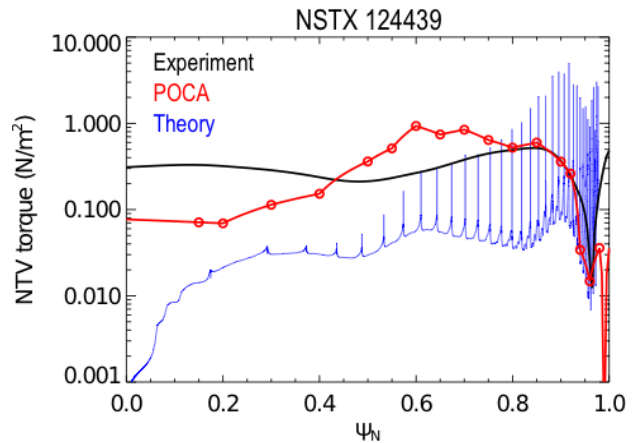


Figure POCA-2: Comparison of NTV profile among POCA, theory and experiment for a NSTX discharge 124439.

type of closed orbit by the resonance was discovered tracking the guiding-center orbit motion, and a significant enhancement of NTV by the resonance was demonstrated.

Experimental analysis of NTV using POCA has been carried out for NSTX magnetic braking experiments. The perturbed magnetic fields, calculated with IPEC including ideal plasma response, are coupled to POCA throughout a fitting using Chebyshev polynomials. Toroidal rotation measured by CHERS is used to calculate the electric potential. An analysis result is presented in Figure POCA-2, where the NTV torque profile in the experiment was inferred from toroidal rotation damping rate and neoclassical toroidal flow considering a neoclassical offset rotation. As shown, POCA shows a good agreement of NTV torque profile with the experiment, and provides an improved prediction. Total NTV torque by POCA is 4.5 Nm and agrees well with the experimental value, 3.5 Nm. Further analyses of NTV experiments using POCA are actively under way for NSTX and DIII-D, which will improve understanding of physics of NTV and magnetic braking.

References

- [POCA-1] J.-K. Park et al, Phys. Rev. Lett. 102, 065002 (2009)
[POCA-2] K. Kim et al, Phys. Plasmas 19, 082503 (2012)

FY2012 Research Milestone (R12-2): Project deuterium pumping capabilities for NSTX-U using lithium coatings and cryo-pumping. (Target - September 2012. Completed – September 2012)

Milestone Description: Access to reduced collisionality in NSTX Upgrade will be achieved with a combination of increased temperature from increased field and plasma current, and from operation with controlled and reduced normalized plasma density (Greenwald fraction). Key to achieving controlled and reduced normalized density is sufficient particle control. Lithium wall coatings have been utilized in NSTX to pump deuterium, and low deuterium Greenwald fractions of 0.3-0.5 have been achieved and maintained for the full flat-top duration of NSTX. However, the lack of ELMs with thick lithium coatings can lead to increased carbon confinement and Zeff and higher total Greenwald fraction ~1 (all of which can be reduced with natural or triggered ELMs). A key question for the usage of lithium coatings in NSTX-U is the deuterium pumping persistence of the coatings, i.e. whether such coatings can pump throughout the entire flat-top of an NSTX-U plasma. To address this issue, modeling of the deuterium pumping from Li coatings in NSTX will be performed with edge codes such as SOLPS and UEDGE. These codes will be used to interpret and reproduce heat and particle flux profiles from high current and high beam-power discharges from NSTX to project scrape-off-layer profiles for NSTX-Upgrade. This SOL profile analysis will be combined with time-dependent analysis of divertor deuterium recycling with lithium in NSTX, and these trends will be used to project lithium pumping persistence in NSTX-U. A second deuterium pumping technique – divertor cryo-pumping – will also be assessed for NSTX-U. Preliminary cryo-pumping designs for NSTX-U will be developed compatible with the NSTX-U vessel geometry and a range of divertor magnetic topologies, including the snowflake divertor. Further, this analysis will be used to assess which NSTX-U operating scenarios and density values can be sustained with stationary deuterium inventory using cryo-pumping. This analysis and modelling for lithium coatings and cryo-pumping will provide a quantitative basis for projecting particle control in NSTX-U with application to future next-step STs.

Milestone R(12-2) Report

Cryo-pumping design for NSTX-U

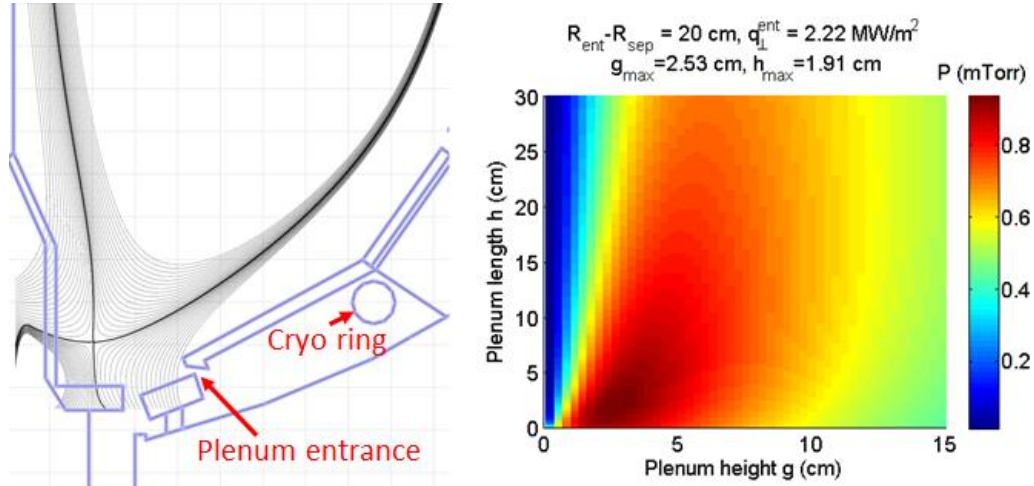


Figure R12-2-1: Schematic of cryo system, and example of projected plenum pressures used to optimize pump entrance.

A physics design study of a cryo-pumping system for the NSTX-Upgrade has been performed; the results of the design were presented at the PAC-31 meeting in April 2012 and will be presented at the APS-DPP meeting this fall. A semi-analytic pumping model [R12-2-1] was used in this effort, and extended to include the effect of finite plenum throat length on achievable neutral pressure. Recent NSTX experiments measuring the scaling of the divertor heat flux profile, as well as measurements of the electron temperature in the far SOL were used in this model to provide a semi-empirical projection of the pumping performance of candidate cryo geometries, as illustrated in Figure R12-2-1.

This model was used to optimize the length, height, and radial position of the plenum entrance. Using the optimized entrance parameters, the achievable plasma density has been estimated by assuming a balance between neutral beam fueling and the pumped flux, and combining this with a two-point model for the SOL to relate the upstream and line-averaged density to the divertor density at which this balance is achieved. Pumping in the optimized configuration has been tested over a wide range of plasma position relative to the cryo pump and flux expansion, and the

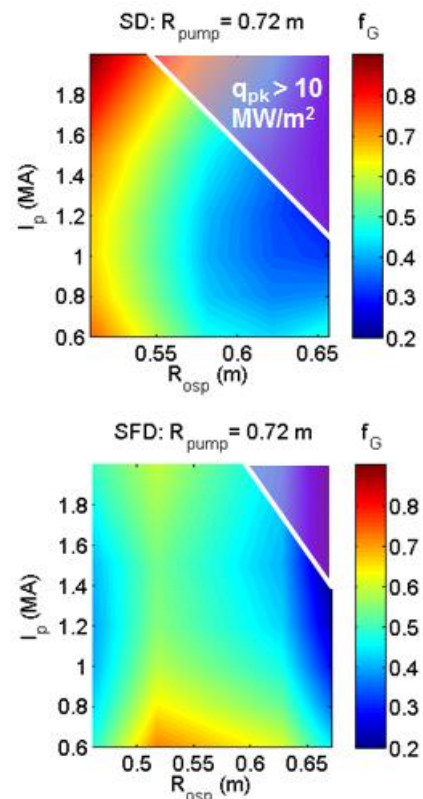


Figure R12-2-2: Projected density achievable for various R_{osp} in standard and snowflake divertor configurations.

modeling indicates that low plasma densities ($f_G \sim 0.5$) can be achieved over a broad range of configurations. Notably, the cryo-pump is found to be compatible with the high flux expansion Snowflake divertor, and in fact performs better in this configuration. Due to the improved power handling capability in this configuration, the allowable operating space with simultaneously sufficient pumping and low peak heat flux is larger with a Snowflake divertor. In the future, this work will be extended by using 2D plasma-neutrals modeling to evaluate pumping efficiency in radiative/detached regimes (which are not captured by the semi-analytic model used).

Persistence of pumping by lithium coatings

The ability of lithium coatings to pump throughout a discharge has been studied through modeling of the PFC recycling during several time points in a discharge. Previously, the experimental edge profiles at the midplane combined with the measured divertor heat flux and D_α profiles were used to constrain the PFC recycling coefficient in 2D modeling using the SOLPS code [R12-2-2,3]. This work has been extended by performing modeling for multiple time slices within the same discharge. The results are summarized in Figure R12-2-3. The midplane SOL n_e and T_e profiles, as well as the peak divertor heat flux and D_α emission are all approximately constant over the time frame considered. Consistent with this, the modeling indicates that the

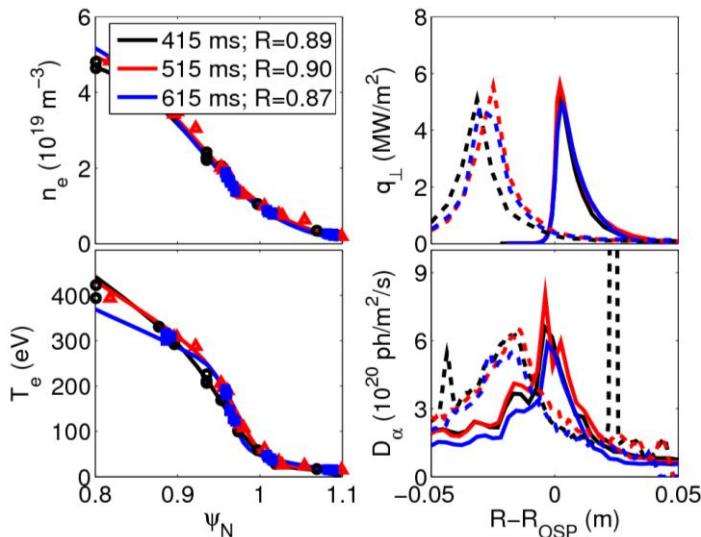


Figure R12-2-3: Measured (points and dashed lines) and modeled (solid lines) midplane and divertor profiles for three time slices of 129038. Inferred R_{PFC} is indicated in legend

PFC recycling coefficient remains at a relatively low level of ~ 0.9 over the three time slices (and in fact is reduced to 0.87 at the final slice, due to a slight reduction in the D_α emission). This indicates that, over the time frame considered (up to $t \sim 0.7$ s) the lithium coatings remain sufficiently activated to pump, with no evidence of saturation. These results were presented at the Plasma Surface Interaction (PSI) meeting in the spring of 2012, with a corresponding paper submitted to the Journal of Nuclear Materials.

Collaboration on EAST studying lithium pumping persistence

As the only other diverted H-mode tokamak in the world fusion program using lithium coatings as a means of particle and impurity control, the EAST tokamak can provide important data for understanding the pumping persistence of lithium coatings in a tokamak environment. In June 2012, several NSTX researchers led and participated in experiments to assess the particle pumping capabilities of lithium coatings in EAST. A supersonic molecular beam injector (SMBI)

was used for precise density feedback control and to modulate the gas fueling to measure particle pump-out times in L-mode plasmas heated with lower hybrid waves. Divertor Langmuir probe data was also taken to measure ion saturation current response to the gas fueling, and the saturation current decay-rate trends (related to local divertor recycling rates) were found to be consistent with the global pumping trends as indicated by the total SMBI fueling required to maintain constant line-average electron density. The global density and local/divertor pump-out measurements were obtained for a variety of configurations including upper single null, double null, and lower single null, and up-down asymmetries in global pumping rates were evident.

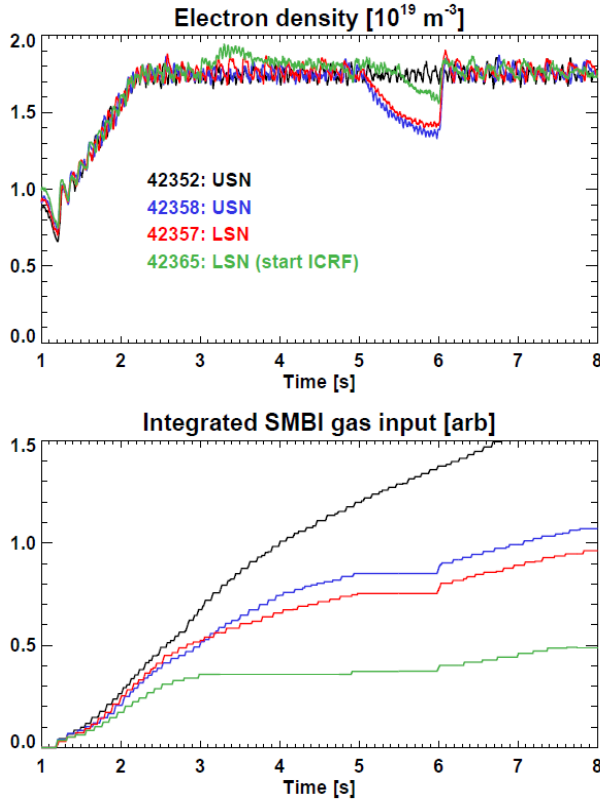


Figure R12-2-4: (Top) EAST line-average electron density vs. time and shot-number, and (bottom) integrated SMBI gas fueling needed to maintain the requested density.

improve understanding for both EAST performance optimization and to aid extrapolation to NSTX-U. For example, even if the lithium pumping degradation rate is increased by an order of magnitude by higher density in H-mode, the pumping efficiency would still only be reduced by 25% at the end of a 5s discharge in NSTX-U.

Strike-point variations were also performed in EAST both with and without cryo-pumping for LSN discharges, and the results indicate the density pump-out is a very sensitive function of the strike-point position in the divertor. It was observed that variations as small as a few cm changed the global pumping rate by up to a factor of two. These results from EAST will be further analyzed in the near-term and could influence the choice of plenum height gap for the divertor cryo-pumping system proposed for NSTX-U as described above.

The lower panel of Figure R12-2-4 shows the integrated SMBI fueling required to maintain constant density decreased by ~40% within 6 shots as evident from comparing the 2 USN plasmas. This result implies degradation of very strong pumping by lithium after 6-8 shots which corresponds to 60-80 total shot-seconds. Further, by comparing the first USN (42352) to the last LSN (42365), the lithium pumping is reduced by roughly a factor of 2 after 13 shots. Finally, lithium pumping reached ~3-4 times lower but nearly stationary values after 25 shots (250 total shot-seconds). These results imply an effective e-folding time for the global lithium pumping of ~18 shots or ~180s of accumulated shot time. Future lithium pumping persistence experiments on EAST will be proposed in beam-heated H-mode regimes and at higher density to

Progress of MAPP: Materials Analysis Particle Probe

The Materials Analysis Particle Probe (MAPP) [R12-2-4] has been designed to allow for the prompt analysis of plasma-facing components exposed to NSTX-U discharges (see Fig. R12-2-5). It is expected that MAPP will play a very important role in NSTX-U operation for understanding the evolution of lithium coatings in addition to other surface chemistry effects. MAPP is part of a four-part endeavor, along with post-mortem tile analysis, atomistic simulations [R12-2-5], and controlled laboratory experiments [R12-2-6], that aims to decipher the fundamental physics and chemistry occurring at the plasma-facing surface. Up until now, examining the influence of plasma-surface interactions (i.e., surface chemistry, retention, etc.) on first wall materials required either post-mortem tile analysis or offline laboratory experiments. These “offline” methods provide valuable insights on fundamental phenomena, however lack in several key areas including: 1) the ability to discern the effects of individual plasma discharges, 2) monitor the evolution of PFC chemistry over a campaign, and 3) prompt analysis of PFCs.

A unique sample head has been designed for MAPP to allow simultaneous exposure of up to four samples to plasma discharges (see Fig. R12-2-6).

The surface of each sample is positioned (via shims or custom machining) colinear to the top surface of the retaining stems in order to avoid self sputtering. Independently controlled heaters are contained beneath each sample and radiative and conductive cross-talk heating is reduced using perforated sample stems and vertical heat baffle shields.

Following plasma exposure, samples are retracted *in-vacuo* into an adjoining chamber, where a variety of analysis techniques are performed during the in-between shot window. Analysis

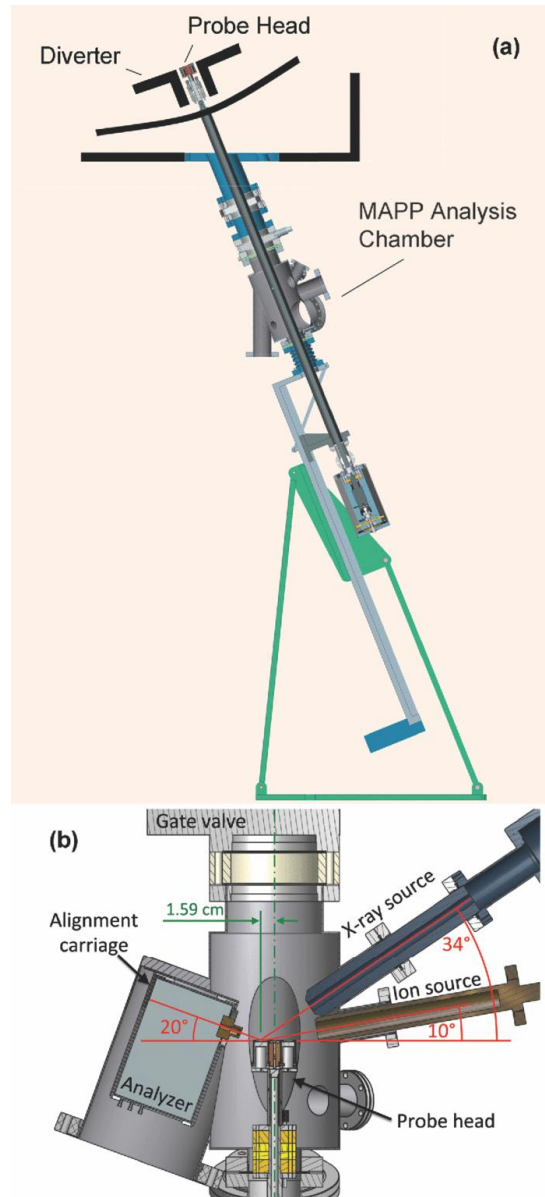


Figure R12-2-5: (a) The MAPP chamber connects to the bottom bay port of NSTX. (b) Following plasma exposure, samples are retracted *in-vacuo* to be analyzed using a suite of diagnostics that include XPS, ISS, DRS, and TDS. See text for details.

techniques include X-ray photoelectron spectroscopy (XPS) – used to assess the chemical interactions of the top ~10 nm, ion scattering spectroscopy (ISS) – interrogates the top 1-2 monolayers to determine surface chemical composition, and direct recoil spectroscopy (DRS) – uniquely capable of measuring the surface hydrogen content in samples. In addition, thermal desorption spectroscopy (TDS) can be performed at the end of each day in order to measure and quantify bulk deuterium retention.

The MAPP design considered operating under dedicated XP's but more importantly operating in 'piggy-back' mode. In the latter, MAPP operation is constrained to the in-between shot window, performing a suite of analyses unobtrusively as a diagnostic for the primary experiment. Dedicated experiments will be used for MAPP experiments that either require operational times exceeding the in-between shot window or to examine plasma characteristics that may not be available in other XPs.

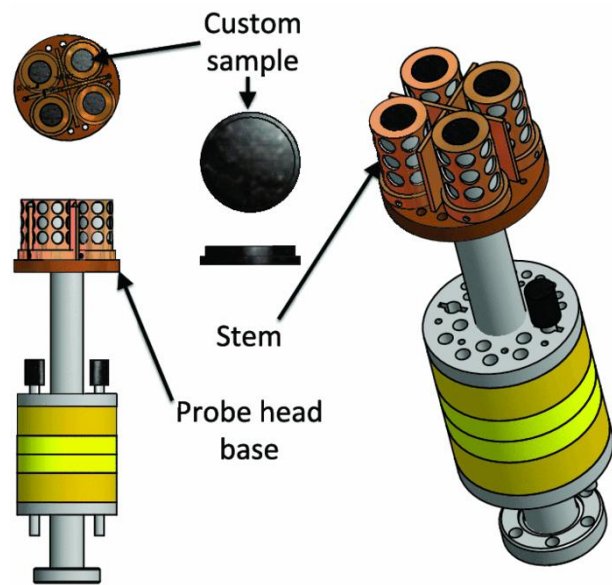


Figure R12-2-6: Four samples can be mounted to the MAPP head for exposure to NSTX-U plasma discharges.

References

- [R12-2-1] R. Maingi *et al*, Nucl. Fus. **39** (1999) 1187.
- [R12-2-2] R. Scheider *et al*, Contrib. Plasma Phys. **46** (2006) 3.
- [R12-2-3] J.M. Canik *et al*, J. Nucl. Mat. **415** (2011) S409.
- [R12-2-4] C.N. Taylor *et al.*, Rev. Sci. Instrum. **83**, 10D703 (2012)
- [R12-2-5] P. S. Krstic *et al.*, Fusion Eng. Des. (in press) doi:10.1016/j.fusengdes.2011.07.009.
- [R12-2-6] C. N. Taylor *et al.*, J. Appl. Phys. **109**(5), 053306 (2011)

FY2012 Research Milestone R(12-3): Simulate confinement, heating, and ramp-up of CHI start-up plasmas (Target - September 2012. Completed – September 2012)

Milestone Description: Elimination of the ohmic heating (OH) solenoid is essential for proposed ST-based nuclear fusion applications. Coaxial helicity injection (CHI) is a leading candidate method for plasma initiation without an OH solenoid. Understanding CHI plasma formation and sustainment is important for projecting non-inductive start-up and ramp-up efficiency to next-steps. CHI initiated plasmas have been successfully coupled to induction in H-mode plasmas with Neutral Beam Injection (NBI) heating. While these results are favorable, fully non-inductive plasma current ramp-up has not yet been achieved and is a major research goal of NSTX Upgrade. The Tokamak Simulation Code (TSC) has been successfully used to simulate CHI plasma formation, and these simulations will be extended with systematic variations of plasma transport parameters and other plasma parameters such as current, temperature, and density to study how NBI couples to these plasmas with low and zero loop voltage. These studies will inform the requirements for CHI plasma parameters for direct coupling to NBI. TRANSP calculations will also be performed using selected cases from TSC simulations to improve estimates for NBI heating and current drive profiles. Finally, optimized CHI target plasmas will be used as target plasmas for NBI ramp-up modeling using the present and 2nd NBI of NSTX Upgrade. High-Harmonic Fast Wave (HHFW) and (more recently) NBI heating of low-current ohmic targets have been demonstrated in NSTX and will be assessed in these modeling activities. This milestone will inform the early plasma and auxiliary heating and current drive requirements for non-inductive start-up and ramp-up for NSTX Upgrade and for next-step ST facilities.

Milestone R(12-3) Report:

CHI Start-up and Current Ramp-up modeling using TSC

TSC is a time-dependent, free-boundary, predictive equilibrium and transport code. It has previously been used for development of both discharge scenarios and plasma control systems. It solves fully dynamic MHD/Maxwell's equations coupled to transport and circuit equations [SFPS-1,2]. It is now being used for full non-inductive start-up and current ramp-up modeling in support of NSTX-U research. As a first step it has been used to study the importance of CHI discharge electron temperature during the plasma start-up phase. The peak electron temperature of NSTX CHI discharges is typically 25 eV, with peak temperatures up to 50 eV having been measured [SFPS-3, 4]. The observed decay time of the current from its peak is on the order of 20 ms, similar to expectations for classical resistivity at those temperature calculated with TSC.

In order to ramp up the plasma current with neutral beam injection after CHI in NSTX-U, both the CHI-produced toroidal current and the electron temperature in the CHI plasma need to be increased to confine the beam ions and to increase their slowing-down time on the electrons, respectively. Electron Cyclotron Resonance (ECH) heating at a power level of about 1.0 MW should be capable of boosting the initial electron temperature of the low-density CHI plasma to a few hundred eV. Experience on NSTX has shown that its HHFW heating can rapidly the boost the electron temperature of a 300 kA, 300 eV discharge to over 1 keV [SFPS-5]. This would produce a target with low density and high electron temperature well suited for neutral-beam current drive.

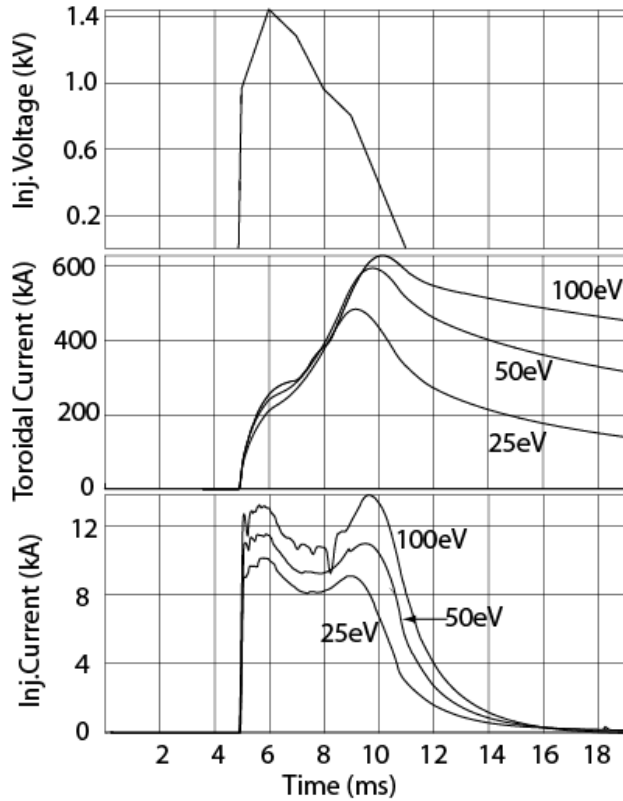


Figure SFPS-1: Injector voltage, CHI produced toroidal current and injector current for CHI discharges with electron temperatures of 25, 50 and 100 eV.

It is also possible that a further reduction of low-Z impurities, such as for example through the use of full metallic divertor plates or full lithium coverage of the divertor plates or a higher temperature vessel bake-out, or a combination of these methods, may naturally increase the electron temperature of CHI discharges. To assess the benefit of electron temperature on CHI discharges we have run simulations with the TSC code in which the electron temperature is increased from 25 eV to 50 eV and 100 eV, such as could be expected from an efficient electron heating system. The results in Figure SFPS-1 show that for the same applied injector voltage, the initial CHI generated current increases with increasing electron temperature. For the present NSTX injector flux conditions, the peak toroidal current increases to over 600 kA at 100 eV and drops to below 500 kA at 25 eV. An

examination of the injector current trace shows that the increase in toroidal current is due to an increase in the injector current, which must increase because the plasma resistivity is lower at the higher electron temperature. In addition, as could be expected the current decay time rapidly slows down at an electron temperature of 100 eV [SFPS-6].

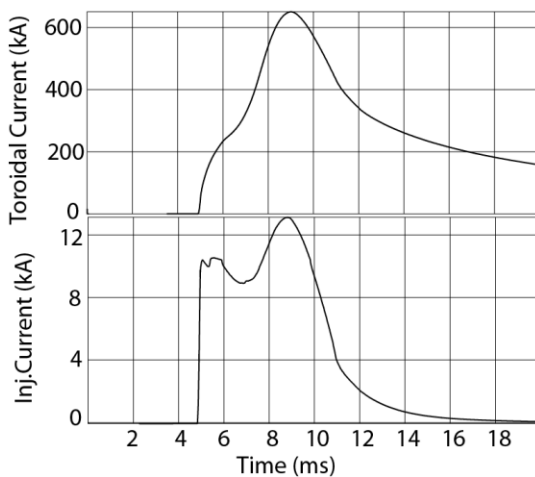


Figure SFPS-2: Toroidal current and injector currents for the 25 eV case shown in Figure SFPS-1, but with the applied voltage increased by 25%.

Figure SFPS-2 shows that at the lower electron temperature of 25 eV, the initial higher toroidal current could be reestablished if the injector voltage is further increased, in this case by 25%. The additional voltage compensates for the increased resistivity at the lower electron temperature and increases the injector current back to the levels required to generate the 600 kA target. However, as shown by the toroidal current trace, the current decay would remain rapid.

Note that at 9 ms, the peak toroidal current is over 600 kA, similar to the 100 eV case shown in Figure SFPS-1. However, later on in time, the current decay rate is similar to

the 25 eV trace shown in Figure SFPS-2. This shows that simply operating the external CHI circuit at a higher voltage is not sufficient to obtain a discharge that persists for a longer time. It is also necessary to heat the discharge to increase its temperature during the current decay phase so that more time is available for the neutral beam ions to couple to the decaying discharge. The detailed modeling of ECH heating of a CHI target is presented in the report section on wave heating and current drive.

These simulations indicate that the CHI system on NSTX-U would benefit from a higher voltage as this provides an important capability for optimizing the discharge evolution. These results also indicate that NSTX-U CHI discharges could significantly benefit from an efficient electron heating system and such a capability may be quite important for NSTX-U to demonstrate direct coupling to neutral beam current drive and thus to demonstrate the possibility for eventual elimination of the solenoid.

NSTX-U researchers have recently conducted the first ever simulations of a full discharge with non-inductive start-up with CHI and subsequent non-inductive current ramp-up using neutral beams in support of planned experiments on NSTX-U. In initial results presented below, a CHI discharge is initiated by TSC as described in Reference [SFPS-2], and a 600kA target is generated. The first step involves current driven by the external injector circuit on purely open field lines. During this phase after the open field line discharge fills the vessel, the applied CHI voltage is rapidly reduced. The resulting rapid decrease in the injector current and the rapidly decaying poloidal flux induces within the open field line CHI discharge a positive loop voltage that causes the generation of closed field lines. At the onset of flux closure a second step in the simulations locates and keeps track of the divertor X-point. After the generation of closed flux surfaces, the flux surface averaged transport equations are solved. This final phase begins 17ms after the CHI discharge is first initiated.

The initial electron temperature for the CHI discharge is 100eV. This is a reasonable starting value for the reasons described above in Figures SFPS-1 and 2. The initial electron density is assumed to be $3 \times 10^{18} \text{ m}^{-3}$, similar to the densities obtained during CHI start-up in NSTX [SFPS-3,4]. The initial plasma internal inductance is also below 0.5, also as calculated by EFIT for CHI discharges in NSTX [SFPS-3,4]. However, transiently, at about 200ms it increases to 1.35. Beyond 500ms it is maintained at about 0.4 for the rest of the discharge. The initial transient is probably because the CHI discharge is rapidly decaying in current and possibly related to the very low level of confinement (less than 1ms during this period) used in these initial simulations.

At 17ms, horizontal position control is implemented and at 55ms vertical position control is used to vertically center the up/down asymmetric CHI plasma. The electron transport is adjusted to keep the energy confinement time well below 25ms. During the low density phase of the discharge the RF power is increased to 2.5MW. This is assumed to be from a combination of 0.5MW absorbed ECH power and 2MW of absorbed HHFW power. Neutral beams are added in increments to keep the current overdrive at acceptable levels, as TSC is not capable of handling the generation of current holes. After the current has built up to sufficient levels, both the density and neutral beam power are ramped-up. Figure SFPS-3 shows the results from this first evolving discharge, which at $t=6\text{s}$ is still increasing in current.

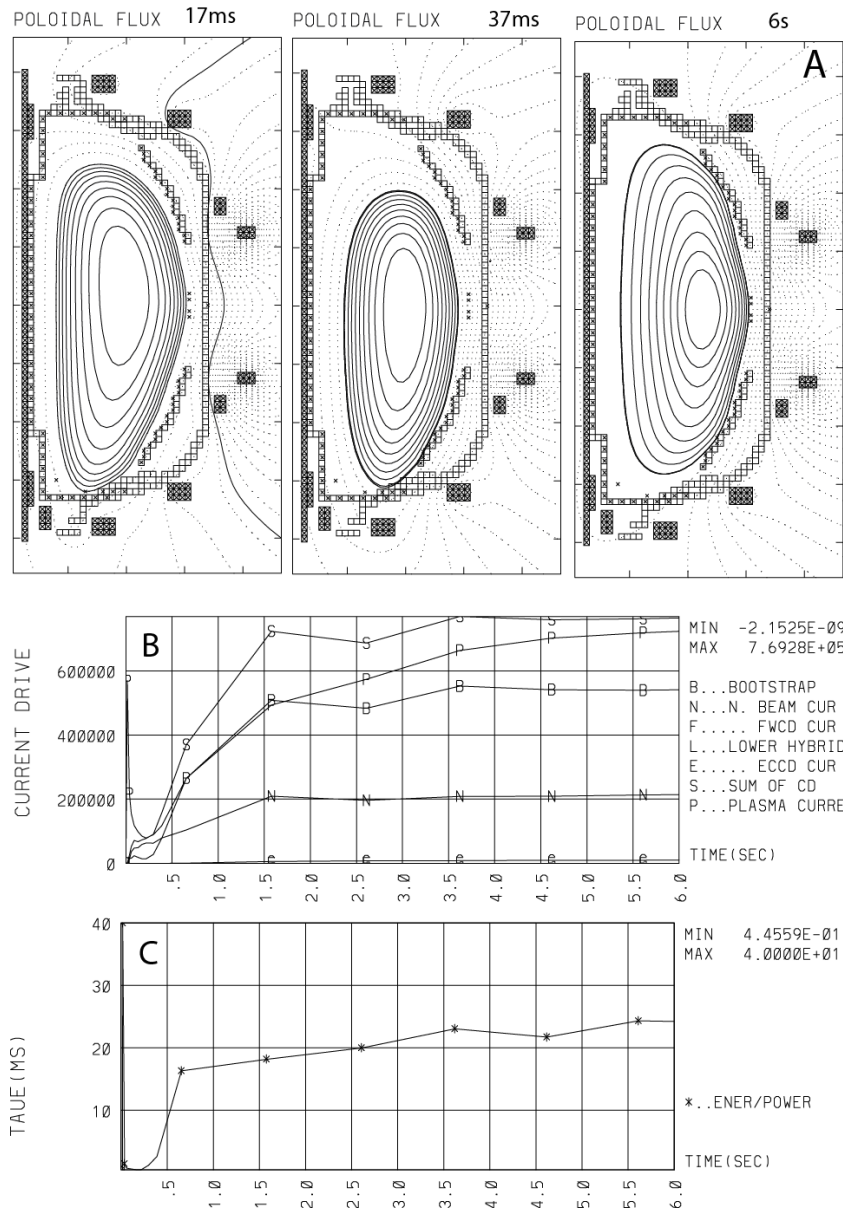


Figure SFPS-3: Shown are TSC simulation results of a full non-inductive discharge plasma start-up using CHI and current ramp-up using neutral beam and bootstrap current drive. (A) Poloidal flux contour at the end of the CHI-only phase at 17ms and at 37ms during the coupling phase and at 6s. (B) Plasma current traces including neutral beam and bootstrap current drive components. (C) The energy confinement time calculated with respect to input power.

CHI start-up modeling with NIMROD

Resistive MHD simulations using the NIMROD code are being used to model CHI start-up in NSTX; to improve understanding of the physics of injection, flux-surface closure, and current drive for CHI plasmas; and to extend these results to NSTX-U. During FY12 the NSTX model has been improved by comparison with experiment and exploration of simulation parameters.

Flux surface closure following the helicity-injection pulse has been demonstrated as seen in the Figure SFPS-5. Magnetic field-line tracing verified flux closure. Critical to the closure have been a 4-cm wide injection slot as used in the experiment and a rapid, monotonic voltage reduction at the end of injection. An X-point forms above the injection slot resulting in a separatrix surrounding a closed flux region. These results were obtained in an axisymmetric simulation indicating that resistive effects are important. A narrow current foot-print along the bottom boundary of NSTX (due to the narrow injection slot) is apparently needed for the reconnection generating this closure. The enclosed volume and toroidal current decay slowly following closure, although faster than experimental results. Ongoing, near-term research is directed to obtaining a larger volume of closed surfaces, to demonstrating improved quantitative comparison with experiment, and to determining the optimum conditions for closure.

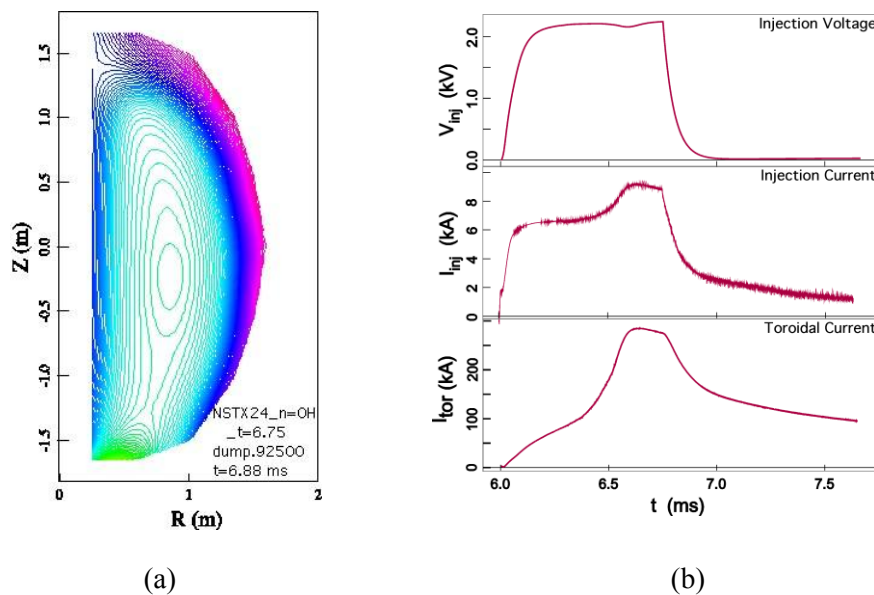


Figure SFPS-4: Flux surface closure for a simulation of a 4-cm wide injection slot. (a) “Fast” closure within 50 μ s after rapidly reducing the injection voltage. (b) Injector voltage and current; Toroidal current for (a).

References

- [SFPS-1] S.C. Jardin, N. Pomphrey, J. Delucia, J. Comput. Phys. **66**, 481-507 (1986)
- [SFPS-2] R. Raman, S.C. Jardin, J.E. Menard, et al., Nucl. Fusion **51**, 113018 (2011)
- [SFPS-3] B.A. Nelson, et al., Nucl. Fusion **51** (2011) 063008
- [SFPS-4] R. Raman, D. Mueller, T.R. Jarboe, et al., Phys. Plasmas, **18**, 092504 (2011)
- [SFPS-5] G. Taylor, et al., PPPL-4729, “Generation of high non-inductive plasma current fraction H-mode discharges by HHFW in NSTX” (2012)
- [SFPS-6] R.Raman, D. Mueller, S.C. Jardin, et al., IEEJ Transactions on Fundamental and Materials, Vol **132**, No. 7, pp462-467: DOI:10.1541/ieejfms.132.462 (2012)

ECH Modeling for NSTX-U

CHI discharges are typically characterized by having a very hollow electron temperature profile as shown in Figure ECH-1(a). A 1-2 MW, 28 GHz electron cyclotron heating (ECH) system is planned for NSTX-U. Initially the system will use short, 10-50 ms, 1 MW pulses to heat CHI start-up plasmas in order to significantly increase the core electron temperature [ECH-1]. The GENRAY [ECH-2] ray tracing numerical code, and the ADJ [ECH-3] Fokker-Planck numerical simulation were used to model second harmonic 28 GHz X-mode ECH in a NSTX CHI start-up plasma with an axial toroidal field, $B_T(0) = 0.5$ T (shot 148072). Figure ECH-1(a) shows the electron density and temperature profiles that were used for the GENRAY-ADJ modeling. In this case the electron temperature is only 5 eV near the magnetic axis. The central electron density is $4 \times 10^{18} \text{ m}^{-3}$ and the density profile is broad. As shown in Fig. ECH-2(b), 28 GHz microwave

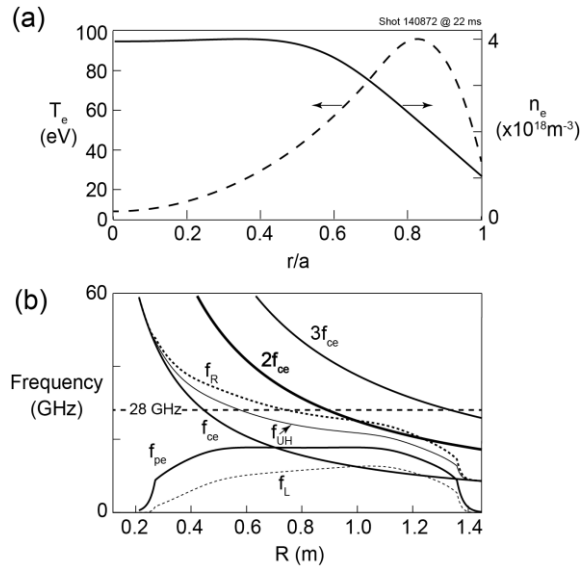


Figure ECH-1(a) Electron density (solid line) and temperature (dashed line) profiles used for the GENRAY-ADJ ECH modeling, derived from multi-point Thomson scattering data acquired at 20 ms during NSTX CHI shot 148072. (b) Electron cyclotron resonances and cutoffs on the midplane of shot 148072 calculated using magnetic equilibrium data at 22 ms and the density profile data of Fig. ECH-1(a).

power is resonant with the second harmonic electron cyclotron resonance ($2f_{ce}$) at a major radius (R) of 0.9 m. The right hand cutoff (f_R) is just below 28 GHz at $R = 0.9$ m.

100 rays were used for the GENRAY-ADJ modeling. The ECH antenna orientation was adjusted for maximum first pass absorption. Figure ECH-2 shows the ray trajectories calculated by GENRAY when the antenna was oriented for maximum first pass absorption; pointing 5 degrees down and 1 degree right of the normal to the ECH port. Figures ECH-2(a) and 2(b) show the rays projected onto the poloidal cross section and toroidal midplane., respectively. The power deposition profile is relatively narrow and located at a normalized

minor radius, $r/a \sim 0.17$ on the low field side of the magnetic axis (see Figure ECH-2(c)).

Figure ECH-3(a) shows the dependence of the first pass absorption on toroidal launch angle when the antenna is pointing 5 degrees down. The peak first pass absorption reaches 27% with the antenna pointed 1 degree from normal to the plasma surface, and falls to 10-15% as the toroidal angle is increased from 3 to 8 degrees. The actual absorption will probably be enhanced significantly by wall reflections. As the core electron temperature rises as a result of the ECH the first pass absorption will increase, reaching about 60-80% when the central temperature is 100-200 eV as shown in Figure ECH-3(b).

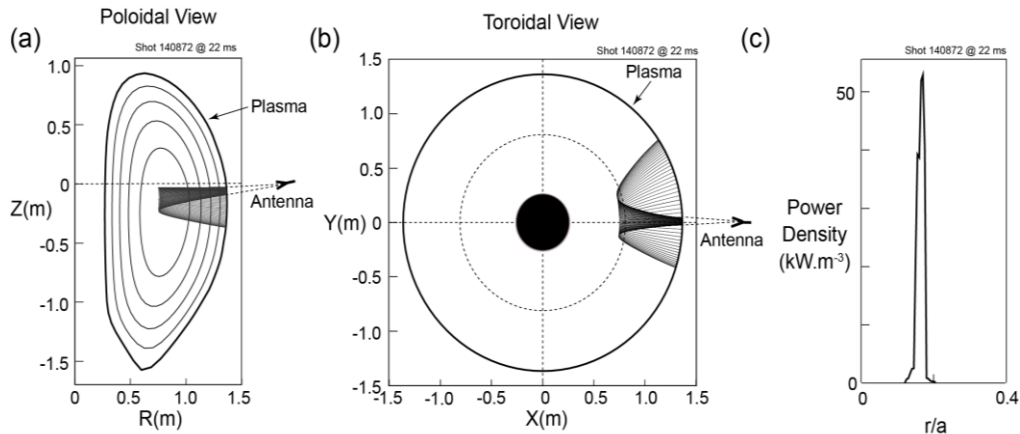


Figure ECH-2: Ray trajectories calculated by GENRAY plotted in (a) the poloidal and (b) the toroidal midplane for the case with maximum first pass absorption of 28 GHz ECRH at 20 ms during NSTX CHI shot 148072, with the antenna pointing 5 degrees down and 1 degree right of the normal to the ECRH port. (c) First pass power deposition profile versus normalized minor radius (r/a) calculated by GENRAY for 1 MW of 28 GHz.

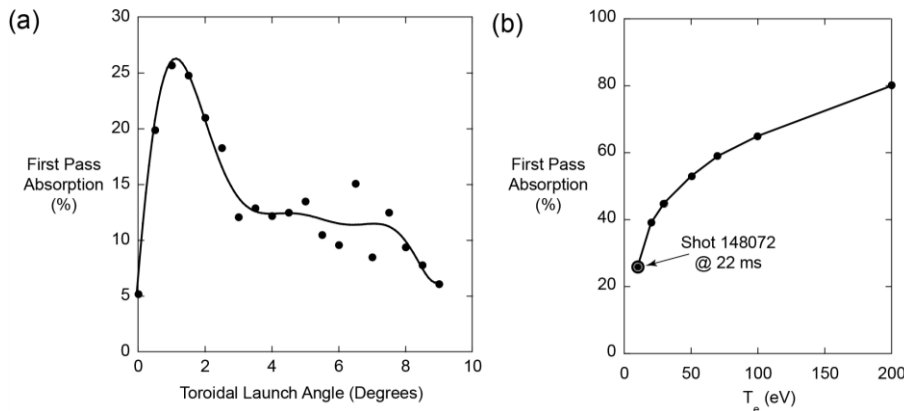


Figure ECH-3: (a) First pass absorption fraction plotted versus the toroidal angle between the antenna axis and the normal to the plasma surface when the antenna is pointing 5 degrees down, and (b) the dependence of first pass absorption on electron temperature when the antenna is pointing with a toroidal angle of 1 degree to the normal to the plasma surface and 5 degrees down.

References

- [ECH-1] G. Taylor, et al., *Proc. 17th Workshop on ECE ECRH*, EPJ Web of Conferences **32**, 02014 (2012) <http://www.epj-conferences.org/>
- [ECH-2] A. P. Smirnov and R.W. Harvey, *Bull. Am. Phys. Soc.* **40**, 1837 (1995)
- [ECH-3] A. P. Smirnov, et al., *Proc. 15th Workshop on ECE and ECRH*, World Scientific (2009), pp. 301-306

Additional NSTX-U Research Achievements in FY2012

Beyond the completion of the FY2012 research described above, additional important scientific results were obtained during the FY2012 period and are described below.

Boundary Physics Research Results

First observations of ELM triggering by injected lithium granules in EAST

Large transient events, including edge localized modes (ELMs), would be problematic for high power fusion devices, including ITER, because of the associated large, periodic heat loads on plasma facing components. Two methods to address this issue are elimination of large ELMs altogether with, e.g. 3-D magnetic perturbations, or controlled triggering of rapid, small ELMs for a manageable transient heat load. One proven method for ELM triggering involves injection of periodic, high-speed cryogenic deuterium pellets. The use of fuel pellets, however, introduces the prospect of increased plasma density; while recent research [BP-ELM-1] has nearly eliminated density increases, the flexibility to use pellet materials other than fuel is still desirable. In this paper, we report the first results of ELM pace-making with lithium granules accelerated into H-mode discharges at the outer midplane in the EAST device, using a rotary motor to impel a controllable velocity, and hence a controllable penetration depth.

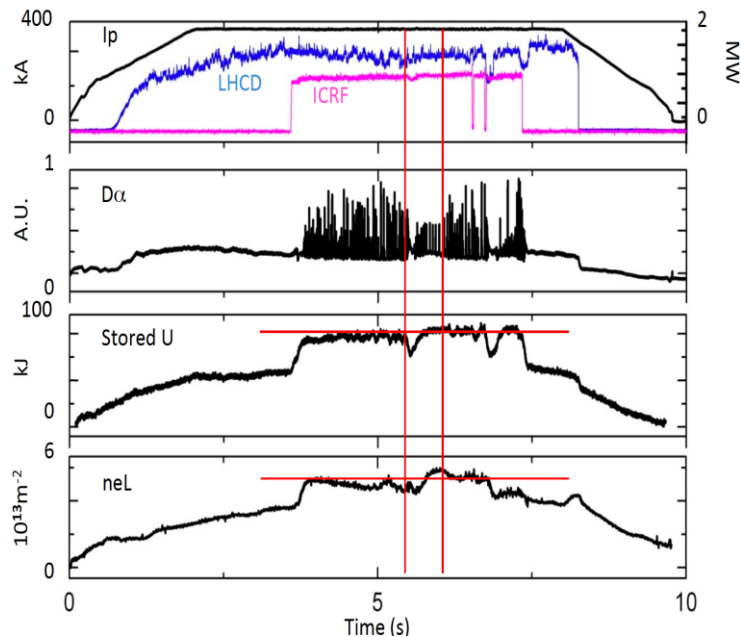


Figure BP-ELM-1: H-mode Discharge in EAST (with naturally occurring mixed Type I/Type III ELMs) into which lithium granules were injected for ~ 1 sec. Nearly every granule triggered an ELM, which became locked to the granule injection times.

Figure BP-ELM-1 shows an H-mode discharge in lower-single null configuration in the EAST device, with heating from both a lower hybrid current drive (LHCD) system and an ion cyclotron radio frequency system (ICRF). The discharge was in a naturally occurring mixed ELM regime, i.e. with both Type I and Type III ELMs. The 0.7mm size lithium granules were injected for ~ 1 sec at a 20-25 Hz repetition rate from ~ 5.4 - 6.4 sec, and these granule triggered ELMs with a nearly 100% efficiency (D_α spikes in between the vertical red lines). Following a brief H-L transition period after injection of the third granule, the H-mode was re-established with a modestly increased stored energy and line average electron density.

Figure BP-ELM-2 shows an expanded time region during the granule injection phase. Nearly every signal shown in Figure BP-ELM-2 reflects the granule injection; the edge soft X-ray (SXR) and Mirnov ('MHD') signals reflect the triggering of ELMs. The third granule followed a large, naturally occurring ELM, and triggered a brief H-L phase, indicated by the blue shaded area. Following resumption of H-mode, all of the observed ELMs except one were coincident with the lithium granule injection.

The pellet impeller motion and lithium granule acceleration was captured by a 16,000 frames/sec visible camera. Somewhat fortuitously, the granule ablation process timescale could be assessed because the ablation resulted in a transient but clear reflection on the impeller body. These reflections were observed only during ablation, and not during natural ELMs or MHD activity. From the known distance to the separatrix (~ 2 m), the average granule velocity was estimated at 52 m/s, in good agreement with the momentum imparted to the granule from the rotary motion of the impeller. Furthermore the penetration depth was also measured because the duration of the reflection had a definite, measureable timescale in the 400-900 μ sec range. Using the estimated granule speed, we compute a penetration depth past the separatrix of 2-5 cm, the minimum value of which is of order the pedestal pressure full width.

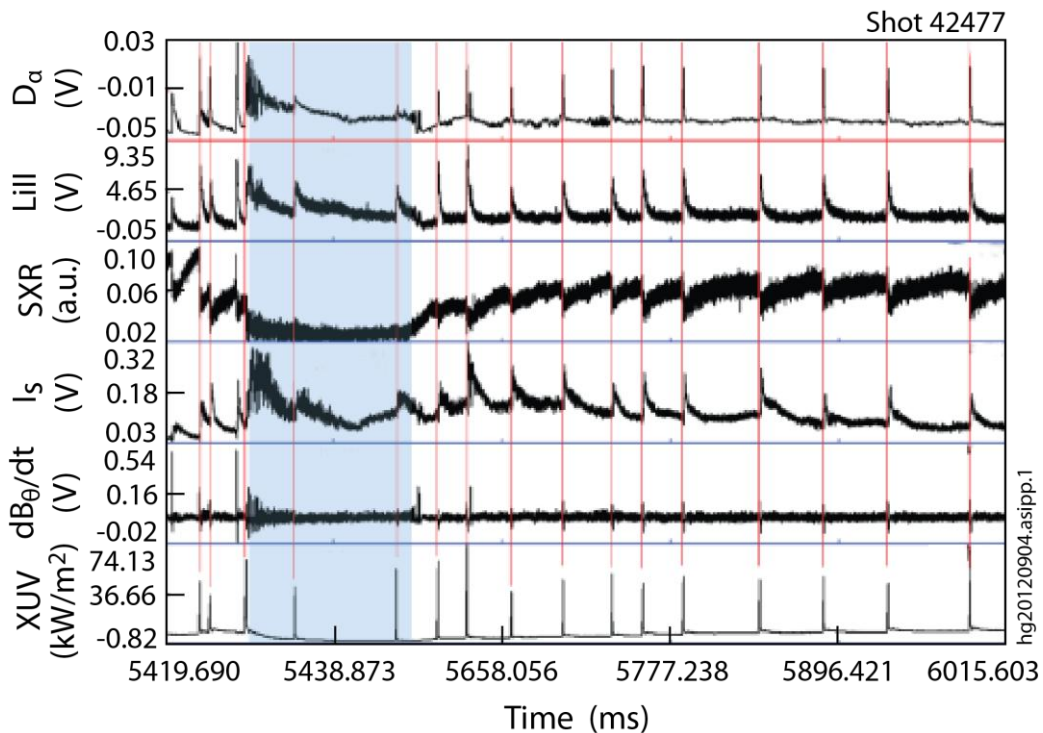


Figure BP-ELM-2: Expanded time base from Figure BP-ELM-1, showing timing of lithium granule injections (red vertical lines) and signatures on multiple diagnostics. The third granule at $t \sim 5480$ msec followed a naturally occurring ELM, and caused an H-L transition. After the discharge went back into H-mode, the ELM timing was locked to the granule injection times.

While this is the first observation of ELM triggering by lithium granules, substantial research is needed to assess the minimum penetration depth needed to trigger ELMs; this can be assessed by varying the impeller speed. In addition, the reason for occasional triggered H-L back transitions needs to be determined; we conjecture (based on very limited statistics) that those granules had deeper penetration than other granules. These research questions will be addressed in the next

EAST campaign in 2013. The system implemented in EAST is compact and relatively inexpensive, with a rotary motor attached to redirect ~ 100 mm lithium granules dropped vertically via an apparatus developed [BP-ELM-2] in NSTX. Granule injection frequencies up to 100 Hz have been achieved in the laboratory, with higher frequencies possible with higher speed motors. The frequency can be easily varied even during plasma discharges. Looking ahead to ITER or perhaps JET, beryllium spheres could be accelerated with a similar system to test ELM pace-making, in case lithium is undesirable. For NSTX-U, the rapid triggering of ELMs using lithium granules could be an effective means of impurity reduction in Li ELM-free H-modes.

Advances in pedestal equilibrium and stability theory and modelling for NSTX/NSTX-U

While the peeling-ballooning mode theory has shown reasonable success in explaining the ELM stability boundary on other tokamak devices, it has been less successful on NSTX. It was speculated by the edge theory group at PPPL that one possible reason for such a discrepancy is inaccuracy in the widely used Sauter bootstrap current formula in the steep edge pedestal in contact with the magnetic separatrix. The Sauter formula was developed only using the conventional core plasma profiles and magnetic geometry. In order to resolve this question, the neoclassical kinetic edge code XGC0 has been used to investigate the bootstrap current in

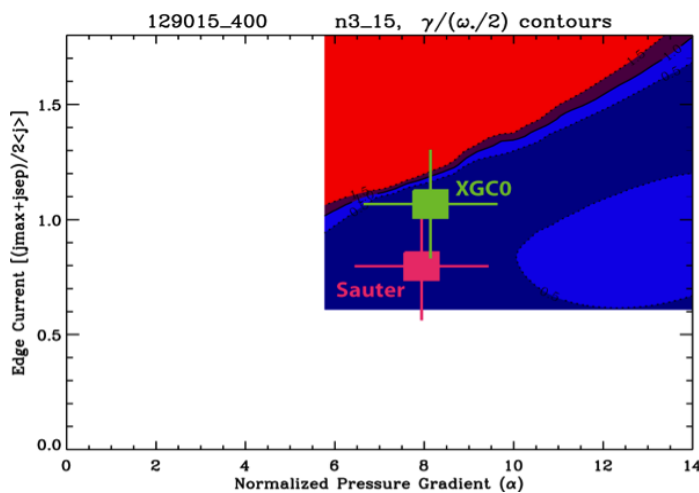


Figure BP-ELM-3: Elite stability boundary condition for NSTX 129015, compared to the kinetic EFIT results with Sauter vs XGC0-produced bootstrap current.

realistic tokamak edge geometry including the magnetic separatrix. It is found that, due to the smallness of the passing particle fraction and the strong poloidal inhomogeneity of the toroidal magnetic field, the bootstrap current in the NSTX pedestal is significantly greater than the Sauter value if the pedestal electrons are in the plateau-collisional regime. Based upon the XGC0 simulation result, a new analytic formula, as a modification to the Sauter formula, has been developed [BP-ELM-3]. When this new formula is used, the edge stability boundary in NSTX is found to be in reasonable agreement with the ELITE stability analysis results. Figure BP-ELM-3 shows the ELITE stability boundary plot compared to the kinetic EFIT results in NSTX plasma 129015 with Sauter vs XGC0 bootstrap current densities. It can be seen from the figure that the XGC0-based formula yields a good agreement within the error bar limit, while the Sauter formula yields a significant disagreement.

References

- [BP-ELM-1] L.R. Baylor, et al. Proc. 24th IAEA FEC, San Diego, CA, paper EX/6-2 (2012).
- [BP-ELM-2] D.K. Mansfield, et al., Fusion Engineering and Design 85, 890 (2010).
- [BP-ELM-3] S. Koh, et al., Plasmas 19, 072505 (2012).

Advances in pedestal turbulence theory and modelling for NSTX/NSTX-U

To gain some physical insights in the spatial characterization of the fluctuations observed in pedestal region from the newly installed BES system, we used the global gyrokinetic edge code XGC1 to study the ITG turbulence. The usefulness of a localized gyrokinetic simulation is highly limited in the edge pedestal since the radial correlation length is similar to or longer than the radial pedestal width. Realistic experimental profiles of 139047 are used, but Coulomb collisions were not turned on in order to study the collisionless physics first. For a clearer analysis under given experimental plasma profiles, XGC1 was operated in the delta-f mode, even though XGC1 normally operates in full-f mode in predictive simulations. Figure BP-XGC-1 displays a cross-section of the potential fluctuations in the non-linear stage of the simulation, which shows characteristic poloidal structures propagating in the ion diamagnetic direction. The ITG drive/source is found to reside at the pedestal top, but nonlinearly and nonlocally penetrates into the pedestal region. Sampling a region encompassing both BES and the reflectometer measurements (as indicated in the second panel of Fig. BP-XGC-1), one can estimate the equivalent radial and poloidal correlations as shown in the third panel of Fig. BP-XGC-1. The correlation is obtained from band-pass filtered potential fluctuations to mimic the BES frequency window. A good agreement is obtained. Poloidal correlation length of approximately 11 cm is obtained from simulation, compared to 12 cm from BES. Radial correlation length of

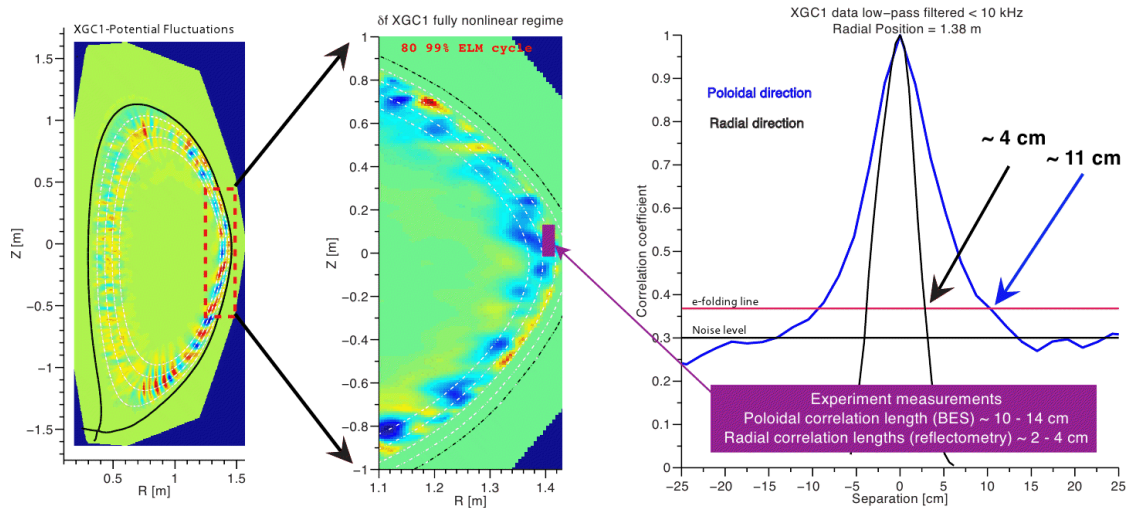


Figure BP-XGC-1: (left) potential fluctuations in the pedestal region as computed by XGC1, (right) turbulence radial and poloidal correlation lengths from XGC-1.

approximately 4 cm is obtained from simulation, compared to 3 cm from BES. Future simulations will include possible modifications by the Coulomb collisions, by the addition of kinetic electrons and by multiscale interaction with background neoclassical flows.

Progress on the characterization of fluctuations and transport in the pedestal region

In FY 2012, NSTX researchers characterized the spatial scales of the fluctuations at play in the pedestal during the inter-ELM phase. Identifying the spatial scales between ELMs is a current research topic, as it will provide the physics basis for predictive capabilities of the pedestal height and width. The work performed focused on high performance discharges with type I ELMs. The diagnostics utilized were the BES system for the poloidal scales and the reflectometer system for the radial scales [BP-PED-1]. Both systems provide density fluctuation spectra in the pedestal region.

Results indicate that fluctuations with spatial scale $k_{\perp} \rho_i < 0.2$ are present in the pedestal region as shown in Figure BP-PED-1. In addition, these fluctuations spatial scales are found to be anisotropic and shown to propagate in the ion diamagnetic direction. These results seem to point to ion-scale fluctuations of the type ITG/TEM or KBM. While a complete identification of these fluctuations remains difficult, preliminary simulations using a full-f XGC1 have been performed (see above). Preliminary XGC1 simulations show fluctuations of the potential (fully nonlinear) localized at the pedestal top with estimated poloidal correlation of 11 cm, radial correlation length of 4 cm, both in agreement with experimental measurements [BP-PED-2].

In the pedestal transport research area, 2D interpretive simulations using SOLPS showed marginal changes in the pedestal region of the effective electron heat and particle diffusivities during the ELM cycle. In addition, NSTX researchers have compared SOLPS and XGC0 ion heat diffusivity in the pedestal and found it to be neoclassical.

The microstability properties of the pedestal without and with lithium coated PFCs has been analyzed with the GS2 code. At the pedestal top, microtearing modes are dominant without lithium. With lithium, these are stabilized by the larger density gradient at this location. Within the pedestal, the experimental parameters are close to the ideal and kinetic ballooning boundaries, but are in the second-stable region with growth rates decreasing with increased pressure gradient [BP-PED-3].

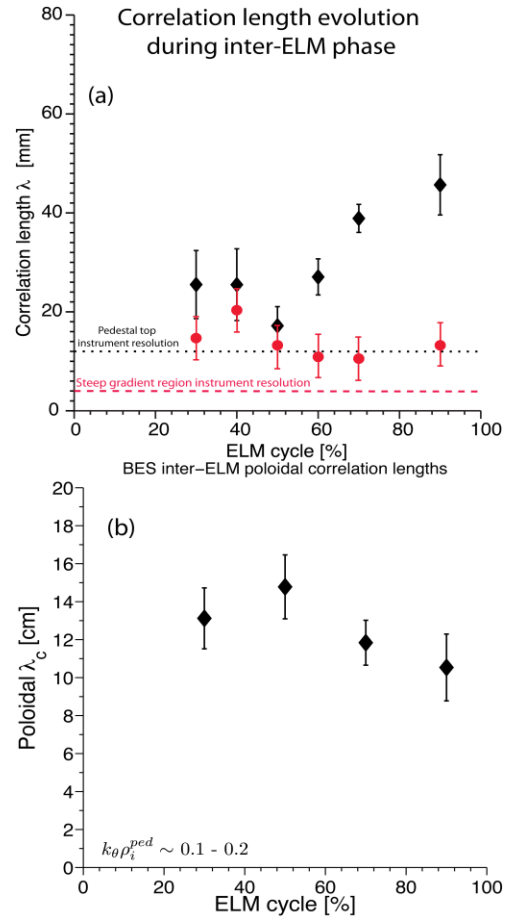


Figure BP-PED-1: Measured correlation lengths during ELM cycle. (a) Radial correlation lengths in both the steep gradient and at the pedestal top. These measurements are performed using the reflectometer. (b) BES measurements of the poloidal correlation lengths.

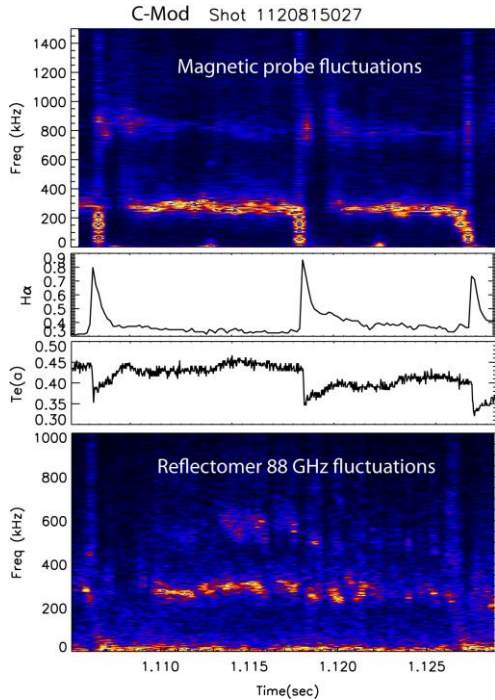


Figure BP-PED-2: From top to bottom: Magnetic probe spectrogram, D_{α} , edge temperature, and reflectometer at 88 GHz.

Collaboration with Alcator C-Mod

Later in FY12, to further our understanding of the fluctuations responsible for clamping the pedestal gradient early in the ELM cycle, NSTX researchers collaborated with the C-Mod group to document characteristics of pedestal fluctuations in both EDA and ELMy H-mode discharges on C-Mod. Figure BP-PED-2 displays the spectrograms of fluctuations between ELMs as observed using a magnetic probe dwelling near the limiter and density fluctuations measured using the reflectometer near the steep gradient. Preliminary results indicate clear correlation between density and magnetic fluctuations in the edge region. Furthermore, from this figure, it is clearly seen that the 300 kHz mode appears to track the edge temperature (see third panel) buildup. A proxy for the edge temperature is represented by the ECE outer channel as $T_e(a)$ where a is the separatrix.

References

- [BP-PED-1] A. Diallo et al. APS-DPP Invited 2011; *to be submitted to Phys. Plasma* (2012).
- [BP-PED-2] A. Diallo US-TTF, Annapolis, MD (2012).
- [BP-PED-3] J. Canik, 536/ EX – P7-16, to be presented at IAEA Conference (2012)

Edge 3D equilibrium, stability and transport

The physics behind the triggering of ELMs by 3D fields has been studied through the generation of 3D MHD equilibria using the VMEC code for discharges with 3D fields applied, combined with calculations of changes in stability and transport caused by these fields [BP-3D-1]. Results indicate that ballooning stability is degraded by 3D fields, but the effect is weak and unlikely to explain the robust ELM triggering observed. An assessment of the 3D neoclassical transport shows that, while small in the present experiments, this transport channel may be significant in the reduced collisionality plasmas enabled by the Upgrade. Finally, the new code SIESTA was used to calculate an equilibrium allowing for island formation. In contrast to simply applying the vacuum

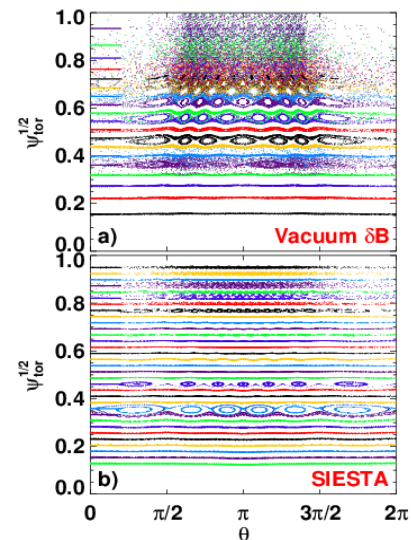


Figure BP-3D-1: Puncture plots with a) vacuum perturbation and b) plasma response calculated by SIESTA

with the plasma response

included, islands and stochastic regions are largely avoided at the plasma edge (Figure BP-3D-1), consistent with the lack of a reduction in T_e observed in experiment.

Determining the properties of open magnetic field lines in high-performance tokamaks is essential for advancing our physics understanding of the pedestal, SOL and divertor plasma. These open field lines result from bifurcations of the plasma edge that produce a complex web of intersecting homoclinic tangles [BP-3D-2] when 3D fields from non-axisymmetric perturbations such as: 1. field-errors, 2. magnetic materials, 3. correction coils, 4. control coils and 5. a variety of MHD plasma instabilities are present in any toroidal confinement system. In lower single null diverted tokamaks, the properties of these open field lines, such as the distribution of connection lengths from the outer to the inner target plates, penetration depths into the pedestal plasma and detailed distribution patterns on the divertor target plates, are calculated using a field line integration code that linearly superimposes the fields from engineering quality models of non-axisymmetric electromagnetic coils on an axisymmetric plasma equilibrium magnetic field. This is known as a vacuum field line solution. This code, referred to as the TRIP3D code, contains models of control and correction coils from a wide variety of tokamaks such as DIII-D, NSTX, MAST, ASDEX-Upgrade, KSTAR, JET and ITER as well as models of the DIII-D field-errors that are based on measurements made over several years. The TRIP3D code also has algorithms needed to quickly prototype coils designs for machines considering adding new coils or modifying existing coils. Additionally, in order to model the plasma response to 3D perturbation fields TRIP3D is coupled to a two-fluid MHD code referred to as M3D-C1. This provides a powerful research tool for quantifying changes between the open field line properties found in a vacuum solution and those found in the corresponding plasma solution.

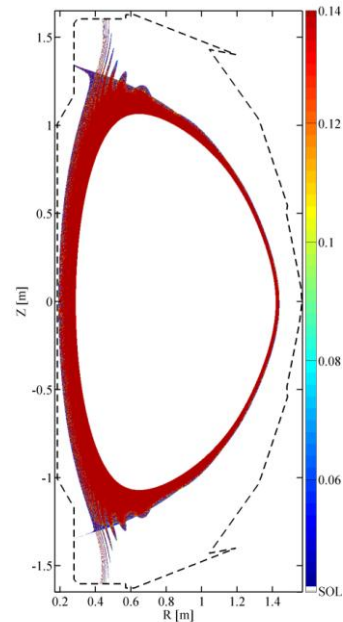


Figure BP-3D-2: NSTX poloidal cross-section showing $n=3$ lobes due to homoclinic tangles.

Recently, the TRIP3D code has been modified to run on a 960 core Tesla GPU computer and is being used to study the open field line properties in NSTX due to 3D fields from an external non-axisymmetric RWM field-error correction coils. Figure BP-3D-2 shows the connection length distribution of field lines passing inside the unperturbed separatrix, between the upper and lower divertor, in a double null NSTX plasma. Here, the lobes of the upper and lower hetroclinic tangle, as theoretically predicted [BP-3D-3] in double null plasmas, are seen intersecting the low-field side target plates over a relatively narrow region. The Tesla computer is essential for carrying out these studies since reasonably good quality simulations of divertor footprint distributions require calculations of at least 800,000 field lines which would take of order 3,000 cpu hours on a standard Linux workstation with the TRIP3D code but have been done in 56 gpu hours using the TRIP3DGPU code on 240 cores (i.e., a single GPU board) on the Tesla computer. As the development of the TRIP3DGPU code continues over the next few years simulations of the open

field line properties from a proposed internal non-axisymmetric perturbation coil on NSTX-U will be carried out and field-error models will be tested.

Lastly, the 3D edge transport code EMC3-EIRENE [BP-3D-4,5] was applied for the first time to NSTX [BP-3D-6]. Figure BP-3D-3a shows the electron temperature in the lower divertor region for shot 135183 at $t=433$, with 1kA of $n=3$ current in the RWM coils. Characteristic lobes formed by the separatrix manifolds are observed. These lobes are filled in by hot plasma from the pedestal region. The intersection of the lobes with the lower horizontal target plate creates spiraling ‘finger’ patterns in the heat and particle fluxes. At a given toroidal angle, a radial profile of the heat flux shows multiple peaks (see Fig. BP-3D-1b). Good qualitative is found in the modeled patterns and those measured by a 2D divertor IR camera.

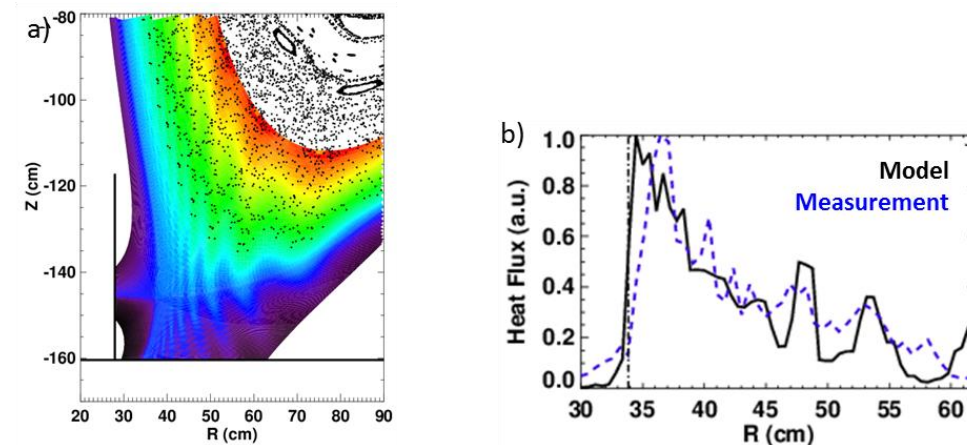


Figure BP-3D-1: a) Electron temperature at $\phi=0$ and b) modeled (black) and measured (dashed blue) normalized heat fluxes for a perturbed plasma.

References

- [BP-3D-1] J.M. Canik *et al.* Nucl. Fusion **52** (2012) 054004.
- [BP-3D-2] T.E. Evans, “Implications of topological complexity and Hamiltonian chaos in the edge magnetic field of toroidal fusion plasmas”, Chaos, Complexity and Transport: Theory and Applications, Ed. Cristel Chandre, Xavier Leoncini and George Zaslavsky, World Scientific Press, ISBN-13 978-981-281-897-9, May 2008, pp 147-176
- [BP-3D-3] Todd E. Evans, Andreas Wingen, Jon G. Watkins and Karl Heinz Spatschek, “A conceptual model for the nonlinear dynamics of edge-localized modes in tokamak plasmas”, Nonlinear Dynamics, Editor: T. E. Evans, Intech Publishing, Vukovar, Croatia, ISBN: 978-953-7619-61-9, January 2010, Chapter 3, pp 59-78.
- [BP-3D-4] Feng Y., *et al.*, J. Nucl. Mater. 241-243, 93 (1997).
- [BP-3D-5] Reiter D., *et al.*, Fusion Sci. Technol. 47, 172 (2005).
- [BP-3D-6] J.D. Lore, *et al.*, Nucl. Fusion 52, 054012 (2012).

L-H transition physics

It is routinely observed on NSTX that the heating power required for accessing H-mode decreases as the triangularity decreases (larger X-point radius) and as the amount of pre-shot lithium increases [BP-LH-1,2]. A dedicated experiment made a careful documentation of the L-H power threshold (P_{LH}) over a wide range of triangularity and levels of lithium deposition. The open divertor and ability to pump both strike points with lithium depositions independent of the strike point location on NSTX provided a unique opportunity to decouple the dependence of P_{LH} on changes in the X-point location and the divertor pumping. It was found that P_{LH} decreased 30% as the X-point radius was increased to a low-triangularity shape. A reduction in P_{LH} of about 20% (constant line-average density) to 100% (constant pedestal density) occurs when aggressively pumping with lithium [BP-LH-3]. The edge ion and electron temperatures were very similar at the time of the L-H transition, regardless of the core heating power, but did appear to scale with triangularity. Full-f kinetic neoclassical XGC0 simulations [BP-LH-4] indicate the P_{LH} vs R_X scaling can be attributed to changes in the $E \times B$ shear driven by an ion orbit loss hole [BP-LH-5], while the dependence of P_{LH} on divertor recycling is due to changes in the neutral penetration and fueling efficiency which impacts charge-exchange losses and ion particle transport.

References

- [BP-LH-1] R. Maingi et al., *Nucl. Fusion* **50** (2010) 064010
- [BP-LH-2] S.M. Kaye et al., *Nucl. Fusion* **51** (2011) 113019
- [BP-LH-3] D.J. Battaglia et al., *Nucl. Fusion*, to be submitted
- [BP-LH-4] S. Ku, et al., *Phys. Plasmas*, **11** (2004) 5626-33
- [BP-LH-5] C.S. Chang et al., *Phys. Plasmas*, **9** (2002) 3884-92

Scrape-off-layer (SOL) turbulence - modeling

In previous work [BP-SOL-1], Lodestar researchers successfully modeled qualitative features of the scaling of the heat-flux width for four discharges in NSTX. The experimentally observed strong inverse scaling with plasma current, I_p , and a much weaker scaling with exhaust power, P_{SOL} , were recovered numerically. These studies provided an experimentally validated base from which further numerical exploration of the SOL width scaling could be carried out using the SOLT (Scrape-Off Layer Turbulence) code. The new studies [BP-SOL-2] have revealed a transition from quasi-diffusive to convective transport in the SOL. Critical parameters for the transition were investigated, including the power flux into the SOL, the field line pitch, the connection length and the plasma collisionality.

In a separate study, the dynamics of blob-filaments in the edge and scrape-off-layer (SOL) region of a tokamak plasma was considered, with emphasis on sheared flow generation. Edge sheared flows are believed to be important for the L-H, and H-L transitions, and improved understanding of their role will be required for first-principles scalings of these transitions for ITER and future

devices. Both SOLT-code simulations and experimental data analysis were employed in our studies. A blob-tracking algorithm based on 2D time-resolved images from the gas puff imaging diagnostic was also developed [BP-SOL-3] and applied to NSTX, Alcator C-Mod and simulation data. The algorithm tracks the blob motion and changes in blob structure, such as elliptical deformations, that can be affected by sheared flows. Seeded blob simulations were shown to reproduce many qualitative and quantitative features of the data including size, scale-length and direction of perpendicular (approximately poloidal) flows, the inferred Reynolds forces, poloidal reversal of blob tracks, and blob trapping and/or ejection. Mechanisms related to blob motion, SOL currents and radial inhomogeneity were shown to be sufficient to explain the presence or absence of mean sheared flows in selected shots. This work will be reported in a poster at the upcoming 2012 IAEA meeting [BP-SOL-4], and in an invited talk at the 2012 DPP-APS meeting [BP-SOL-5].

Scrape-off-layer (SOL) turbulence – measurements and analysis

Data from the gas puff imaging (GPI) diagnostic on NSTX taken in 2010 was still being analyzed this past year, since the edge turbulence structure and motion which is seen in the GPI data is still far from understood.

A graduate student Bin Cao from IPP in China visited PPPL for one year to work on the analysis of the NSTX GPI data (ending March 2012). He evaluated the changes in edge turbulence which occurred during a scan with variable lithium wall coating, in order to help understand the reason for the confinement improvement with lithium. There was a small increase in the edge turbulence poloidal velocity and a decrease in the poloidal velocity fluctuation level with increased lithium. The possible effect of varying edge neutral density on turbulence damping was evaluated for these cases in NSTX, and a paper on this topic was submitted to PPCF [BP-SOL-6].

This set of GPI data also provided a nearly ideal basis for validation of the DEGAS 2 model for neutral transport in the edge plasma and for the transport of molecular deuterium in particular. The principal improvement over previous DEGAS 2 validation exercises was absolute calibration of the GPI diagnostic and the availability of data on the amount of gas puffed. Consequently, the total number of photons recorded by the camera per source atom could be determined. The corresponding quantity found in DEGAS 2 simulations of four discharges was very similar, with differences much less than a factor of two. The radial location and width of the simulated and observed light emission clouds in four shots agreed to within ~ 1 cm, comparable to the uncertainties. A paper on this topic is in preparation.

The GPI diagnostic on NSTX can also be used to measure the two-dimensional evolution of Edge Localized Mode (ELM) precursors. Precursor events were observed preceding ELMs and ELM-induced H-L back transitions in radio frequency (RF) heated H-mode plasmas, and the growth of the precursor mode through the ELM filamentation was imaged in the plane perpendicular to the local B-field. Strong edge intensity modulations appeared to propagate in the electron diamagnetic direction while steadily drifting radially outward. Intensity fluctuations were observed at frequencies around 20 kHz and wavenumbers of 0.05-0.2 cm^{-1} . Quantitatively similar precursors

have been observed in Ohmic H-mode plasmas as well, though significantly fewer events are seen in the Ohmic cases and none were observed in NBI heated H-modes. These results were recently submitted to PPCF [BP-SOL-7].

A dual GPI diagnostic was designed for the EAST tokamak with the help of advice from PPPL. First results were obtained during 2012 and a paper describing these results is being prepared for the Review of Scientific Instruments.

References

- [BP-SOL-1] J. R. Myra, D. A. Russell, D. A. D'Ippolito, J.-W. Ahn, R. Maingi, R. J. Maqueda, D. P. Lundberg, D. P. Stotler, S. J. Zweben, J. Boedo, M. Umansky, and NSTX Team, *Phys. Plasmas* **18**, 012305 (2011).
- [BP-SOL-2] J. R. Myra, D. A. Russell and D. A. D'Ippolito, *Plasma Phys. Control. Fusion* **54**, 055008 (2012).
- [BP-SOL-3] W.M. Davis, S.J. Zweben, J.R. Myra, D.A. D'Ippolito and M. Ko, *54th Annual Meeting of the APS/DPP*, October 29-November 2, 2012, Providence, RI.
- [BP-SOL-4] J. R. Myra, D. A. D'Ippolito, D. A. Russell, W.M. Davis, S. J. Zweben, J.L. Terry, and B. LaBombard, *24th IAEA Fusion Energy Conference*, San Diego CA, October 8 – 13, 2012, paper 251-TH/P4-23.
- [BP-SOL-5] J. R. Myra, D. A. D'Ippolito, D. A. Russell, W.M. Davis, S. J. Zweben, J.L. Terry, and B. LaBombard, *54th Annual Meeting of the APS/DPP*, October 29-November 2, 2012, Providence, RI.
- [BP-SOL-6] B. Cao, S.J. Zweben, D.P. Stotler, M. Bell, A.Diallo, S.M. Kaye, B. LeBlanc, "Edge Turbulence Velocity Changes with Lithium Coating on NSTX", submitted to *Plasma Physics and Controlled Fusion* (2012)
- [BP-SOL-7] Y. Sechrest, T. Munsat, D. Battaglia, and S. J. Zweben, "Two-dimensional characterizat on of ELM precursors in NSTX", submitted to *Plasma Physics and Controlled Fusion* (2012)

Divertor Physics

Snowflake divertor studies for NSTX-U

The snowflake (SF) divertor configuration is being developed as a leading divertor heat flux mitigation candidate for NSTX-Upgrade and next-step devices such as ST-FNSF. In NSTX-U, two up-down symmetric sets of four divertor coils will be used to test SF divertors for handling the projected steady-state peak divertor heat fluxes of 20-30 MW/m² in 2 MA discharges up to 5 s long with up to 10 MW NBI heating. Magnetic equilibria with SF configurations have been successfully modeled using the ISOLVER Grad-Shafranov equilibrium solver (Fig. BP-SFN-1) and showed that a robust snowflake control can be maintained even when time-dependent electromagnetic effects are included.

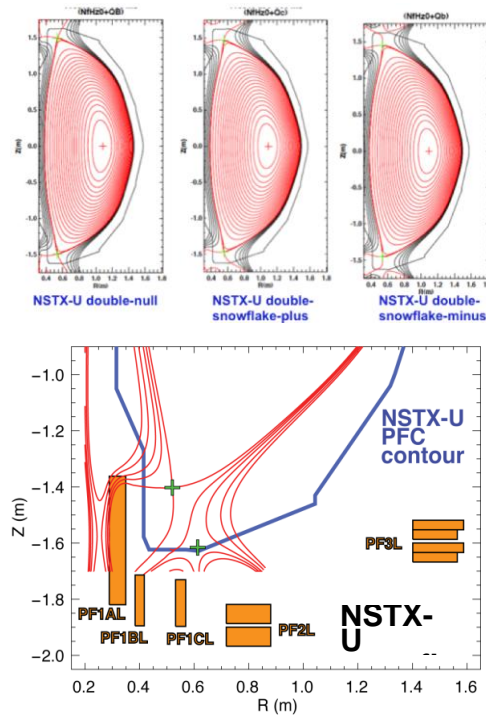


Figure BP-SFN-1: Examples of modeled plasma equilibria with snowflake divertor configurations for NSTX-U.

Analysis of NSTX snowflake divertor experiments continued in 2012 [BP-SFN-1,2,3]. In NSTX, three existing divertor coils with pre-programmed currents were used to obtain snowflake configurations lasting up to 0.6 s ($\leq 10 \tau_E$) in 1.0-1.2 s long 4 MW NBI-heated strongly-shaped H-mode discharges (Fig. BP-SFN-1). Analysis of the experimental equilibria, in combination with a recently developed one-parameter analytic description of the magnetic configurations provided guidelines for the design of a real-time feedback control algorithm, which is presently being implemented. The snowflake divertor had a profound effect on the H-mode discharge parameters. While core H-mode confinement with $\tau_E \sim 50$ -60 ms, $W_{plasma} = 200$ -250 kJ, and $H98(y,2) \sim 1$ (calculated using TRANSP) was maintained, core and edge carbon concentration was reduced by up to 50 %. As the snowflake configuration was formed, Type I ELMs that were otherwise stabilized by pedestal changes linked to the use of Li, re-appeared (Fig. BP-SFN-2).

Transient heat and particle fluxes from Type I ELMs remain an unresolved issue for future divertor designs. ELM elimination techniques are explored, as radiative buffering of ELMs has been found ineffective. In the NSTX snowflake divertor, heat fluxes from Type I ELMs ($\Delta W_{plasma}/W_{plasma} = 7$ -10 %) were significantly dissipated (Fig. BP-SFN-3). Peak target temperatures, measured by fast infrared thermography at peak ELM times, reached 1000-1200 °C in the standard divertor and only 300-500 °C in the snowflake phase. This was consistent with the lower surface temperature rise due to the longer convective heat deposition time because of the longer L_x in the snowflake divertor, and the convective heat redistribution mechanism in the null-point region proposed theoretically. The snowflake configuration was maintained during the ELMs.

As the snowflake divertor configuration was formed, the plasma-wetted area A_{wet} , the X-point connection length L_x , and the divertor volume V_{div} increased continuously by up to 50-75 % (cf. standard divertor). This led to a stable partial detachment of the outer strike point otherwise inaccessible in the standard divertor at $P_{SOL}=3$ MW in NSTX. Peak divertor heat flux was reduced from 3-7 MW/m² to 0.5-1 MW/m² between ELMs. The reduction factor quickly exceeded the geometric factor proportional to A_{wet} , as the estimated $q_{||}$ reduction from 80-100 MW/m² in the standard divertor to 10-30 MW/m² in the radiative snowflake phase was observed. The additional volumetric losses were corroborated by the divertor radiation and the recombination rates that also continuously increased, exceeding that of the standard divertor by up to 50 %. An additional CD₄ seeding increased divertor radiation further, thus demonstrating the potential to enhance non-coronal impurity radiation in the snowflake configuration due to its already reduced T_e regime. The snowflake divertor also showed better impurity gas screening characteristics, with edge and pedestal carbon densities being lower than in the seeded and unseeded standard divertor discharges.

To enable these projections of heat and particle fluxes in NSTX-U a two-dimensional multi-fluid edge transport model based on the UEDGE code is developed. The model development for NSTX-U started with an accurate two-dimensional numerical mesh that was based on the MHD equilibrium modeled with the ISOLVER code. The curvilinear meshes were generated for the standard divertor and for the snowflake-minus configurations, as shown in Fig. BP-SFN-4. The meshes spanned about 3 cm in the radial direction at the midplane (0.9-1.2 in normalized flux coordinates). Radial transport was described by constant electron and ion particle and heat transport coefficients $D_{perp} = 0.25$ m²/s, $\chi_{i,e} = 2$ m²/s in these initial simulations. A diffusive neutral model was used for deuterium neutral transport. Initial modeling showed large reductions in T_e , T_i , particle and heat fluxes due to the geometric and radiation effects. Radiative detachment of all snowflake cases with 3% carbon and up to $P_{SOL} \sim 11$ MW was obtained, with q_{peak} reduced from ~ 15 MW/m² (standard) to 0.5-3 MW/m² (snowflake) as shown in Fig. BP-SFN-4. Initial modeling also showed higher neutral pressure (density) in the lower flux expansion region of the snowflake-minus configuration at a radial location considered for a pump duct for a cryogenic panel. Future plans include coupling this model with DEGAS 2 Monte-Carlo neutral transport model for improved calculation of neutral transport for the cryo-pump design.

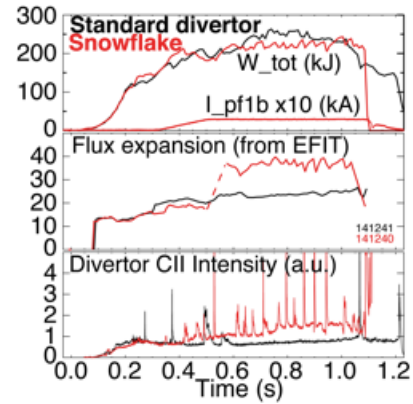


Figure BP-SFN-2: Time histories of plasma stored energy (a), snowflake divertor coil current (a), divertor outer strike point flux expansion (b), and divertor C II emission intensity (c) in the standard (black) and snowflake (red) divertor discharges discussed.

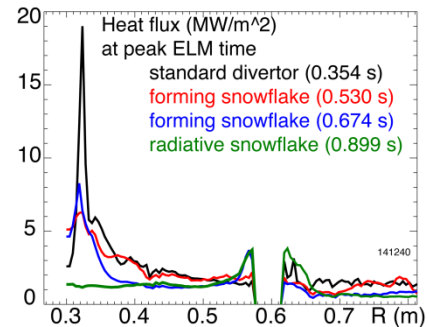


Figure BP-SFN-3: Divertor heat flux profiles measured in the standard and snowflake divertor configuration at peak Type I ELM times.

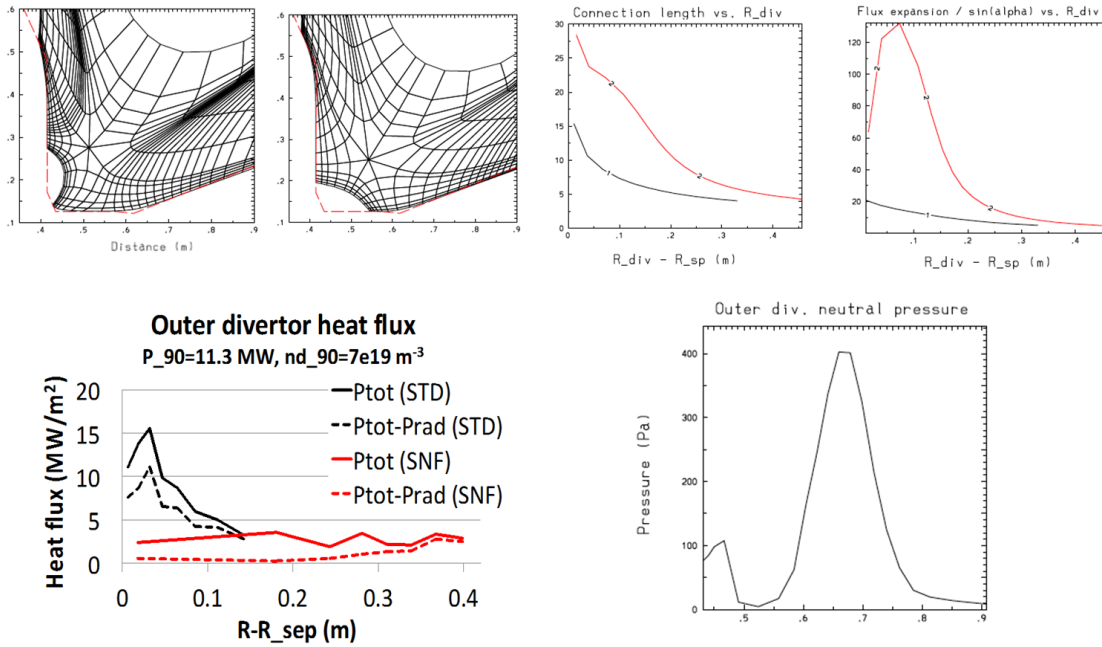


Figure BP-SFN-4: Projections of snowflake divertor parameters to NSTX-U from UEDGE model. Shown are high-resolution numerical meshes, divertor geometry parameters, heat fluxes and neutral pressure distributions for the standard and the snowflake divertors.

References

- [BP-SFN-1] V. A. Soukhanovskii, et al., *Divertor heat flux mitigation with impurity-seeded standard and snowflake divertors in NSTX*, Proceedings of the 39th EPS Conference on Plasma Physics, Stockholm, Sweden, 2012, Paper P5.049
- [BP-SFN-2] V. A. Soukhanovskii, et al., Phys. Plasmas **19**, 082504 (2012)
- [BP-SFN-3] V. A. Soukhanovskii, et al., Submitted to J. Nucl. Materials.

Snowflake divertor results from DIII-D

In 2012 NSTX-U staff proposed and executed an experiment to study the snowflake divertor configuration on DIII-D. Magnetic equilibrium reconstructions have confirmed that the benefits of the snowflake magnetic geometry were realized (w.r.t. the standard divertor): the outer strike point poloidal magnetic flux expansion (i.e. A_w) was increased by a factor of 2.5–3.0, with concomitant increases in connection length and divertor volume. Results show significantly reduced (a) inter-ELM peak

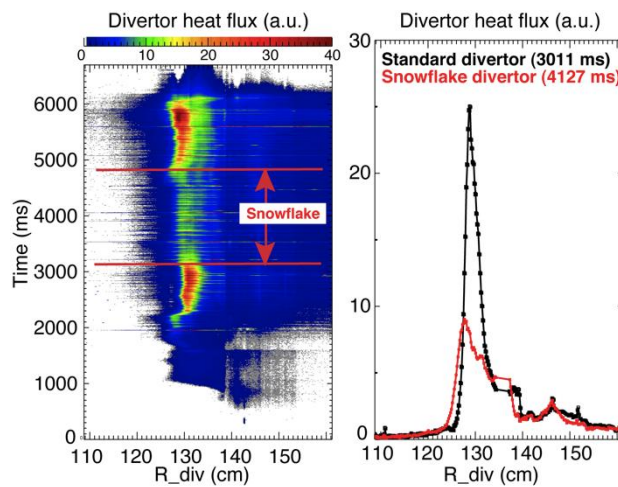


Figure BP-SFD-1: Divertor IR imaging shows reduction of heat flux during snowflake divertor configuration. The main (outer) peak of the heat flux is shown.

heat flux (Fig. BP-SFD-1) and (b) energy loss per ELM without pedestal pressure reduction (Fig. BP-SFD-2). In the DIII-D tokamak, steady-state snowflake divertor configurations were maintained for up to 3 s using *existing* divertor coils operated in their normal operational range. Variations from the fully x-point overlapped “ideal” snowflake configurations were also studied as shown in Fig. BP-SFD-3: snowflake-plus, where the secondary x-point lies in the private flux region, and snowflake-minus, where it lies in the boundary of the core plasma.

As shown in Fig. BP-SFD-2b, core confinement in 1.2 MA 3–5 MW NBI-heated H-mode discharges was unaffected by the snowflake configuration as evidenced by $HL89\sim 2.1$, $H98(y,2)\sim 1.2\text{--}1.3$ in the standard divertor phases and the snowflake phases. Most discharges had a steady $n/m=3/2$ MHD mode during most of the high performance phase. In these initial studies, the core density at which the divertor detaches (measured by CIII 2-D profiles in the lower divertor) was similar to the standard divertor.

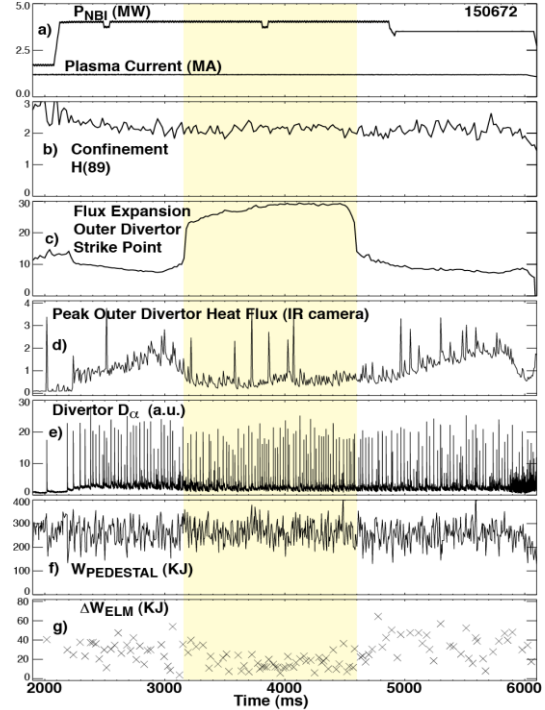


Figure BP-SFD-2: During the SF configuration (highlighted), the c) EFIT flux expansion increases $\sim 3x$, and the d) average between-ELM peak divertor heat flux (IRTV) decreases. Detailed ELM analysis shows that the e) pedestal energy is constant, while the f) change in energy per ELM decreases.

The snowflake divertor magnetic geometry had a marked effect on the ELMs and divertor transport. Detailed analysis of the pedestal parameters shows that the energy loss per ELM was reduced by roughly a factor of 2 from $\Delta W_{ELM}/W_{PED}\sim 12\%$ to $\sim 6\%$. For the discharges analyzed, most of the ELM energy loss appears in the conductive channel, as the change in pedestal density per ELM $\Delta n_{ePED} / n_{ePED}=27\%$ before the Snowflake and $\sim 24\%$ during the Snowflake, while the change in pedestal temperature per ELM is $\Delta T_{ePED} / T_{ePED}=18\%$ before the Snowflake and is reduced to $\sim 9\%$ during the snowflake. This reduction in ELM conductive loss channel is similar to that observed with gas puffing. However, in contrast to the gas puffing case, there is no reduction in the pedestal pressure during the Snowflake divertor operation (Fig. BP-SFD-2f).

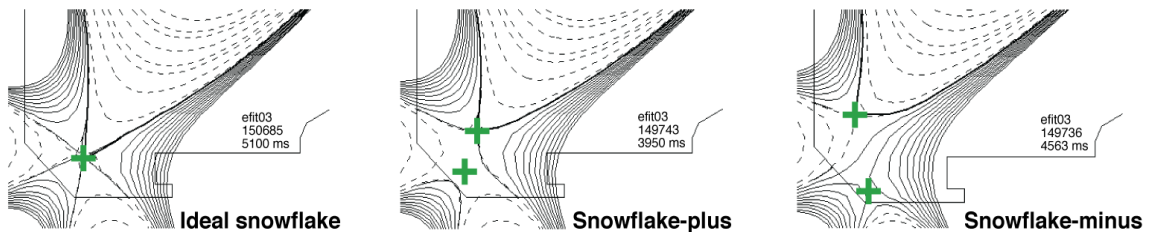


Figure BP-SFD-3: The EFIT reconstructions of the (left) ideal snowflake, the snowflake-plus, and the snowflake-minus configurations in DIII-D. The green plus-signs indicate the x-points. These configurations were made both in different discharges, and in separate phases of the same discharge.

The DIII-D results further support the SF divertor configuration as a promising plasma-material interface for the advanced tokamak (AT)-based fusion nuclear science facility and for the DEMO, where the standard axisymmetric magnetic X-point divertor may be inadequate for keeping divertor heat load and divertor plate erosion within the operating margins of plasma-facing components. Future experiments in DIII-D will seek to produce the SF configuration in ITER-shaped plasmas, and to explore the operational regime.

References

- [BP-SFD-1] Ryutov, D., Phys. Plasmas **14** (2007) 064502
[BP-SFD-2] Piras, F. et al., Plasma Phys. Controlled Fusion **51** (2009) 055009; Plasma Phys. Controlled Fusion **52** (2010) 124010; Phys. Rev. Lett. **105** (2010) 155003
[BP-SFD-3] Soukhanovskii, V. et al., Nucl. Fusion **51** (2011) 012001; Phys. Plasmas **19** (2012) 082504

Development of radiative divertor control for NSTX-U

In the NSTX-U device, discharges with $I_p \leq 2$ MA, $P_{\text{NBI}} \leq 10$ MW and up to 5 s duration are projected to produce steady-state peak divertor heat fluxes in the range 20–30 MW/m², thereby challenging thermal limits of divertor plasma-facing components (PFCs). A radiative (partially detached) divertor technique is used in tokamak experiments and planned for ITER to mitigate high divertor heat loads and material erosion of divertor plasma-facing components (PFCs) to prevent their thermal and structural damage. The radiative divertor uses induced divertor volumetric power and momentum losses to reduce heat and particle fluxes on divertor target plates. Deuterium and/or impurity gas seeding has been employed to control the radiative divertor plasma parameters in several tokamak experiments via a real-time feedback control of the gas injection rate. In the National Spherical Torus Experiment (NSTX), a large spherical tokamak with lithium-coated graphite PFCs and high divertor heat flux ($q_{\text{peak}} \leq 15$ MW/m²), radiative divertor experiments employed D₂, CD₄, or Ne gas injections that were controlled by pre-programmed waveforms. Experimental and modeling efforts are underway to design and implement real-time feedback control of divertor conditions in the NSTX Upgrade facility [BP-RDIV-1].

In previous NSTX experiments, a single-channel divertor gas injector was used. For NSTX-U, an upgrade to the system is proposed. The upgraded system would include four outlets placed axi symmetrically in the lower and upper divertor regions in the physical gaps between divertor plates. To control the gas inventory, existing turbo-molecular pumps and a divertor cryogenic panel (presently under consideration) would be used. The seeding impurity gas is selected based on operational and atomic physics (radiated power at low Te) considerations. In the initial period of NSTX-U operations, all graphite PFCs conditioned via lithium and boron coatings are planned, and the seeding gas options are D₂, CD₄, and Ar. Nitrogen is excluded at this stage due to its chemical reactivity with lithium coatings and its absorptivity into graphite. If NSTX-U is upgraded with molybdenum and/or tungsten PFCs, then D₂, N₂, and Ar would be used.

It is expected that the same divertor diagnostics used in NSTX would be available for NSTX-U divertor characterization in the initial operations period. In NSTX radiative divertor experiments, a significant reduction of divertor heat flux from peak values of 4–10 MW/m² to 0.5–2 MW/m², simultaneously with good core H-mode confinement characterized by H98(y,2) up to 1, has been demonstrated in 1.0–1.3 s discharges. A partial divertor strike point detachment was characterized in NSTX using a number of divertor plasma measurements: divertor plate PFC temperature (heat flux), radiated power using bolometry and impurity emission spectroscopy, neutral gas pressure measurements, ion flux using Langmuir probes, and divertor recombination using UV or NIR spectroscopy. Shown in Fig. BP-RDIV-1 are divertor time traces in two 0.8 MA 4 MW NBI-heated H-mode discharges, a reference discharge, and a radiative divertor discharge with CD₄ seeding. In the radiative divertor discharge, peak divertor heat flux was reduced from 4–5 to 1–2 MW/m² in the detachment phase that started at about 0.7s. These time traces will be used to illustrate the control signal options for NSTX-U. On the basis of these experiments, two categories of diagnostics have been identified: (1) divertor plasma and PFC diagnostics and (2)

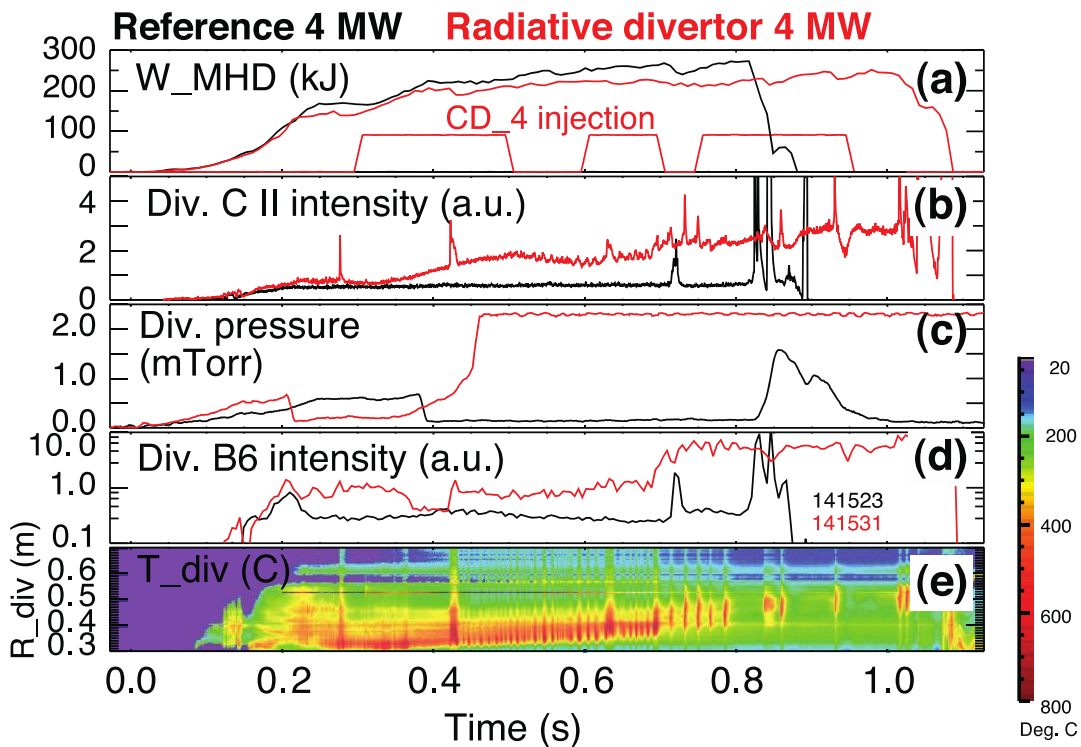


Figure BP-RDIV-1: Time traces of a reference (black) and a radiative divertor (red) H-mode discharges: (a) Plasma stored energy WMHD and CD₄ injection waveforms, (b) divertor C II ($\lambda=658.5$ nm) intensity, (c) divertor neutral pressure, (d) divertor Balmer $n = 2-6$ line intensity in the strike point region, and (e) divertor PFC temperature from IR thermography.

the diagnostics characterizing the pedestal or core plasma that can be used as “security” measures to insure the radiative divertor compatibility with H-mode confinement. The control diagnostic signals recommended for NSTX-U include divertor radiated power, neutral pressure, spectroscopic deuterium recombination signatures, infrared thermography of PFC surfaces, and thermoelectric scrape-off layer current, as well as spectroscopic “security” monitoring of possible confinement or pedestal degradation.

Initial considerations for spatial and temporal requirements to the control signal are as follows. The characteristic detachment onset time in NSTX was 5–20 ms, and it is expected to be similar in NSTX-U. The control signal spatial resolution should be better than 1 cm, and the ability to distinguish between inner and outer divertor leg parameters is important. One concern with spatially (both poloidally and toroidally) localized divertor signals is that they can be affected by changes in plasma shaping, strike-point locations, and toroidal asymmetries in heat and particle fluxes during the application of 3D fields. This could limit the operating space of the control system if it is based on a single spatially localized diagnostic.

References

[BP-RDIV-1] V. A. Soukhanovskii, et al., Rev. Sci. Instrum. **83**, 10D716 (2012)

Characterization of lower divertor carbon and lithium sputtering and sources

In order to obtain a better understanding of the behavior of lithium conditioned plasma facing components (PFCs), lithium and carbon sputtering characteristics were studied by means of a high resolution divertor spectrometer and photometrically calibrated fast visible cameras equipped with narrow bandpass filters using incoming ion fluxes measured by Langmuir probes and atomic coefficients based on the S/XB method.

The application of lithium coatings on graphite plasma facing components resulted in only a moderate reduction of carbon sputtering yield as it is evident from carbon sputtering measurement in the divertor near-SOL. In Figure BP-CLI-1, the relative carbon sputtering yields are plotted versus time and normalized psi for three discharges: with boronized PFCs (black), with 2.2 grams of lithium but no fresh lithium (blue) and a discharge with 190 mg of fresh pre-applied lithium (red). This is consistent with measurements carried out during the 2010 run campaign which indicate carbon sputtering yield consistently of the order of 1%, indicating a few times reduction from the generally expected carbon sputtering from graphite at oblique incidence. A clearer picture of how lithium coatings affect divertor carbon influxes is emerging. In particular, the reduction in carbon sputtering expected from the coverage of graphite tiles with lithium can

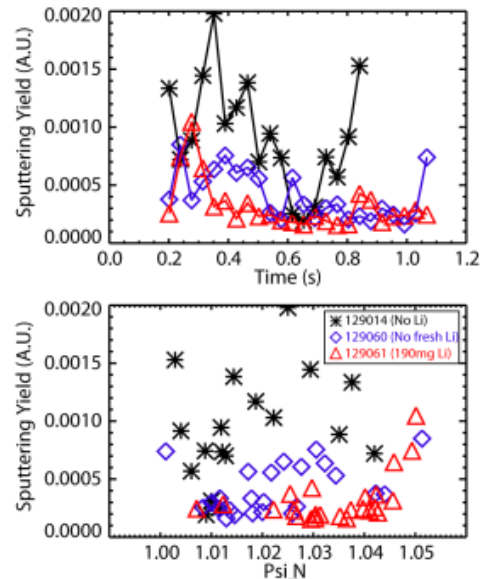


Figure BP-CLI-1: Divertor relative sputtering yield for boronized and lithium-coated carbon tiles.

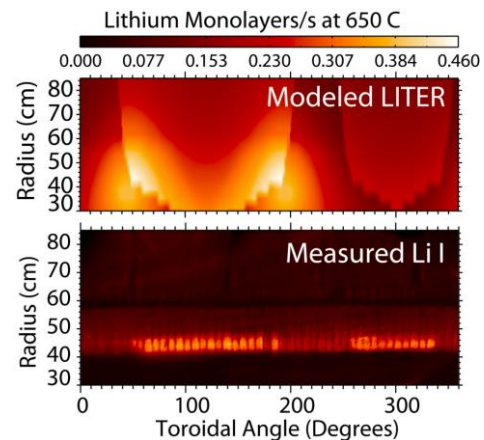


Figure BP-CLI-2: Toroidally asymmetric deposition of lithium (modeled, top panel) resulting in asymmetric plasma-surface interaction and lithium erosion.

be counteracted by both the limited lifetime of the coating (degrading under the divertor particle and heat fluxes) and the change in divertor plasma parameters (due to the transition of the SOL to a sheath-limited regime).

For what concerns Li sputtering and influxes, the analysis of neutral Li sputtering showed neutral lithium sputtering yields less than 10% from solid lithium coatings, consistent with measurements on other tokamaks and test stands. However uncertainties still remain on the actual surface composition and the role of self-sputtering or impurity-induced sputtering. The expected temperature enhancement of lithium sputtering was clearly observed both as a result of surface heating due to plasma heat flux at the strike point region as well as a result of external heating of PFCs. Toroidal asymmetries in lithium influxes were routinely observed as a result of the toroidally asymmetric lithium deposition pattern of the lithium evaporators as shown in Figure BP-CLI-2. Toroidal asymmetries were enhanced during transient heat loads and in the proximity of the strike point.

Characterization of carbon and lithium particle transport in the plasma core

In NSTX lithium conditioned ELM-free discharges, a low concentration ($\sim 1\%$) and peaked carbon density (n_C) profile in L-mode typically evolves into a strongly hollow n_C profile at the H-mode transition with a steady slower accumulation into the core and concentrations up to 10%. Lithium ions show a similar profile evolution but with the extremely low core n_{Li} of $\sim 1\%$ of core n_C . In a typical ELM-free H-mode NSTX discharge, deuterium ions are well inside the banana-plateau regime while both carbon and lithium ions are in plateau regime in the core and in Pfirsch-Schlüter regime in the edge region. Carbon is a strong impurity and is mostly collisional on deuterium ions while lithium is a trace impurity mostly collisional on background carbon ions, thus the importance of including multi-ion effects for lithium transport. The neoclassical transport codes NCLASS and NEO were used to derive neoclassical fluxes and transport coefficients in mixed regimes, multi impurity NSTX plasmas (two impurity species were included C^{6+} and Li^{3+}) [BP-CLI-1]. The very low lithium concentrations allowed a sensitivity study on n_{Li} with minor perturbation to the overall n_e profiles using NCLASS. This indicated a negligible effect on carbon transport due to the presence of lithium ions as was also suggested from collisionality estimates. Lithium transport, on the other hand, is mostly driven by collisions on carbon ions. The high background carbon density leads to an increase in lithium particle diffusivities. In Figure BP-CLI-3, the diffusion coefficients and convective velocities are plotted for the two different impurities as computed using NCLASS and NEO. Lithium ions have a 10x higher edge diffusivity

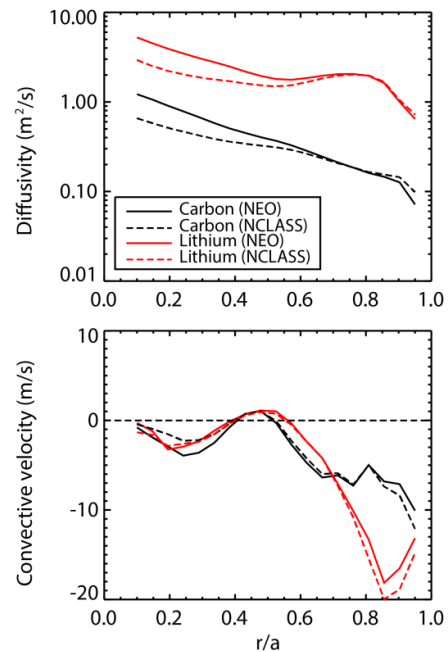


Figure BP-CLI-3: Carbon and lithium transport coefficients inferred from NEO and NCLASS modeling.

with comparable or higher inward edge convective velocities. The difference in the two impurities transport characteristics was modeled using the MIST code in a predictive mode using the neoclassical transport coefficients for carbon and lithium calculated by NCLASS to predict the time evolution of the charge state distribution of the two impurities given the same edge impurity source. Modeling with the MIST code shows how the high edge diffusivities results in core n_{Li} that varies from $\sim 30\%$ to a few % of n_C , decreasing with the increase in n_C over time. This is qualitatively consistent with the low n_{Li} observed in the NSTX core as well as with the decrease of the lithium-to-carbon inventory as the discharge progresses. However, experimentally measured n_{Li} are usually 1% of n_C or less since the early phase of the discharge indicating the possible importance of other divertor/SOL processes in reducing the edge lithium sources.

References

[BP-CLI-1] F. Scotti, et al., *Study of Neoclassical Core Transport of Intrinsic Impurities in the National Spherical Torus Experiment*, Proceedings of the 39th EPS Conference on Plasma Physics, Stockholm, Sweden, 2012, Paper P4.031.

Simulations of radiating properties of divertor lithium

While the presence of a lithium coating in NSTX has an important effect on the surface recycling properties, less is known of its impact on the divertor plasma. Owing to lithium being a low-Z material, it is generally believed to not radiate a substantial amount of power from the core. However, in the divertor with a low electron temperature ($T_e \sim 1$ eV) and corresponding high electron density, lithium has the potential to radiate a significant amount of power as can be

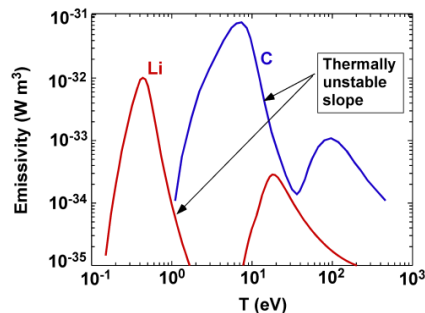


Figure BP-LIRAD-1: Coronal emissivity comparing lithium and carbon vs T_e .

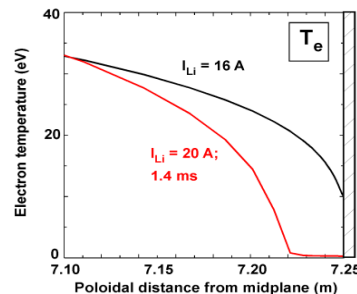


Figure BP-LIRAD-2: Predicted divertor T_e profile for two lithium fluxes emitted from divertor at right.

estimated from the emissivities as shown in Fig. BP-LIRAD-1. The radiated power is the product of the emissivity, the lithium density, and the electron density, and curves for both lithium

and carbon are shown.

In a more detailed study of lithium in the

divertor region for a simplified geometry with UEDGE, we have found that a sufficient amount of lithium sputtered or evaporated from a divertor plate can induce plasma detachment. This model uses a full multi-charge-state lithium model with multi-step ionization processes included, thus going beyond the coronal model used for the emissivity figure here. It is found that a small increase in the divertor-plate emission of lithium, from 16 Amps to 20 Amps, has a dramatic effect on the divertor T_e as shown in Fig. BP-LIRAD-2. The region with $T_e \approx 1$ eV shown in the red curve is a signature of divertor plasma detachment, and the suddenness of the detachment onset is thought to be associated with the thermally unstable portion of the emissivity curve in Fig. BP-LIRAD-1. Work is continuing to model NSTX in more detail and to make direct comparisons with data to determine the role of this mechanism on divertor detachment.

Characterization of non-axisymmetric divertor plasma surface interactions

A pair of two-dimensional fast cameras with a wide angle view (allowing a full radial and toroidal coverage of the lower divertor) was used in NSTX in order to monitor non axisymmetric effects [BP-DCAM-1]. A custom polar remapping procedure and an absolute photometric calibration enabled easier visualization and quantitative analysis of non-axisymmetric plasma material interaction. In particular, this new capability was applied for the analysis of asymmetry in impurity influxes as a result of the toroidal asymmetry of evaporated lithium coatings. Furthermore, this technique was applied for the study of non axisymmetric plasma material interaction (e.g. strike point splitting due to application of 3D fields). In Figure BP-DCAM-1, three different cases (all imaged with a Li I filter) compared to an axisymmetric unperturbed outer strike point (Figure BP-DCAM-1a). Non axisymmetric particle and heat deposition was observed as a result of: application of 3D fields which results in outer strike point splitting (Figure BP-DCAM-1b), edge localized modes (Figure BP-DCAM-1c) and HHFW heating of the edge plasma which results in non-axisymmetric divertor helical structures (Figure BP-DCAM-1d).

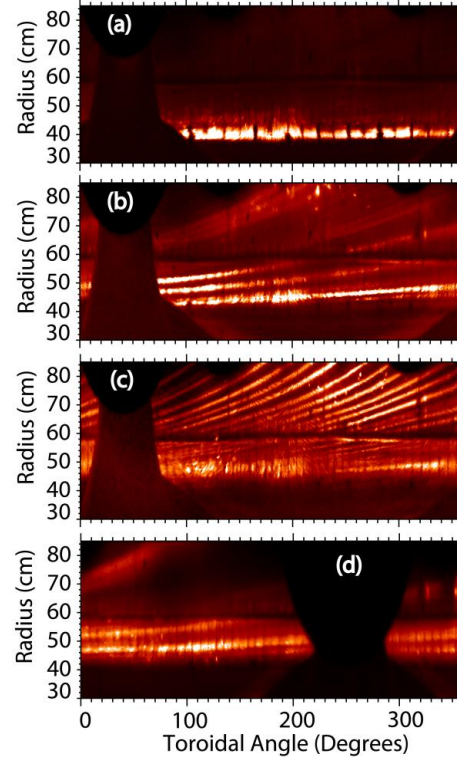


Figure BP-DCAM-1: Divertor camera imaging of plasma-lithium interactions due to magnetic perturbations, ELMs and HHFW heating, as explained in text.

References

[BP-DCAM-1] F. Scotti, et al., Rev. Sci. Instrum. 83, 10E532, 2012.

Impact of 3D magnetic field ELM control on radiative divertors

The compact size of the ST geometry naturally leads the divertor heat flux problem more challenging for a given heating power and plasma current. This is true for both the steady state and the transient ELM heat deposition. Therefore, the ELM control using the 3D fields and the peak heat flux reduction technique with the divertor detachment must be compatible with each other. Results for the effect of applied 3D fields on the divertor plasma in NSTX can be found in [BP-3DD-1,2]. Partial divertor detachment both on the inboard and outboard sides has been demonstrated in the high performance H-mode plasmas in NSTX [BP-3DD-3].

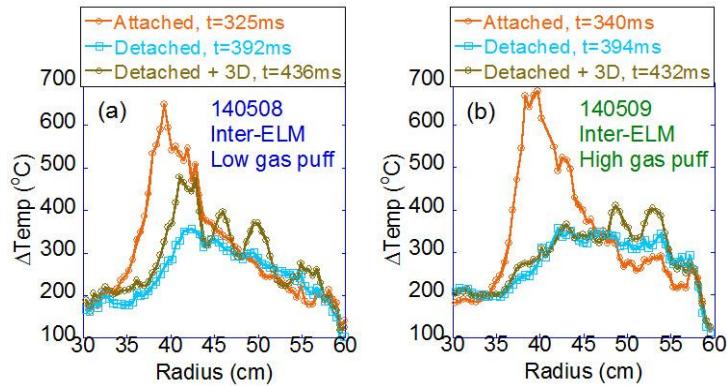


Figure BP-3DD-1: Measured surface temperature profiles for discharges with divertor detachment by (a) low and (b) high divertor gas puff (D_2). Each profile is color coded; orange is before gas puff, blue is after gas puff, gold is after gas puff plus 3D field application.

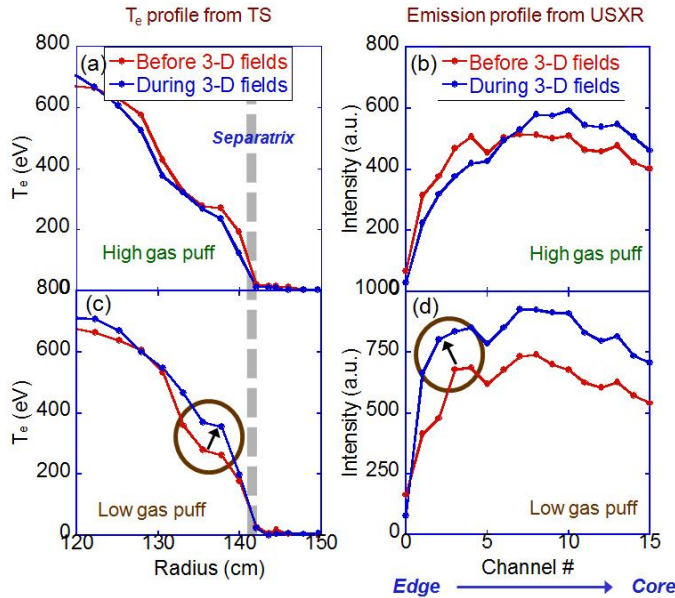


Figure BP-3DD-2: Pedestal T_e profile (left column) and poloidal USXR channel signals (right column). The upper row (figures (a) and (b)) is for high gas puff and the lower row (figures (c) and (d)) is for the low gas puff, with 3-D fields applied later during the detached phase in both cases.

by $\sim 50\%$ compared to those in the attached regime before the gas puff. It is also seen that the surface temperature profile is slightly more peaked for the low gas puff case. This is interpreted as a “weaker” detachment compared to the high gas puff case. The gold profiles are after the 3D field was applied to the detachment. It is clearly seen that the temperature profile becomes peaked again in the low gas puff case, i.e. the divertor plasma re-attaches. However, it stays flat in the high gas puff case, which indicates that the plasma remains detached. Therefore, the 3D fields can re-attach weakly detached plasmas but this can be avoided by enhancing detachment with higher gas puffing.

A large amount of deuterium (D_2) gas is puffed into the divertor area for the naturally ELMy H-mode plasma to produce partially detached divertor condition, *i.e.* detachment only occurs near the strike point. Then $n=3$ perturbation field is superimposed for the 2nd half of the gas puff period with the amplitude of 3D coil current ($I_{3D} = -0.5$ kA) below the ELM triggering threshold [BP-3DD-2]. Plots in figure BP-3DD-1 are the divertor surface temperature profile during the inter-ELM period, measured by the high speed dual band IR camera. Two levels of gas amount for the divertor puff were tested. Figure BP-3DD-1(a) is for the low gas puff and BP-3DD-1(b) is for the high gas puff case. Temperature profiles in orange are before the gas puff and are peaked near the strike point at $r \sim 40$ cm in both cases, which indicates that the divertor plasma is attached. The blue profiles are obtained after the detachment onset (by gas puff) but before the 3D field application. The peak surface temperature is reduced

As the detachment of divertor plasma is established, the pedestal T_e progressively drops with increasing gas puff, while the pedestal n_e changes only little [BP-3DD-4]. The T_i and V_i profiles also decrease modestly in the overall pedestal region with the onset of detachment. Therefore, the pedestal T_e drop is most prominently observed in NSTX when the divertor plasma detaches. Figure BP-3DD-2 illustrates the effect of 3D fields on the pedestal plasma with detachment. Panels (a) and (c) are the mid-plane T_e profiles and (b) and (d) are the emission profiles from a

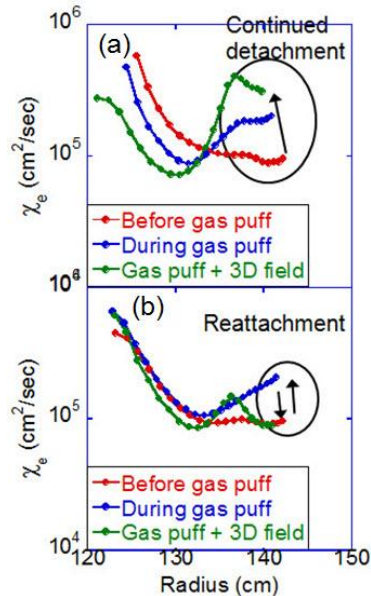


Figure BP-3DD-3: Evolution of pedestal χ_e profile from TRANSP modelling for (a) high and (b) low divertor gas puff with 3D fields applied later during the detached phase.

poloidal array of ultra soft X-ray (USXR). The upper row, panels (a) and (b), is for the high gas puff and the lower row, (c) and (d), is for the low gas case. In the continued detachment case with high gas puff, the pedestal T_e profile remains decreased before and after turning on the 3D field, so the applied 3D field has no effect on the T_e profile, figure BP-3DD-2(a). It is also seen in figure BP-3DD-2(b) that the USXR data for the edge channels continuously decrease. On the other hand, in the case of re-attachment, the pedestal T_e rises back up after the application of 3D fields (see figure BP-3DD-2(c)). The increase is usually by ~ 100 eV and the edge soft X-ray data also shows an increase - see Figure BP-3DD-2(d). As the pedestal n_e does not change significantly as explained above, this increase of edge USXR is attributed to the increase of pedestal T_e .

TRANSP modeling was carried out for these discharges [BP-3DD-4] and figure BP-3DD-3 shows the pedestal electron heat diffusivity (χ_e) profiles. For the continued detachment case, the pedestal χ_e continuously increases during the whole detachment and the later 3D field application phases. It shows

the same trend during the detachment phase, *i.e.* χ_e rises, in the low gas puff case, but comes back down when the 3D fields are applied and the divertor re-attachment occurs. This result is consistent with the T_e profile data shown in figure BP-3DD-2. It is not yet understood why, under this condition, the 3D fields lead to reduced χ_e and higher T_e in the edge region.

References

- [BP-3DD-1] J-W. Ahn et al, Nucl. Fusion 50, 045010 (2010)
- [BP-3DD-2] J-W. Ahn et al, Phys. Plasmas 11, 056108 (2011)
- [BP-3DD-3] V.A. Soukhanovskii et al, Nucl. Fusion 49, 095025 (2009)
- [BP-3DD-4] J-W. Ahn et al, Plasma Phys. Control. Fusion, submitted (2012)

Divertor VUV spectrometer development for NSTX-U

Understanding divertor power balance and accurate power accounting is needed for divertor experiments aimed at divertor heat flux mitigation. Divertor radiated power is due to low-Z impurities that strongly radiate $T_e \leq 10$ eV. At these temperatures, about 80-90 % of power is radiated through line emission in the 20 – 160 nm range. To understand the impurity radiated power, the LLNL group is preparing to operate a vacuum ultraviolet (VUV) spectrometer SPRED on NSTX-U. The spectrometer will be mounted on a horizontal divertor port with a view of the lower divertor region. The measurements would support NSTX-U plasma-facing component and divertor programs, by providing routine steady-state and transient divertor impurity measurements (e.g., Mo III-XIV, Li II, C II, C III, C IV line emissions). With supporting analysis, it may be possible to derive divertor carbon ionization balance (steady-state and during ELMs), divertor T_e estimates from C II, C III, C IV line ratio measurements, deviation from Maxwellian electron energy distribution function, and improved divertor P_{rad} estimates from radiative divertor impurity radiation (CD₄, N₂, Ne, Ar).

The SPRED spectrometer has been brought from LLNL (Livermore, CA) to PPPL and its performance was evaluated at the Low Temperature Plasma Laboratory at PPPL (Y. Raitse). The spectrometer was mounted on a DC-RF Penning discharge operated with argon and xenon, as shown in Figure BP-VUV-1. A range of magnetic fields and RF power levels provided a number of confinement modes and temperatures of the Penning discharge. The tests in LTP laboratory at PPPL confirmed excellent VUV sensitivity and resolution properties of two gratings and MCP image intensifier. The spectrometer has been moved to TFTR basement for storage at PPPL. For NSTX-U applications, absolute calibration at NIST SURF III synchrotron source is being considered.

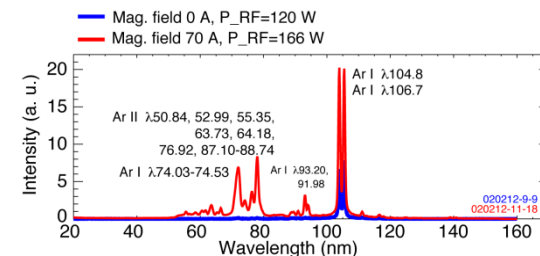
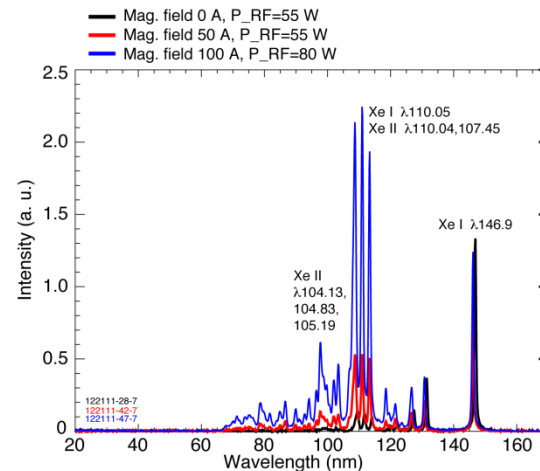
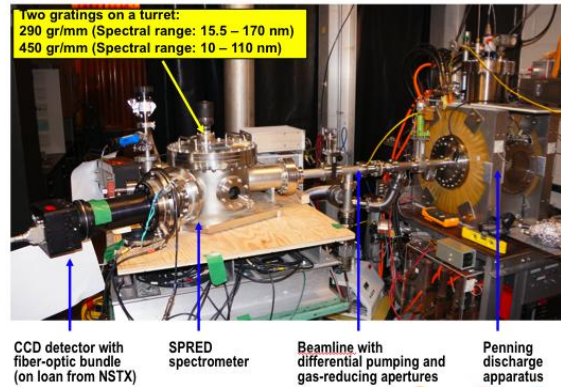


Figure BP-VUV-1: The LLNL SPRED VUV spectrometer mounted on the Penning low temperature plasma source at PPPL (top) and examples of Xenon and Argon spectra obtained at different plasma temperatures.

Materials and PFC Research for NSTX-U

Magnum-PSI Collaboration Experiments and Liquid Metal PFC Development

Experiments on lithiated plasma facing component materials have been conducted on the Magnum-PSI linear plasma device located at the Dutch Institute for Fundamental Energy Research (DIFFER). Magnum-PSI is a magnetized, linear plasma device designed for simulating the divertor conditions expected in ITER-class devices (10^{21} m^{-3} , $T_e \sim 1\text{-}5\text{eV}$) [MP-1]. The device currently operates with copper magnetic fields coils with discharge lengths from 5-50s (field dependent) and will soon be upgraded to provide steady-state discharges with a superconducting magnet. The plasma conditions present at the Magnum-PSI target provide similar density and temperatures as those found in NSTX, for example, during the recent liquid lithium divertor campaign [MP-2]. In these discharges densities of $1\text{-}5 \times 10^{20} \text{ m}^{-3}$ and temperatures of $T_e \sim 3\text{-}5\text{eV}$ were found in the vicinity of the strike-point creating a good match between the NSTX divertor and Magnum-PSI capabilities.

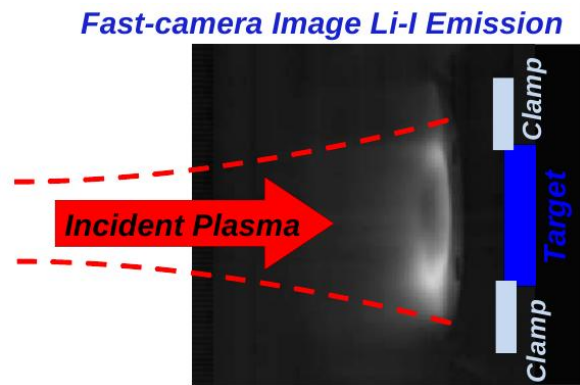


Figure MP-1: Fast-camera image of sample exposed in Magnum-PSI linear plasma device. Image shows Li-I (671nm) emission.

The Magnum-PSI device is well diagnosed and well suited to PMI studies. Plasma density and temperature are measured via Thomson scattering on a single chord parallel to the target surface

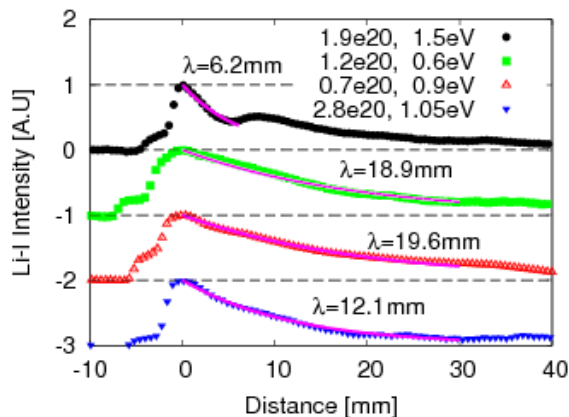


Figure MP-2: Normalized Li-I (671nm) emission intensity as a function of distance from the sample surface in the plane of the camera view. Exponential decay fits are shown for the regions indicated in each of the discharges shown.

at an adjustable distance of 1-3cm (typical range). Numerous broad-band spectrometers are available for monitoring specific line emission from the plasma; for these experiments the spectroscopic views observed the same volume of space as measured by Thomson. Infrared thermography is utilized for measuring surface temperature of the sample, in addition to calorimetry of the cooling water. Visible wavelength fast-cameras are available for recording plasma dynamics and observing spatial emission structure directly in front of the target. Figure MP-1 shows one

such image of Li-I (671nm) emission during plasma bombardment.

For these experiments, a lithium evaporator was commissioned and operated on Magnum-PSI. The evaporator consists of a commercial source with custom mounting for use in the Magnum-PSI Target Exchange and Characterization (TEAC) chamber. Evaporation was monitored with a quartz-crystal microbalance and calibrated to give approximately 100nm thick lithium depositions on the target. Samples were prepared at PPPL

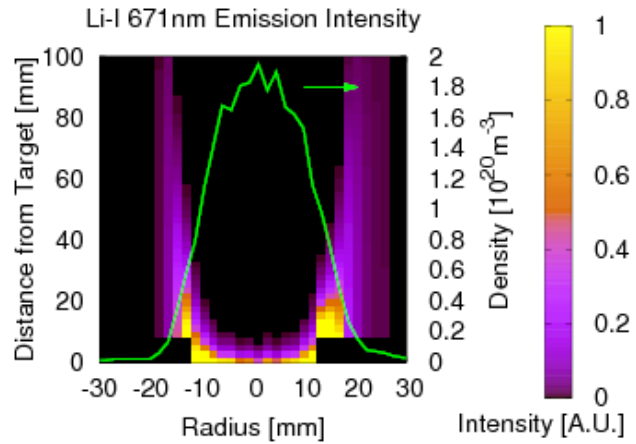


Figure MP-3: Li-I (671nm) emission simulated using experimental density and temperature profiles measured with Thomson scattering.

composed of ATJ graphite, molybdenum alloy TZM, and pure tungsten. Exposures were taken with and without deposited lithium over a range of densities and temperatures in the machine.

A set of experiments were carried out on Magnum to develop a database of observations of the lithium migration in the local plasma as prelude to material migration modeling in NSTX-U. The spatial distribution of lithium emission measured by the filtered fast-camera provides information on the transport of this material near the target surface. Figure MP-2 shows a representative set of data obtained by processing the emission intensity over a band through the center of the target.

Ionization, excitation and recombination rate coefficients are available from the ADAS database [MP-3] and show strong dependencies on temperature and density. Qualitatively, the visible emission data are consistent with expectations based on temperature and density scaling.

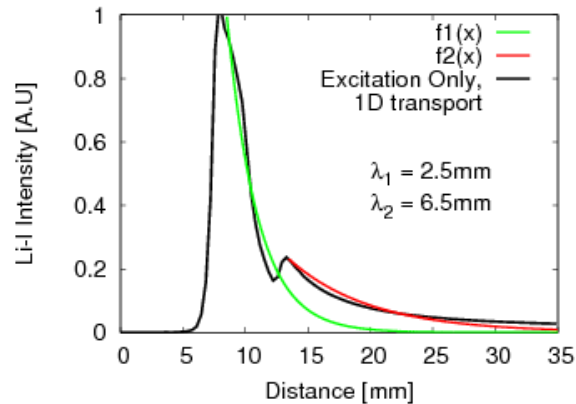


Figure MP-4: Simulated Li-I (671nm) emission profile through center of plasma volume at relevant camera angle ($\sim 11^\circ$ from parallel to surface).

A quantitative evaluation of lithium transport into the plasma requires inclusion of 2D-spatial information and viewing geometry information (i.e. synthetic diagnostic). An initial model was developed using the fluid continuity equation to model neutral lithium transport with an “Onion-skin method” approach. Background density and temperatures were obtained from Thomson scattering and assumed uniform in the z-direction. A constant lithium sputter-yield corresponding to SRIM calculations [MP-4] at the applied bias energy (40eV) was utilized alongside a calculated particle flux (also from Thomson) to provide a lithium source term. Only excitation and ionization is included in the present model. Figure MP-3 shows a model result corresponding to the plasma conditions in the top-most set of data of figure MP-2. Figure MP-4 shows the simulated diagnostic profile.

The modeling reproduces the double-peaked structure observed in the data and produces decay constants about a factor of 2 off from those in the experiment. However, relative strength of each peak are not well matched. Examination of the ADAS database indicates that recombination and charge-exchange are significant in the density and temperature range of these experiments and are not yet included in the model. In summary, the initial results are encouraging, but still require additional work to reproduce the observed profiles. Once the basic elements of the model are validated, then modeling of additional impurity species, such as oxygen and carbon, can be validated with further experiments.

Liquid Metal Plasma-Facing Component Research and Development

In addition to the study of plasma-material interactions on lithiated substrates, development of flowing liquid lithium PFCs and related technologies is underway at PPPL in the form of engineering analysis and design work in addition to some modest experimental research and development in on-site laboratory spaces. The present efforts focus on an actively cooled, capillary-restrained system that incorporates gaseous cooling. The conceptual diagram of the design is shown in figure MP-5.

The PFC includes a porous or textured front face, similar to that used on the Liquid Lithium Divertor [MP-5] for which stability analysis indicates that for porous materials with pore sizes of order 0.01mm, very large current densities are required to destabilize and eject droplets [MP-6]. This method for reducing droplet ejection via reduced pore size was experimentally observed on T11-M with the Red-Star CPS system [MP-7]. In order avoid a long wicking path-length between a lithium source or reservoir and the PFC front-face, lithium flow channels are located parallel to the cooling channels with discrete ports to allow the liquid metal to wick to the front-face. The thin liquid layer results in large viscous forces in addition to MHD damping and the resulting flow velocities are expected to be

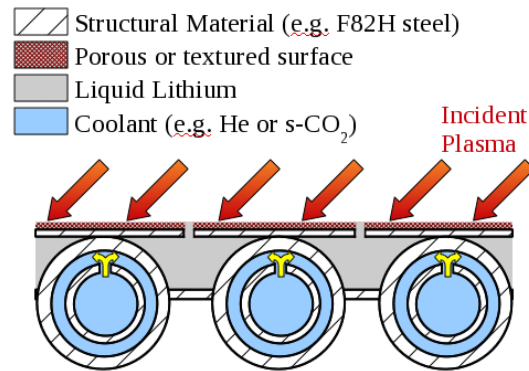


Figure MP-5: Conceptual diagram of the actively cooled, capillary-restrained liquid-metal PFC concept.

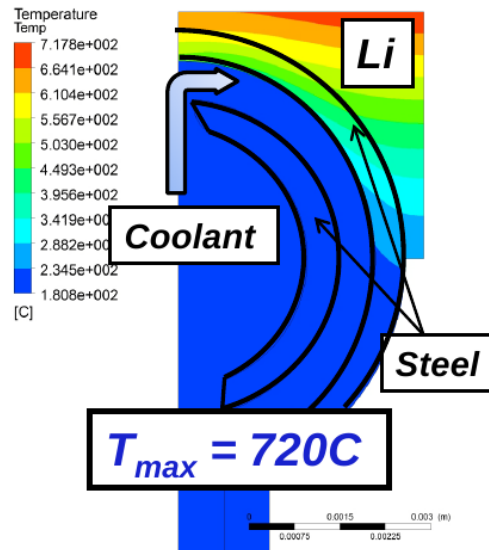


Figure MP-6: Thermal-hydraulic simulation of the liquid metal PFC concept utilizing a T-tube cooling configuration. Supercritical-CO₂ is utilized in this simulation. Active cooling is sufficient to maintain the steel (F82H) at about 610C - in the range where ODS steels can operate. 10MW/m² incident heat flux is simulated.

small which enables the temperature transport to be described by thermal conduction [MP-8].

This reliance on thermal conduction allows the significant work on gaseous cooling to be used in the liquid metal context and scaling studies with the US-based T-tube concept [MP-9] have been carried out as shown in Figure MP-6. In addition to size scaling, an examination of the basic cooling fluid is also being carried out. Supercritical carbon dioxide (s-CO₂) has been identified by many in the fission power industry as having favorable properties in a power cycle over helium [MP-10]. These include more efficient power-cycles overall for similar turbine inlet temperatures, more compact turbo-machinery leading to lower capital costs, lower leak rates overall and improved heat transfer efficacy at power-cycle-relevant pressures and temperatures. Calculations performed with ANSYS/CFX analysis code of the T-tube configuration with identical volumetric flow-rates of He and s-CO₂ indicate that s-CO₂ can reduce the peak surface temperature by over 250C of a solid-W target. While tungsten PFCs are the leading solid-PFC choice, lithium-coated PFCs are expected to operate at temperatures below the tungsten ductile-to-brittle transition temperature of 800C [MP-11]. At lower temperatures, however, steel materials are potential substrates for use with liquid lithium where the lithium provides a low-Z protective layer over the high-Z steel. This material choice eliminates the need to transition from structural steels to tungsten where the operating temperature windows do not always overlap [MP-11]. It is likely, however, that the oxide-dispersion strengthened (ODS) types of steels will be necessary for the elevated temperatures and coolant pressures in a divertor PFC.

Despite even more efficacious cooling with s-CO₂ in the T-tube configuration, surface temperatures still range about 700C in the vicinity of the strike-point in the present set of design studies. This temperature would result in significant evaporation and sputtering from the surface of the PFC. Not only must the technology supply adequate replacement metal, but collection schemes must be developed to re-condense the material and close the liquid-metal loop. This result highlights the importance of plasma simulation with Magnum-PSI as such strong surface evaporation has never before been studied in the divertor configuration. Strong ingress of lithium into the local plasma also raises the possibility of developing *continually vapor-shielded PFCs*. Robust liquid lithium PFCs would therefore enable the study of this potentially attractive operating state in a high-power device such as NSTX-U.

Experimental demonstration of liquid metal PFC concepts is currently underway to complement the design studies described above. These begin with the development of a liquid lithium loop which will provide active pumping into and out of vacuum chambers. The facility will be utilized for testing of candidate PFC designs to show such things as (1) stable operation and flow in a tokamak-relevant vacuum environment (1e-7 to 1e-6 Torr pressures), (2) restart capability after periodic shut-down and gettering of residual gases, (3) maintainability and reliability in addition to safe operation. Future plans include active purification of lithium inventory and upgrades to include integrated tests with s-CO₂ or other gas-based cooling systems.

Compositional changes of lithium (Li) coatings on TZM during plasma bombardment

The Titanium-Zirconium-Molybdenum alloy TZM has previously been used as a metallic plasma-facing component (PFC) in Alcator C-Mod and is being considered for use in NSTX-Upgrade. While *ex-situ* tests have been performed to demonstrate the capability of Li-coated molybdenum to withstand the high heat loads present in the NSTX divertor region [MP-12], Li-coated TZM has not yet been studied in an NSTX-U relevant environment. The time evolution of Li coatings on TZM under high heat fluxes were studied for the first time in 2012 on Magnum-PSI, a linear plasma device located capable of ion fluxes up to $10^{25} \text{ m}^{-2}\text{s}^{-1}$ at electron temperatures $< 5 \text{ eV}$. These parameters are similar to those extrapolated for NSTX-U [MP-13].

A bare TZM sample was exposed to a series of 5-second D_2 plasma discharges with plasma parameters $0.6 \text{ eV} < T_e < 1.7 \text{ eV}$ and $10^{20} \text{ m}^{-3} < n_e < 4.0 \times 10^{20} \text{ m}^{-3}$. The sample was evaporatively coated with a $\sim 100 \text{ nm}$ thick Li layer and the series of discharges was repeated. Electron density and temperature were measured via Thomson Scattering on a single chord located $\sim 2.0 \text{ cm}$ away from the TZM target. The time evolution of the Li-I (671 nm) and O-I (777 nm) line emission intensity (in the same location as the Thomson measurements) were also measured using a broad-band visible spectrometer, typically operated with a time resolution of $5\text{-}10 \text{ s}^{-1}$.

Significantly different trends were observed for the evolution of the O and Li signal intensities during plasma exposure to Li-coated TZM. As shown in Figure MP-7, the Li-I signal continuously increased throughout each discharge, while the O-I signal peaked at $\sim 0.5 \text{ s}$ and subsequently decayed exponentially. The peak O-I intensity also decreased significantly in the second discharge, despite similar electron densities and temperatures. In contrast, the peak Li-I intensity actually increases slightly in the second plasma shot.

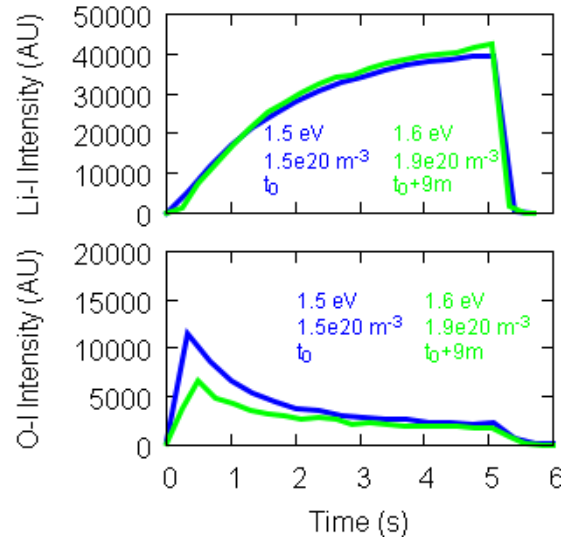


Figure MP-7: Time evolution of the Li-I and O-I signal intensities for two consecutive plasma discharges. Li-I intensity continually increases throughout each discharge while O-I intensity exponentially decays. The electron density and temperature as well as the relative discharge times are given.

The physical interpretation of these results is that a layer composed of lithium hydroxide (LiOH) and lithium oxide (Li_2O) formed on the first several monolayers of the Li surface. This impurity layer then partially eroded during each plasma discharge, as evidenced by the Li and O radiation. The relative changes in impurity emission in the plasma suggest an evolving surface composition. The evolution indicates a decreasing amount of oxygen in the surface that could be caused by a difference between the local *re-deposition* of Li and O on the substrate. Previous experiments on pure lithium in the PISCES-B plasma device also demonstrated cleaning of the Li surface under

plasma bombardment, but at much lower density and higher impact energy using helium bombardment [MP-14]. Whereas the discharge cleaning in PISCES-B required several hundred seconds of plasma exposure and elevated temperatures [MP-15], reduction of the oxygen emission was obtained in Magnum-PSI within the first second of plasma bombardment and reached saturation by 3-4s into the discharge.

Further analysis is ongoing to determine if the contamination and discharge cleaning can be modeled and extrapolated to NSTX-U operating conditions. Surface science experiments at PPPL have been examining the former process through controlled impurity gas puffs [MP-6, 7]. Shot-by-shot comparison in the Magnum-PSI divertor plasma simulator to obtain absolute quantities of each impurity species is possible with the existing diagnostic set and will be conducted to determine if a net cleaning of a lithiated PFC can be achieved for typical inter-shot periods in NSTX-U (10-20 min).

The Li-I and O-I emission from a PFC surface in the divertor is expected to be highly localized near this surface. The present experiments indicate that such a local measurement of impurity influx provides information on the composition of the PFC itself. The present results indicate that increased attention to the intensities of these two lines, at least, would prove a useful addition to the NSTX-U diagnostic set for understanding and characterizing the response of lithiated PFCs in the NSTX-U device.

NSTX-U-relevant Plasma-Material Interaction results from Alcator C-Mod collaboration

The NSTX-U Program is considering an option of molybdenum plasma-facing components (PFCs) in the divertor. To improve molybdenum PFC erosion diagnostics and understand plasma-surface interactions with boron-coated molybdenum, the LLNL/NSTX-U group started a new collaboration with PSFC MIT on the Alcator C-Mod tokamak.

An intensified charge injection device (CID) camera with a narrow bandpass interference filter was installed on Alcator C-mod to image the 550.6 nm Mo I emission associated with PFC erosion. Initial observations, including molybdenum erosion proportional to ICRH power and suppression after boronization, were found similar to those previously made with a visible range spectrometer at C-Mod. Subtraction of continuum sources (i. e. Planck emission, visible bremsstrahlung, D₂ molecular emission) and measurement of the SOL plasma temperature and density are necessary to interpret observed emission as erosion. Modifications of the diagnostic are in progress for simultaneous imaging of the line emission (including continuum) and spectrally adjacent continuum emission to facilitate this subtraction. For the first time, the camera spatially resolved hot spots on the primary (GH) limiter during operation of lower hybrid current drive (LHCD), shown in Figure MP-8. These hot spots were identified via their Planck continuum observed in coincident spectrometer views. Field line mapping links these locations to the LHCD antenna horns on the opposite side of the torus. Seeding of impurities during ICRH operation has been shown to suppress accumulation of eroded molybdenum in the plasma core. The mechanism, believed to be a combination of changes in transport and erosion, is still under investigation. The overall decrease of emission associated with Mo I as injected Neon increases suggests an overall reduction of gross erosion.

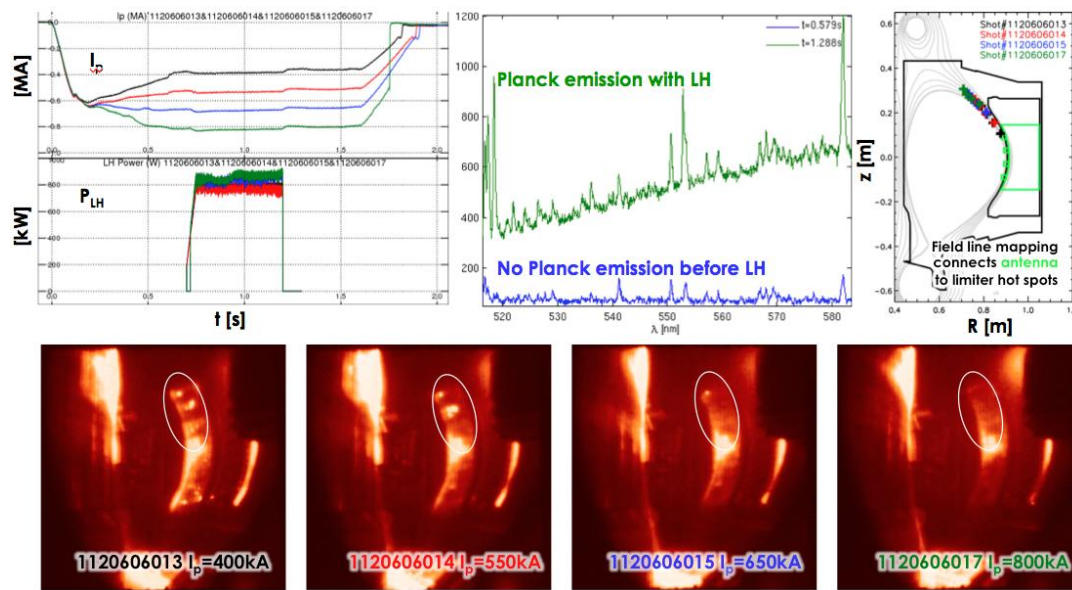


Figure MP-8: CID camera images filtered for 550.6nm Mo I emission showing hot spots during LHCD operation at surfaces with field line mapping to the antennas for a scan of magnetic pitch.

Accounting for edge cooling due to injected Neon, and modest increase of local Mo I emission on some portions of the GH limiter, the gross erosion source is observed to decrease even at regions of strongest erosion. Emissive probe measurements of the SOL potential along field lines mapping to the antenna face indicate an increase during ICRH from $\sim 10V$ to $>400V$ in some cases, and the effect of Neon injection on these potentials will be studied shortly. Operating the plasma in the I-mode results in a gradual purge of molybdenum impurities, as opposed to the accumulation observed in H-mode.

References

- [MP-1] G. De Temmerman, et al., J. Vac. Sci. Technol. A **30** (2012) 041306.
- [MP-2] M.A. Jaworski, et al., Fusion Eng. Des. (2012) *in press*.
- [MP-3] Summers, H. P. (2004) The ADAS User Manual, version 2.6 <http://www.adas.ac.uk>
- [MP-4] J. Zeigler, et al., Nucl. Instrum. Methods B **268** (2010) 1818-1823.
- [MP-5] H.W. Kugel, et al., Fusion Eng. Des. (2011) *in press*.
- [MP-6] M.A. Jaworski, et al., J. Nucl. Mater. **415** (2011) S985-S988.
- [MP-7] V.A. Evtikhin, et al., J. Nucl. Mater. **307-311** (2002) 1664-1669.
- [MP-8] M.A. Jaworski, N.B. Morley and D.N. Ruzic, J. Nucl. Mater. **390-391** (2009) 1055-1058.
- [MP-9] S.I. Abdel-Khalik, et al., Fusion. Sci. Technol. **54** (2008) 864-877.
- [MP-10] V. Dostal, M.J. Driscoll and P. Hejzlar, "A Supercritical Carbon Dioxide Cycle for Next Generation Nuclear Reactors", Technical Report MIT-ANP-TR-100, The MIT Center for Advanced Nuclear Energy Systems, March, 2004.
- [MP-11] S.J. Zinkle and N.M. Ghoniem, Fusion Eng. Des. **51-52** (2000) 55-71.
- [MP-12] T. Abrams et al., J. Nucl. Mater. – submitted 2012
- [MP-13] T.K. Gray et al., J. Nucl. Mater. **415** (2011) S360-S364.
- [MP-14] R. Doerner et al., J. Nucl. Mater. **290-293** (2001) 166-172.
- [MP-15] M. Baldwin et al., Nucl. Fusion **42** (2002) 1318-1323.
- [MP-16] R. Sullenberger, M.S. Thesis, Princeton University (2012)
- [MP-17] C.H. Skinner et al, J. Nucl. Mat – submitted 2012

Macroscopic Stability Research

NSTX-U RWM Active Control

While NSTX-U is a modification of NSTX, changes to the device conducting structure (e.g. new 2nd NBI port structure), midplane RWM control coils, and equilibria requires recomputation of $n = 1$ active RWM control performance using proportional gain, and RWM state space control. The upgrade also adds new capability, such as independent control of the 6 RWM coils. This new capability, combined with the upgrade of the RWM state space controller will also allow

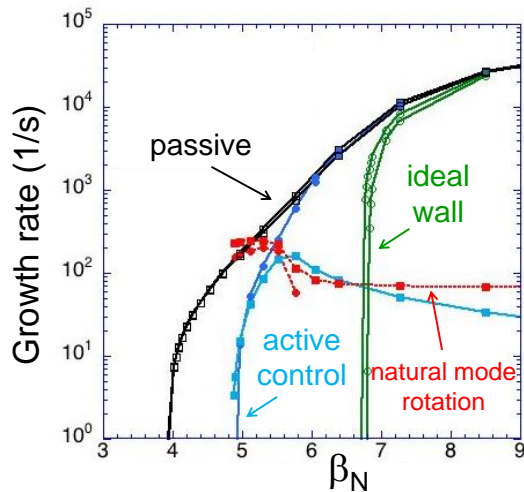


Figure MS-CU-1: $n = 1$ active RWM control performance for NSTX-U equilibria, 3D device conducting structure, and 6 midplane RWM control coils.

simultaneous $n = 1$ and $n = 2$ active control, along with $n = 3$ dynamic error field correction. Finally, the active control performance of the proposed off-midplane non-axisymmetric control coils (NCC) also needs to be evaluated. The first of these three tasks has been completed, with the results shown in Figure MS-CU-1 assuming no kinetic RWM stabilization by plasma rotation. The results are elucidating when compared to equivalent calculations made from past NSTX equilibria and conducting structure (see Fig. 8. in Ref. MS-CU-1). Active control performance in terms of β_N as measured as a percentage between

$n = 1$ no-wall and with-wall limits (i.e. C_β) is similar to past calculations for NSTX results, as expected. The major difference in the controllable β_N level at zero plasma rotation is due to the reduced $n = 1$ no-wall limit for the NSTX-U equilibria, which have higher aspect ratio than NSTX due to the larger center stack. A significant increase in controllable β_N is expected with the RWM state space control in NSTX-U, as was found for NSTX.

Active MHD Spectroscopy Analysis and RWM Stability vs. Plasma Parameters

Active MHD spectroscopy is an experimental diagnostic technique that is used as a proxy for kink-ballooning/RWM mode stability when modes are stable [MS-CU-2]. The “low-frequency” version of this technique typically measures the amplification and phase shift of a traveling $n = 1$ applied tracer field. Experimental evidence to date has shown large amplitude and phase shifts to indicate reduced mode stability. Dedicated experiments were performed in NSTX to determine the stability of long pulse, high β_N plasmas as a function of basic plasma parameters, and for comparison to kinetic RWM stabilization physics established and quantitatively compared to NSTX RWM marginal stability experiments [MS-CU-3]. Here, a 40Hz co-NBI rotating AC field was applied with the NSTX RWM coils, and the resonant field amplification (RFA) of that applied field was measured using magnetic sensors. MHD spectroscopy analysis software was upgraded to match the analysis in Ref. MS-CU-2 for direct comparison to results in the literature. Similar analysis was performed in a joint experiment conducted on DIII-D to compare results with NSTX.

Figure MS-CU-2 shows $n = 1$ RFA amplitude vs. β_N / l_i evaluated for many plasmas over the majority of the discharge pulse length. The increase in RFA amplitude as β_N / l_i is increased toward ~ 10 implies a decrease in stability. There is a large variation in RFA amplitude at a given β_N / l_i because other parameters, chiefly plasma rotation, are not constant. A particularly interesting trend is the *increased* stability of plasmas with high $\beta_N / l_i > 10$, which may be due to those plasmas having favorable rotation profiles. Figure MS-CU-3 shows that some plasmas become unstable at the intermediate rotation level of ~ 12 KHz while others survive and return to lower, more stable, RFA levels at low rotation. Again, there is a large variation of RFA amplitude at a given rotation level. This is partly because here we are plotting vs. only a single point in the rotation profile, while RWM stability depends more generally on profile effects.

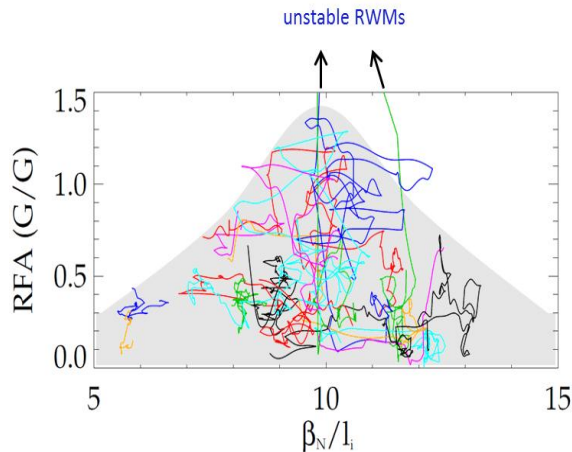


Figure MS-CU-2: RFA amplitude vs. β_N / l_i , showing generally decreasing stability as β_N / l_i is increased toward ~ 10 , and increasing stability at higher values.

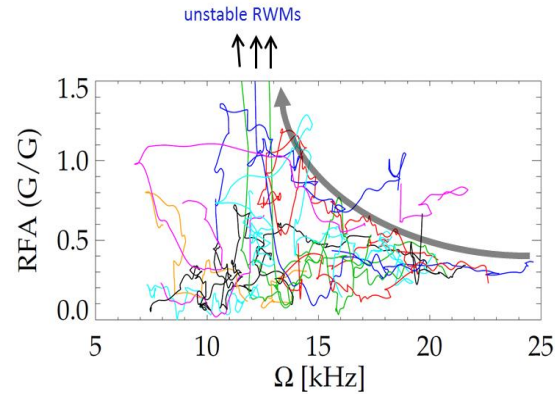


Figure MS-CU-3: RFA amplitude vs. carbon toroidal rotation at CHERS channel 6 (near the core), showing generally decreasing stability as rotation is reduced toward ~ 12 KHz.

Figure MS-CU-4 shows a comparison of three NSTX discharges showing the $n = 1$ signal on the upper poloidal magnetic field sensors, β_N , carbon toroidal rotation at CHERS channel 6 (near the core), and RFA amplitude, vs. time. Each discharge was subject to varying $n = 3$ non-resonant magnetic braking, which accounts for the steadily decreasing rotation. The discharge shown in blue became unstable at 0.9s when the rotation reached ~ 12 kHz. The discharge shown in red has the same β_N , but higher rotation and maintains stability, as would be expected (although the RFA rises to a high level when the rotation approaches ~ 13 -14 KHz, near the rotation level that drives the discharge shown in blue unstable). This discharge approaches marginal stability twice, but does not become unstable (see (a) and (d)). The discharge shown in black has *higher* β_N and *lower* rotation, but also maintains stability, which is counter-intuitive based on early RWM stability theory. Invoking resonant kinetic stabilization at low rotation provides an understanding for this observation [MS-CU-3]. Note that the RFA level for this discharge also peaks near the same rotation level that drives the discharge shown in blue unstable.

Development of NSTX kinetic RWM stabilization physics model and application to ITER

Theoretical development of the kinetic RWM stability model has continued, in collaboration with Riccardo Betti from the University of Rochester. It was demonstrated, and presented at the 2012 Sherwood Fusion Theory Conference in Atlanta, GA, that pressure anisotropy, as may occur for energetic particles injected with neutral beams, leads to a modification of the energy principle. A

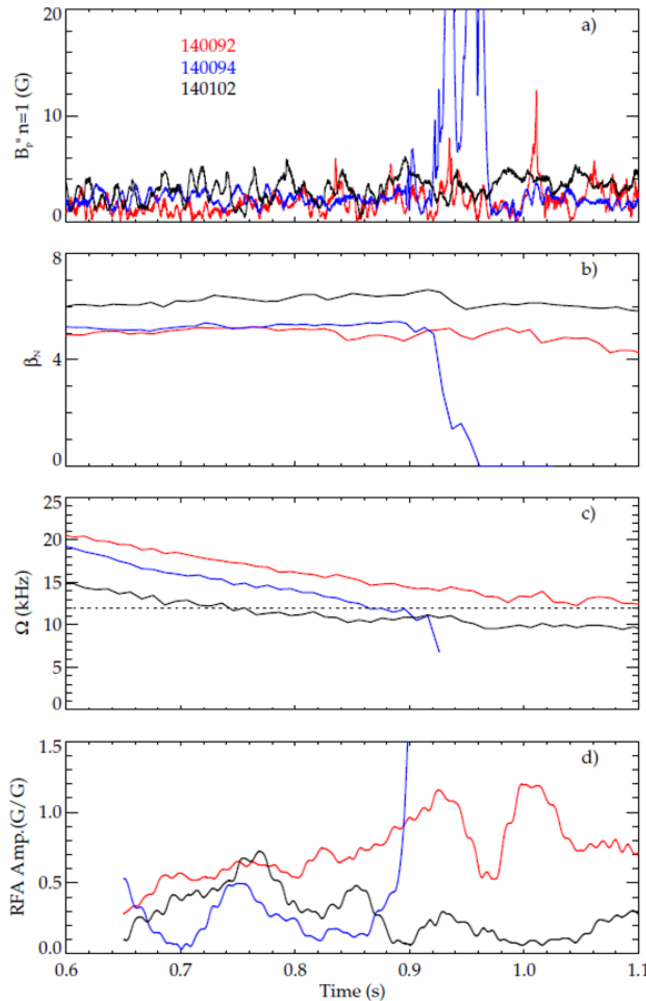


Figure MS-CU-4: Comparison of multiple NSTX discharges showing, a) $n=1$ signal on the upper poloidal magnetic field sensors, b) β_N , c) carbon toroidal rotation at CHERS channel 6 (near the core), and d) RFA amplitude, vs. time.

a new anisotropic term modifies the pressure-driven ballooning fluid term, and can be significant. The modified fluid δW was shown to maintain self-adjointness.

ITER advanced scenario discharges analyzed with the MISC code were previously shown to require the stabilizing effects of alpha particles to maintain RWM stability due to the low expected toroidal rotation in ITER (see Fig. 5 of Ref. MS-CU-4). However, low rotation in ITER may not be entirely detrimental to RWM stability. Stability analysis was performed on ITER advanced scenarios with internal transport barriers [MS-CU-5] that have strong internal gradients (see Figure MS-CU-5a). This can create a large ion diamagnetic frequency, ω_{*i} , which combined with relatively slow internal rotation can zero out the ExB frequency, $\omega_E = \omega_\phi - \omega_{*i}$ (Figure MS-CU-5b). The slow internal ω_E effectively allows resonance between the mode and slowly precessing particles. This is shown in Figure MS-CU-5b, where a linear rotation profile with 3kHz core rotation causes $\omega_E - \omega_D = 0$, and Figure MS-CU-5c, where $|\omega_E|^{-2}$ indicates where this precession resonance occurs. Combined with the more internal nature of the marginally stable eigenfunction for these plasmas (which resemble “infernal” modes [MS-CU-5]), strong kinetic stabilization can occur ($\text{Im}(\delta W_R)$ in Figure MS-CU-5c). Figure MS-CU-6 shows that when the rotation drops to a low enough level in this ITER case with an ITB, kinetic resonance occurs and stabilization without alpha particles is possible. Note that at higher rotation this ITER case is even less stable than a previous case without alphas (shown varied along the ordinate in Figure MS-CU-7).

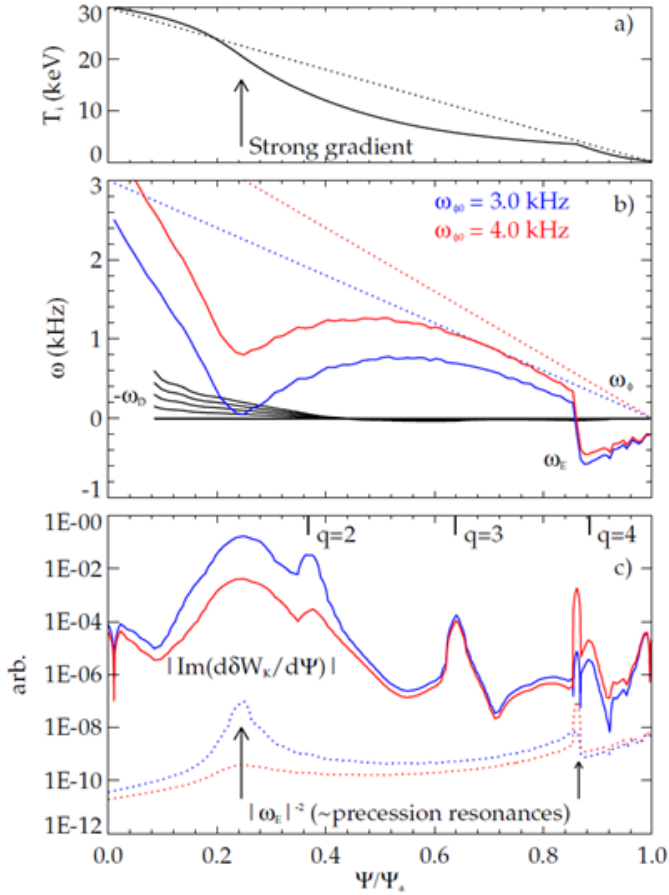


Figure MS-CU-5: a) T_i profile (with linear dashed line shown for reference), b) Linear toroidal rotation profiles, ω_ϕ , with 3 and 4 kHz core rotation, and the resulting ω_E profiles, c) $|\omega_E|^{-2}$ and MISK-calculated $|\text{Im}(d\delta W_K/d\Psi)|$ for $l=0$ trapped thermal ions, all vs. Ψ/Ψ_s .

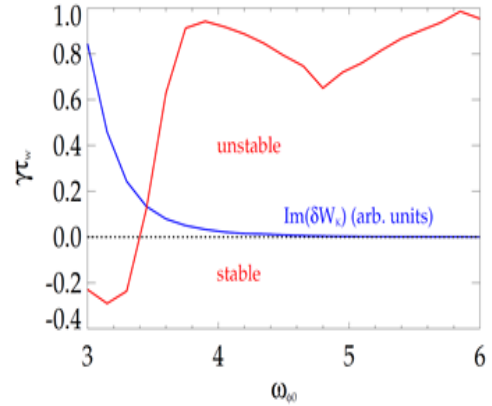


Figure MS-CU-6: Normalized growth rate, $\gamma\tau_w$, and $\text{Im}(\delta W_K)$ (in arb. units) vs. linear rotation profiles with core value $\omega_{\phi 0}$.

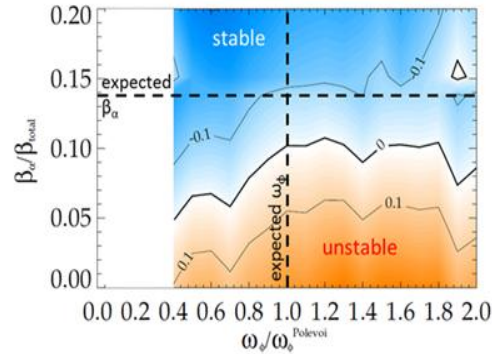


Figure MS-CU-7: RWM growth rate contours calculated with MISK vs. rotation and alpha particle β for ITER.

NSTX Joint Experiments: DIII-D

DIII-D kinetic RWM physics and resonant field amplification near marginal stability

A joint experiment between NSTX and DIII-D was conducted in 2012 (DIII-D MP2012-83-02). Columbia U. collaborators Dr. S.A. Sabbagh and Dr. J.W. Berkery participated in the two session, one day experiment with session leader Dr. J.M. Hanson of Columbia U. to further validate the kinetic RWM stabilization model quantitatively established on NSTX. Data was taken in 2012 using DIII-D's unique off-axis NBI capability, and also separately with NBI all injected on the device midplane. MHD spectroscopy using an $n = 1$ field (as described above as used in NSTX experiments) in a beta-controlled target of $\beta_N = 2.4$ was used to determine RWM stability from RFA for several plasma parameter variations including the amount off-axis NBI power, and toroidal field (Figure MS-CU-8). Additionally, the RFA was examined at substantially higher β_N , to examine the RFA behavior as the plasma approached the RWM marginal stability point. Plasmas were produced with β_N exceeding 3.5, and in this regime $n = 1$

RFA clearly increased to large magnitudes – 2-3 times the values reached in the lower β_N target. The higher normalized beta values exceed the nominal $n = 1$ no-wall stability limit. The $n = 1$ RWM amplitude increased to values exceeding 15 G with no strong tearing mode activity. At this point, higher frequency modes appeared (few kHz range), which either caused mode locking, or clamped the plasma $n = 1$ RFA. This activity, which precludes RWM instability in NSTX, is being investigated to determine if the perturbations are ideal or tearing. The present analysis has not yet conclusively shown RWM instability and the associated hard disruption limit observed in NSTX, but does establish a soft beta limit for DIII-D. Further analysis, and comparison with NSTX unstable RWM data, will focus on the scaling and physics that cause this limit.

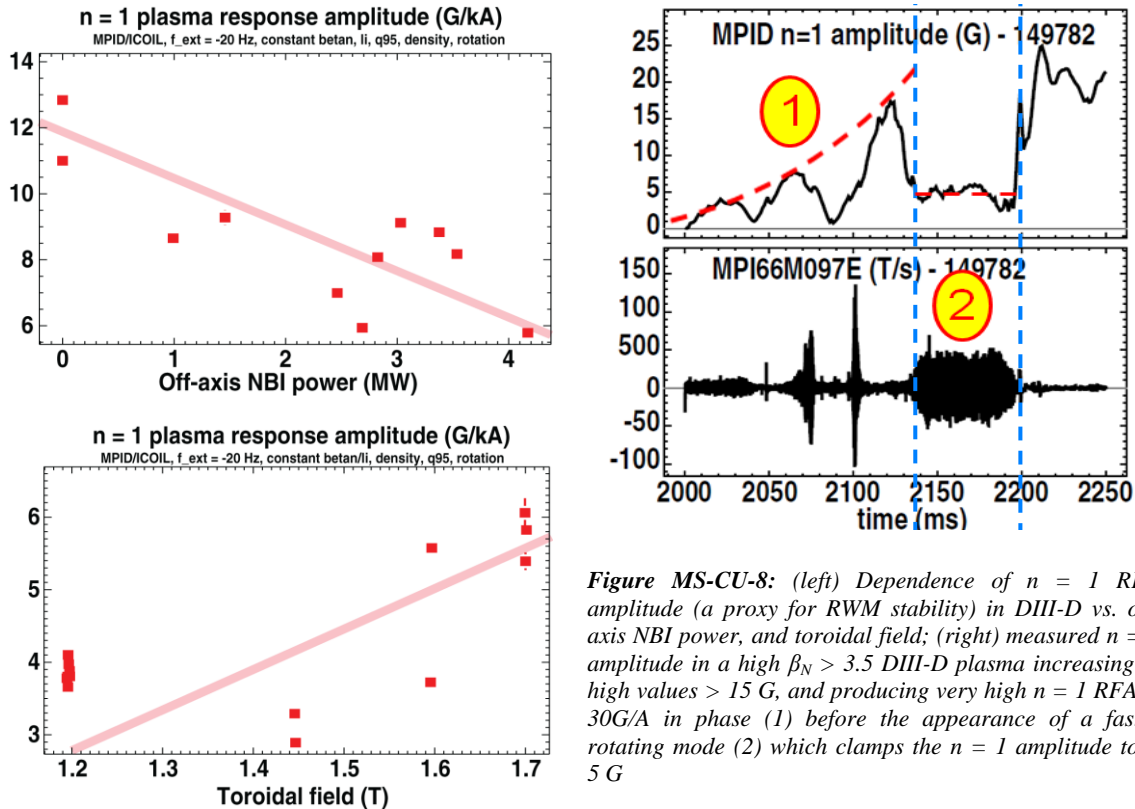


Figure MS-CU-8: (left) Dependence of $n = 1$ RFA amplitude (a proxy for RWM stability) in DIII-D vs. off-axis NBI power, and toroidal field; (right) measured $n = 1$ amplitude in a high $\beta_N > 3.5$ DIII-D plasma increasing to high values > 15 G, and producing very high $n = 1$ RFA > 30 G/A in phase (1) before the appearance of a faster rotating mode (2) which clamps the $n = 1$ amplitude to ~ 5 G

ITER Collaboration

RWM active control and error field correction – sensor/actuator control scoping studies

The ITPA/ITER Integrated Plasma Control Working Group, led by Dr. J. Snipes of the ITER Organization, has conducted a community-wide study of control system needs for ITER. Seventeen categories have been investigated. Dr. S.A. Sabbagh was chosen as the leader for the RWM Control, and Error Field Control categories. Significant contributions came from several NSTX researchers including Dr. Sabbagh, Dr. M. Bell, and Dr. J.-K. Park. Needs for RWM and error field correction actuators were determined, and needs for sensors were modified from past ITPA MHD Stability Working Group 4, led by Dr. J. Lister. The full report is available from the ITER Organization web site at: <https://user.iter.org/?uid=4DUHTS&version=v2.0>. An example of the calculations conducted for active RWM control is shown in Figures MS-CU-9 and

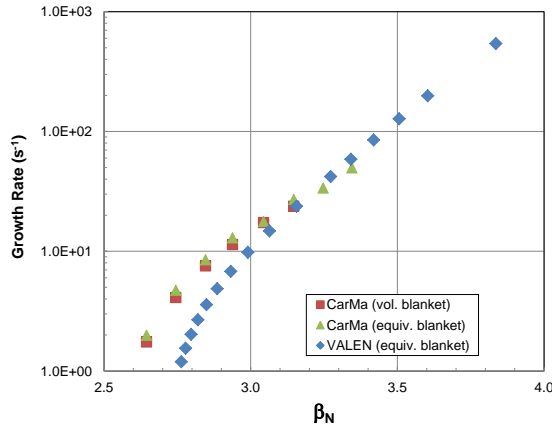


Figure MS-CU-9: RWM passive growth rate for ITER Scenario IV equilibria as computed by the CarMa and VALEN codes. Three curves are shown: (i) CarMa using a volumetric blanket model, (ii) CarMa using an equivalent blanket model made to match the RWM passive growth for the volumetric blanket model, and (iii) VALEN using a similar equivalent blanket model, including spaces in the wall model that match the blanket modules. Note that the differences between the codes are largely due to the VALEN calculation using a more recently computed for ITER Scenario IV equilibrium.

MS-CU-10. An important aspect of the study was the choice of a 3D thin shell blanket model that yielded equivalent control performance to a 3D volumetric blanket - this allowed a common, agreed point of comparison between the VALEN and CarMa codes (Figure MS-CU-9). In this study, the effect of sensor positions on RWM active control performance was determined. The sensors considered were chosen from the set planned for ITER. Several groups, including those targeted to be used for RWM control, were not the best options. A combination of sensors was computed to be superior based on their proximity to the plasma, inductive coupling to the plasma, and number of toroidal and poloidal positions. The dispersion curves for RWM active

control using different sensor sets are shown in Figure MS-CU-10.

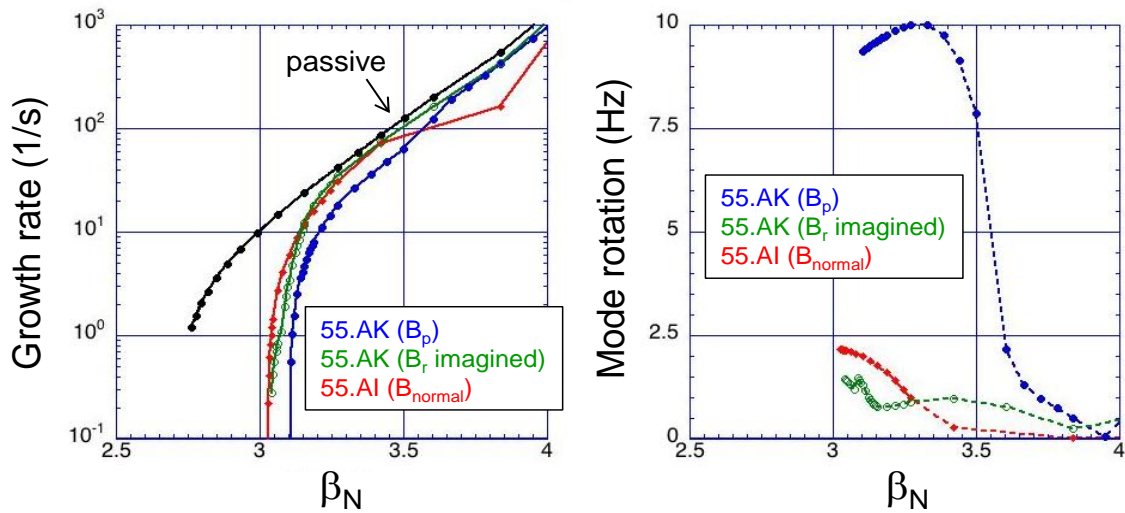


Figure MS-CU-10: (a) $n = 1$ RWM growth rate under active control (b) and natural mode rotation computations using planned sensors for ITER. Sensors considered are 55.AK measuring poloidal field perturbation, (imagined) 55.AK measuring radial field perturbation, and 55.AI saddle coils measuring normal field perturbation. Note that results use proportional gain feedback, and are not fully optimized. Calculations are from the VALEN code using the same wall and blanket model as in Figure MS-CU-9(iii).

Kinetic RWM analysis – ITPA MDC-2 Joint Experiment benchmarking activity

Benchmarking of the kinetic RWM stabilization physics in the MISK and MARS-K (Dr. Y. Liu) codes continued in 2012 under the auspices of the ITPA MHD Stability Group Joint Experimental Analysis Task MDC-2. The relevant frequencies and eigenfunctions now match between codes

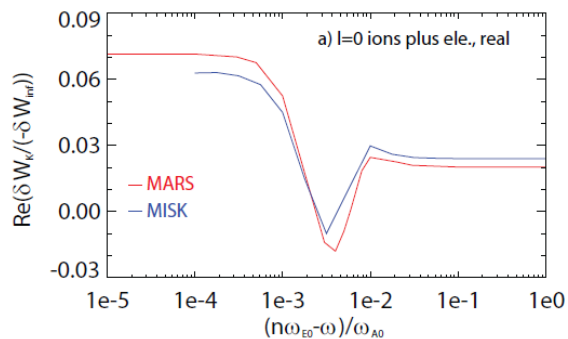


Figure MS-CU-11: Benchmarking comparison of δW_K for $l=0$ ions and electrons vs. scaled ω_E between MARS-K and MISK.

for both analytical Solov'ev and ITER equilibria. It was demonstrated that the numerical approach to the frequency resonance fraction energy integral taken in MISK is equivalent to analytical limits computed in MARS-K. MISK was upgraded to be able to take these analytical limits if desired as well as to separate out bounce harmonics ($l=0$ for precession drift resonance and $l \neq 0$ for bounce resonance). A comparison of δW_K for $l=0$ ions and electrons over a range of ExB frequency for a Solov'ev equilibrium found good agreement between the codes (Figure MS-CU-11).

KSTAR Collaboration

KSTAR stability experiments and analysis

Columbia U. Group research on NSTX is coupled directly to collaboration on KSTAR in common topical areas with complementary data sets. A summary of results and analysis from

areas covering the extended H-mode operational space, tearing mode characteristics, and predictions of active RWM control using the present KSTAR RWM sensors are described below.

The H-mode was more stably sustained in 2011 for longer durations up to about 5 s (H-modes were shorter than 2 s in 2010) with operational plasma current and toroidal field similar to the prior campaign, 0.6 MA and 1.6 - 2 T, respectively. In ohmically heated plasmas, 1 MA plasma current and a pulse length longer than 12 s were achieved. The expanded operating regime expressed in stability-relevant parameters (l_i , β_N) space is shown in Figure MS-CU-12. Progress toward desired operation at lower l_i and higher β_N in 2011 is shown and compared to data taken up to 2010. Compared to the first diverted H-mode achieved in 2010 with maximum $\beta_N = 1.3$, and $W_{tot} = 258$ kJ, $\tau_E = 148$ ms [MS-CU-6], equilibria have reached new high values for KSTAR, $\beta_N = 1.9$, $W_{tot} = 340$ kJ with a corresponding $\tau_E = 171$ ms. The maximum β_N was reached at B_T of 1.6 T. Plasma internal inductance was also reduced to 0.94 from 1.15 at peak β_N . The equilibrium enhancement toward higher values of $\beta_N/l_i > 2$ in 2011 without a substantial increase in auxiliary heating power from 2010 is significant. Enhanced energy confinement due to improved wall conditioning by boronization and higher bake out temperature (increased from 200°C up to 260°C on the carbon tile surface) has allowed this improvement. These results mark substantial progress toward the $n = 1$ ideal no-wall stability limit, computed for KSTAR projected equilibrium targets by the DCON code to be most closely positioned at $\beta_N = 2.5$, $l_i = 0.7$. An operating space plot of plasma elongation versus internal inductance (l_i , κ) is shown in Figure MS-CU-13. The internal inductance was lowered in 2011, which helped sustain higher operating κ by enhancing vertical stabilization. Although precise plasma shape control is still an important issue in the device, sustained elongation higher than the designed target value of 2.0 was achieved in many equilibria spanning $0.9 < l_i < 1.1$.

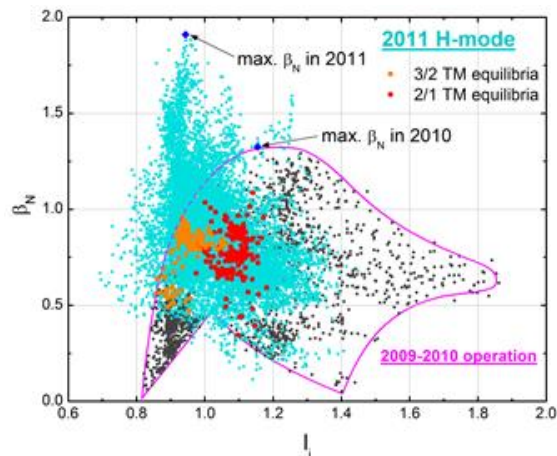


Figure MS-CU-12: KSTAR equilibrium operating space for 2011, and prior discharges. About 16,000 equilibria from 137 shots (93 shots from 2011) are shown. Expansion of the operating space in l_i and β_N is illustrated, along with the onset parameters for 3/2 and 2/1 tearing modes.

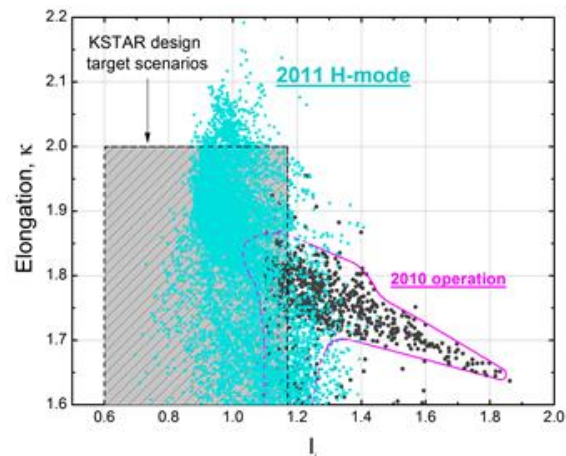


Figure MS-CU-13: Plasma elongation versus internal inductance of elongated equilibria for the present KSTAR database. A total of 111 full discharge evolutions during current flattop are shown.

Rotating MHD modes are observed with perturbations having tearing rather than ideal parity as determined by Mirnov and ECE [MS-CU-7] measurements. Modes with $m/n = 3/2$ (m structure by 2D ECEI [MS-CU-8]) onset at lower l_i than modes with $m/n = 2/1$ in the range $0.5 < \beta_N < 1$ as

shown in the expanded operating space in Figure MS-CU-12. The 3/2 modes are triggered during the H-mode phase but are relatively weak and do not substantially reduce W_{tor} . In contrast and surprisingly, 2/1 modes to date have not onset in H-mode. The modes only onset when both the stored energy and plasma rotation profiles are lowered after H-L back-transition with q_{95} ranging from 4.3 to 6.2 ($4.9 < q_{95} < 6.4$ for 3/2 modes) as shown in Figure MS-CU-14. Subsequent 2/1 mode locking creates a repetitive collapse of β_N by more than 50%. Onset behavior suggests the 3/2 mode is close to being neoclassically unstable while the 2/1 mode is not certain. Figure MS-CU-15 shows the 2/1 tearing mode amplitude dependence on local rotation shear measured by an X-ray imaging crystal spectrometer (XICS) [MS-CU-9]. A correlation is found between the mode amplitude and local rotation shear that impacts mode stability. Additionally (not shown in the figure), 2/1 modes only onset below local rotation shear values of $\sim 1,200$ km/s/m (~ 670 krad/s/m).

Computation of future active RWM control using the VALEN code examines control performance using present device sensors. Off-midplane saddle loops (SL) and midplane locked mode (LM) sensors are analyzed. Using saddle loop sensors, the mode can be stabilized up to β_N of 4.5 ($C_\beta = 86\%$) and up to 3.6 ($C_\beta = 44\%$) with/without compensation of the prompt applied field of the control coils from the sensors, respectively. The locked mode sensors are found to be strongly affected by mode and control coil-induced vessel current circulating around the elongated horizontal port penetrations facing the sensors, resulting in a reduced C_β of 37% and 16% with/without the prompt field compensation, respectively. Continued analysis is investigating improved control using LM sensors through compensation of the induced eddy currents.

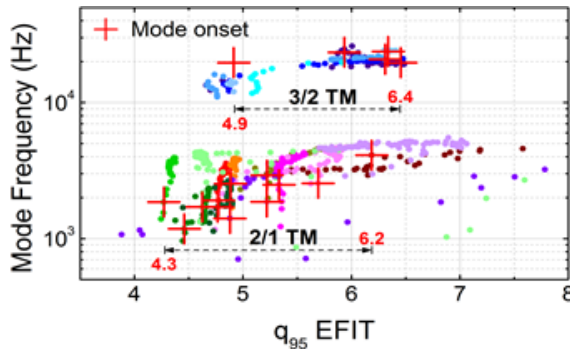


Figure MS-CU-14: Mode frequency vs. equilibrium q_{95} for 3/2 and 2/1 tearing mode evolutions.

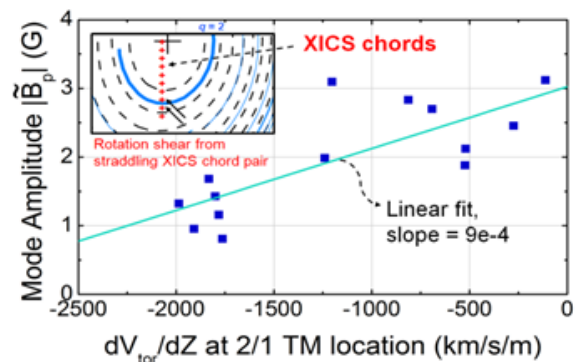


Figure MS-CU-15: Mirnov amplitude for 2/1 tearing mode vs. local rotation shear from XICS.

References

- [MS-CU-1] S.A. Sabbagh, J.W. Berkery, R.E. Bell, et al., Nucl. Fusion **50**, 025020 (2010).
- [MS-CU-2] H. Reimerdes, M.S. Chu, A.M. Garofalo, et al., Phys. Rev. Lett. **93**, 135002 (2004).
- [MS-CU-3] J. W. Berkery, S.A. Sabbagh, R. Betti, et al., Phys. Rev. Lett. **104**, 035003 (2010).
- [MS-CU-4] J. Berkery, S. Sabbagh, H. Reimerdes, et al., Phys. Plasmas **17**, 082504 (2010).
- [MS-CU-5] F. Poli, C. Kessel, M. Chance et al., Nucl. Fusion **52**, 063027 (2012).
- [MS-CU-6] Y.S. Park, S.A. Sabbagh, J.W. Berkery, et al., Nucl. Fusion **51** (2011) 053001.
- [MS-CU-7] Y. Kogi, T. Sakoda, A. Mase, et al., Rev. Sci. Instrum. **79** (2008) 10F115.
- [MS-CU-8] G.S. Yun, W. Lee, M.J. Choi, et al., Rev. Sci. Instrum. **81** (2010) 10D930.
- [MS-CU-9] S.G. Lee, J.G. Bak, U.W. NAM, et al., Rev. Sci. Instrum. **81** (2010) 10E506.

Error fields and mode locking physics

The IPEC applications to intrinsic error field corrections have been successfully extended to various tokamaks. Figure MS-EF-1 shows the compiled error field threshold scaling vs. critical density in locking, across five different tokamaks including L-mode and H-mode. Especially the new KSTAR and the revision of the old JET data increased the reliability of the size scaling, and the scaling is presently given by

$$\delta B_{21}/B_{T0} \cong 0.96 \times 10^{-4} (n_e [10^{19} m^{-3}])^{1.1 \pm 0.07} (B_{T0} [T])^{-1.4 \pm 0.09} (R [m])^{-0.60 \pm 0.16}.$$

This tokamak locking scaling will be updated for ITER prediction if further data are supplied.

The error field threshold based on the resonant field driving magnetic islands has been quite successful as shown, but recently it has also been found that this resonant picture can be incorrect if the residual non-resonant field is very large. In the so-called proxy error field experiments in DIII-D [MS-EF-1], one of the control coil, C-coil, was used to produce non-resonant error field, and another control coil, I-coil, was used to compensate the resonant part of the C-coil. This I-coil correction against C-coil did not work well and the optimal correction failed to reduce the locking density as expected. The IPEC and NTV analysis on this DIII-D proxy experiment indeed showed that the residual non-resonant field was increased by more than the sum of each, while

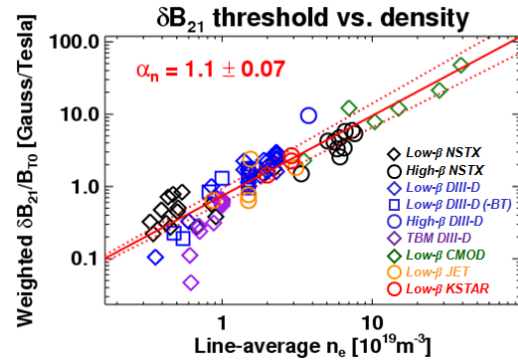


Figure MS-EF-1: Error field threshold scaling vs. critical density for locking across different tokamaks, including L-mode and H-mode plasmas.

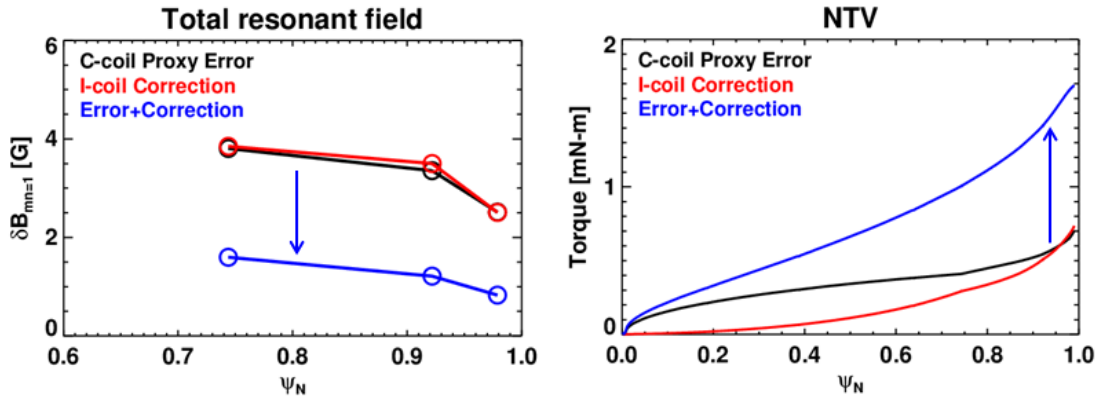


Figure MS-EF-2: IPEC and NTV analysis on the DIII-D Proxy error field experiments. The left figure shows the successful reduction of the resonant components as intended, but the figure on the right shows the non-resonant field and NTV is largely increased by more than the sum of each.

the resonant field was decreased by more than 50%, as shown in Figure 2. How to quantify these non-resonant effects in error field threshold will be challenging due to its non-linear nature, but will be attempted by looking into various special cases such as TBM mock-up experiments.

References

[MS-EF-1] R. J. Buttery et al., Phys. Plasmas 19, 056111 (2012)

Neoclassical Tearing Mode Stability Dependence on Aspect Ratio and Curvature

Toroidicity in a tokamak makes the total magnetic field on a flux surface vary poloidally so that it is stronger on the inboard side and weaker on the outboard side. Drift is added to particle gyrations and a fraction of particles are trapped on the outboard side in magnetic mirrors formed due to the poloidal variation of the magnetic field [MS-NTM-1]. A bootstrap current arises (carried by passing electrons) which is approximately proportional to the product of the trapped fraction and the electron pressure gradient [MS-NTM-2]. Neoclassical tearing modes (NTMs) are destabilized and sustained by helically perturbed bootstrap currents [MS-NTM-3]. At sufficiently high beta (ratio of volume averaged plasma pressure to magnetic field pressure), a linearly stable tearing mode if seeded by another MHD event can have the seed reinforced, a destabilizing effect that can lower the plasma magnetic energy. However, curvature effects, i.e. field line bending by the island, tend to raise the magnetic energy, a stabilizing effect [MS-NTM-4-8]; this is often called the GGJ effect after the original authors. The destabilizing helically perturbed bootstrap current is counter-acted by a number of effects at small island size; this tends to make an NTM linearly stable and non-linearly unstable, i.e., metastable [MS-NTM-3].

All of the toroidal effects depend on aspect ratio R/a , i.e., how spherical a tokamak is. While the GGJ effect is usually neglected at large aspect ratio [MS-NTM-3], time dependent modelling in the low aspect ratio device MAST confirmed its significance at low aspect ratio [MS-NTM-9-10]. In this DIII-D/NSTX work, experimental results are contrasted between the typical “high” aspect ratio DIII-D ($R/a=2.7$) and the low aspect ratio NSTX ($R/a=1.4$).

Both DIII-D and NSTX are run with near balanced double null divertor shapes of similar minor radius ($a \approx 0.6$ m), elongation ($\kappa \approx 2$), triangularity ($\delta_u \approx 0.4$ and $\delta_l \approx 0.7$) and cross sectional area (≈ 2 m²). The key parameter at issue is the local $q=m/n$ rational surface inverse aspect ratio ϵ (estimated as r/R_0 which comes from the dominant poloidal in/out asymmetry in B_T . Rigorously, toroidal effects come from the variation in total B which is used here). ϵ enters into the bootstrap drive, the GGJ curvature effect, and small island stabilizing effects. The experimental procedure in each device is: (1) raise beta in a high confinement H-mode to excite an $m/n=2/1$ mode, (2) “slowly” reduce neutral beam injection (NBI) power and thus beta, (3) stay in H-mode as power is reduced, (4) avoid the rotating $n=1$ mode locking to the resistive wall as torque is reduced with less NBI, and (5) reach the marginal point for self-stabilization, i.e., removal of the metastable parameter space.

For an island of full width w , the island growth rate is given by the Modified Rutherford Equation (MRE) [MS-NTM-11,12]:

$$\frac{\tau_R}{r} \frac{dw}{dt} = \Delta' r + C_R \frac{r D_R}{w} + \epsilon^{1/2} \frac{r L_q}{L_{pe}} \beta_{\theta e} \left[\frac{1}{w} - \frac{w_{\text{small}}^2}{3w^3} \right]$$

Here Δ' (in m^{-1}) is the classical tearing index and $C_R r D_R / w$ is the GGJ effect of assumed good average magnetic field curvature with dimensionless D_R the “resistive interchange parameter”. To

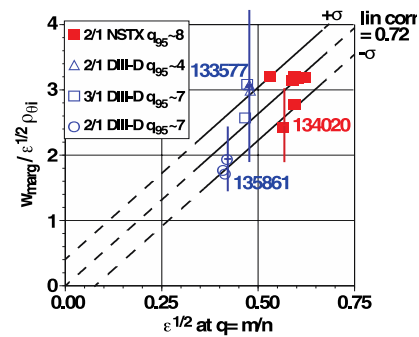


Figure MS-NTM-1. Ratio of the marginal island width to the ion banana width vs square root of the inverse aspect ratio.

leading order in inverse aspect ratio at the rational surface, $D_R \approx -(q^2 - 1)(L_q^2 / rL_p)\beta$ where L_q is the radial magnetic shear length, L_p is the total pressure gradient scale length, and $\beta = 2\mu_0 p / B_{T0}^2$ with p the local total pressure. $C_R = \mathcal{O}(1)$ is a constant of proportionality which can be modified by finite aspect ratio effects. The destabilizing bootstrap current drive term is $\varepsilon^{1/2}(rL_q / L_{pe}w)\beta_{\theta e}$ where $L_{pe} = (-p_e / dp_e / dR)$ and $\beta_{\theta e} \equiv 2\mu_0 p_e / B_{\theta}^2$ is the local electron beta poloidal. Finally, all of small island stabilizing effects [MS-NTM-13,14] are lumped together as w_{small} . The ratio of the marginal island width to the ion banana width is found to be experimentally well correlated with the square root of ε as shown in Fig. MS-NTM-1.

The inferred experimental sum of the $\Delta'r$ and curvature terms has also been computed, and there is a good correlation for NSTX with the curvature parameter rD_R/w . The linear fit (not forced through zero) extrapolates to about 0 at $rD_R/w = 0$. This suggests that $\Delta'r \approx 0.0 \pm 0.4$ to the one sigma of the fit and that the curvature term is the dominant stabilizing effect. In contrast to NSTX, the curvature parameter in DIII-D for all three cases is much smaller. This is confirmed by the NIMROD [MS-NTM-15] resistive MHD stability code which calculates the resistive interchange stability parameter D_R in full shaped geometry [MS-NTM-7]. D_R from NIMROD is close to the large aspect ratio expansion analytic formula for NSTX, but NIMROD finds D_R in DIII-D is 3~5 times a bigger effect than that of the expansion formula. However, curvature stabilization is found to still be relatively small in DIII-D. The NSTX case is found by NIMROD to have a significant stabilizing curvature effect comparable to that of a negative $\Delta'r$ (not directly calculated), but not dominant. The DIII-D cases are found to be $\Delta'r$ dominated. More on all this work has recently been published [MS-NTM-16].

References

- [MS-NTM-1] J. Wesson, Tokamaks 2nd ed., 124-131, 166-168, (Clarendon Press-Oxford, 1997)
- [MS-NTM-2] O. Sauter et al. Phys. Plasmas 6, 2834 (1999)
- [MS-NTM-3] R.J. La Haye Phys. Plasmas 13, 055501 (2006)
- [MS-NTM-4] A.H. Glasser et al. Phys. Fluids 18, 875 (1975)
- [MS-NTM-5] A.H. Glasser et al. Phys. Fluids 19, 567 (1976)
- [MS-NTM-6] S.E. Kruger et al. Physics of Plasmas 5, 455 (1998)
- [MS-NTM-7] C.C. Hegna, Phys. Plasmas 6, 3980 (1999)
- [MS-NTM-8] H. Lütjens and J.F. Luciani, Phys. Plasmas 8, 4267 (2001)
- [MS-NTM-9] R.J. Buttery et al. Phys. Rev. Lett. 88, 125005 (2002)
- [MS-NTM-10] R.J. Buttery et al. Nucl. Fusion 44, 1027 (2004)
- [MS-NTM-11] R.J. La Haye et al. Phys. Plasmas 17, 056110 (2010)
- [MS-NTM-12] R.J. La Haye et al. and the DIII-D Team, Nucl. Fusion 51, 053013 (2011)
- [MS-NTM-13] R. Fitzpatrick, Phys. Plasmas 2, 825 (1995)
- [MS-NTM-14] F.L. Waelbroeck et al. Phys. Rev. Lett. 87, 215003-1 (2001)
- [MS-NTM-15] C.R. Sovinec et al. Phys. Plasmas 10, 1727 (2003)
- [MS-NTM-16] R.J. La Haye et al., Phys. Plasmas 19, 062506 (2012)

Disruption Halo Current Studies

Research in the past year has refined our understanding of halo currents in the NSTX lower divertor; these are currents that flow between the plasma and the divertor during a disruption, and that can cause significant damage due to the forces they exert on the vessel and divertor components. These studies were made possible by the installation of a toroidal array of “shunt tiles” in the NSTX lower divertor that can measure the current flowing into individual tiles.

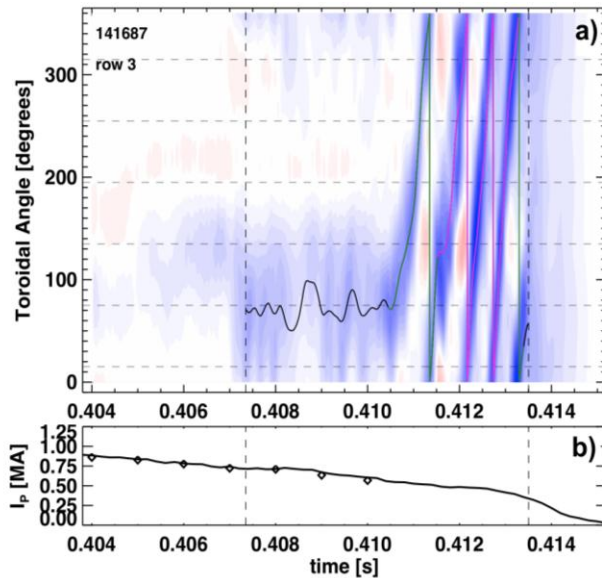


Figure MS-HALO-1: (a) contours of current flowing into the divertor floor and (b) plasma current during large halo current during a disruption in NSTX.

the dominant spatial structure of the halo currents is a single, toroidally localized lobe of current, regardless of whether the pattern is rotating or stationary. Secondly, the temporal dynamics of this lobe can vary rapidly, even over the ~ 6 ms duration of the halo current pulse, examples of rapidly varying quantities include the rotation frequency and toroidal extent of the lobe. Finally, the halo currents are observed to decay in a toroidally symmetric fashion at the end of the pulse, starting at $t=0.4135$ s. Modelling indicates that the magnetic axis has been almost completely driven into the divertor floor, leaving behind residual open field line current.

Disruption Detection

Recent research in NSTX has examined the detectability of disruption in a high- β spherical torus. This research has proceeded in two steps. First, the ability of individual sensor signals to predict a disruption has been examined. Then, a simple means of combining these single-signal tests has been developed.

Example results for a “single signal” test are shown in Fig. MS-DD-1. In frame a), the time between the $n=1$ RWM sensors reaching a threshold value and the initiation of the current quench

Figure MS-HALO-1a shows contours of current flowing into the divertor floor, as a function of time and toroidal angle, while Figure MS-HALO-1b) shows the plasma current rapidly decreasing to zero during the disruptions. At $t\sim 0.407$, current begins to flow into the divertor; this current is largely localized to half of the shunt tiles. However, at $t=0.41$, the observed halo current pattern begins to rotate toroidally, completing approximately 4 toroidal revolutions. Up to 8 toroidal revolutions have been observed in rare cases.

Two key observations come from this and similar measurements. First,

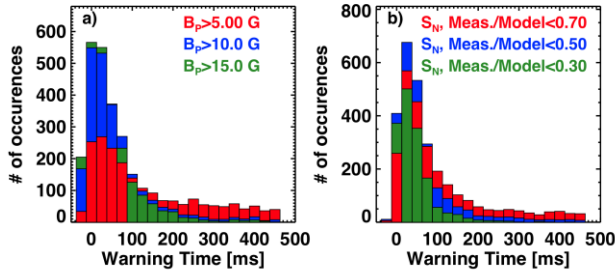


Figure MS-DD-1: Histograms of time between thresholds being crossed and the current quench. Tests are based on a) $n=1$ poloidal field sensors, and b) the neutron rate.

level to 10 and 15 G reduces the false positive count, at the expense of more late warnings. In frame b), the ratio of the measured neutron emission rate to the prediction from a simple, rapidly evaluated model for the neutron emission is used for disruption detection. The time between that ratio dropping beneath a given threshold value and the initiation of the current quench is recorded, for various values of the threshold. A threshold ratio (measured/model) of 0.7 often leads to false positives, while thresholds of 0.5 and 0.3 reduce the false positive count. However, these two frames show that no single signal can be used to predict all disruptions.

In order to test the ability of a combined set of tests to predict disruptions, we have developed a simple algorithm that combines the output of single-signal tests like those described above. In this case, a “point score” is assigned to each test, and the total points from 17 such tests are summed at each time slice to determine a aggregate warning level; different values of this aggregate warning level can be chosen, trading off false positives and late warning. Fig. MS-DD-2 shows an example output of this study, showing that for the chosen warning level threshold, only ~2% of disruptions cannot be detected within 10 ms, and that only 4% of discharges are false positives. Furthermore, this false positive count is dominated by discharges with severe MHD modes, which cause severe rotation damping and stored energy loss, but no current quench.

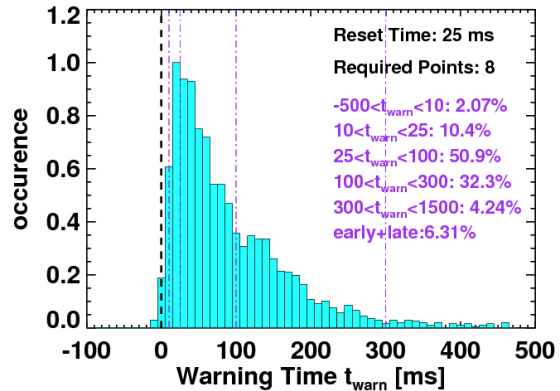


Figure MS-DD-2: Histogram of warning times based on the combination of tests.

is plotted, for a database of ~1700 H-mode disruptions; this time is called the “warning time”, with negative values implying that the current quench proceeded the sensor exceeding the threshold. We see that a warning level of 5 Gauss produces many false positives, here defined as a warning more than 300 ms in advance of the current quench. Increasing the warning

Disruptivity Studies

Research in NSTX during 2012 attempted to determine what discharge regimes resulted in minimum disruptivity. Here disruptivity is defined as the number of disruptions when the plasma is in a given portion of parameter space, normalized by the amount of time that the plasma is in that space. Figure MS-DR-1 shows the disruptivity in NSTX as a function of β_N and a single additional parameter. In frame a), the additional parameter is $q^* = \varepsilon\pi a B_T (1 + \kappa^2) / \mu_0 I_p$. We see a rapid increase in disruptivity for $q^* < 2.4$, but no increase in disruptivity at higher β_N . Note that this is higher than the ideal MHD q^* boundary of ~ 1.7 . The reason for this increase in disruptivity is a wide range of

operational problems at the highest current or with low shaping. It should be noted that attempts to access this very low q^* regime have been limited in the campaigns under consideration here, although they were more common in the initial years of NSTX operations. Frame b) shows the disruptivity vs. β_N and shape parameter $S = q_{05} I_p / a B_T \propto \varepsilon (1 + \kappa^2) f(\kappa, \delta, \varepsilon, \dots)$; boundary shapes with low aspect ratio, high elongation, and high triangularity, all of which are typically beneficial for stability, will have large values of S . The figure does indeed show a great reduction of disruptivity with shaping. Finally, Fig. MS-DR-1c) and MS-DR-1d) show the disruptivity vs. two parameters related to the peaking of the profiles: the pressure peaking, defined as the central pressure normalized to the volume averaged pressure $F_p = p_0 / \langle p \rangle$, and the internal inductance $l_i(1) = l_p^2 \iiint B_p^2 dV / V (\mu_0 I_p)^2$. These quantities are larger when the pressure and current profiles are more peaked. We see clearly that operating at large pressure peaking, especially at higher values of β_N , results in a strong increase in disruptivity. Note that increases in the pressure peaking are well known to result in reduction to the ideal stability limit. Similarly, while higher l_i generally increases the no-wall limit for broad pressure profiles, NSTX often operates in the wall-stabilized regime, where broad current profiles improve the coupling to passive conductors.

This analysis has included other parameters as well. It is found that maintaining the mid-radius rotation above ~ 7 kHz helps avoid disruptions, as does the use of $n=1$ RWM control and dynamics error field correction. Maintaining $q_{\min} > \sim 1.3$ helps to avoid the onset of disruptive core $n=1$ modes. This research shows that a combination of strong shaping, broad profiles, sustained rotation, and elevated q_{\min} can be used to minimize the disruptivity. By, using the new

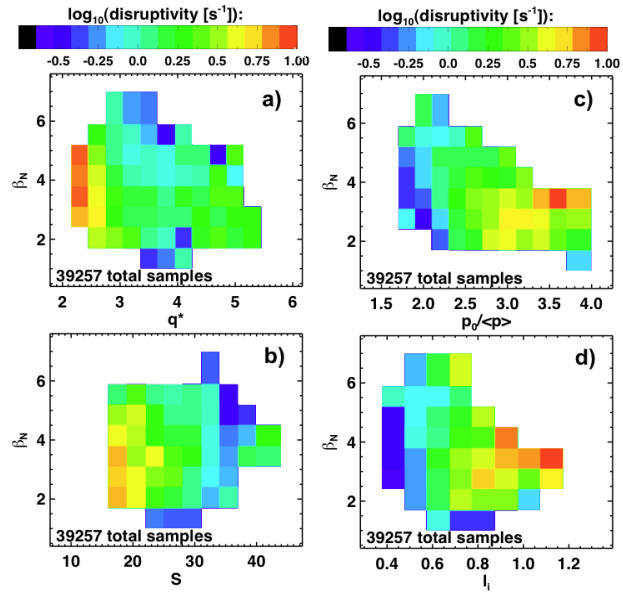


Figure MS-DR-1: Disruptivity as a function of β_N and a) q^ , b) shape factor, c) pressure peaking factor, and d) internal inductance.*

actuators of NSTX-U with advanced control techniques, we will study how to maintain this optimal state for long pulse in NSTX-U.

Disruption Mitigation Studies

Simulations using the DEGAS-2 code

In support of Massive Gas Injection (MGI) studies in NSTX-U, we are conducting DEGAS-2 simulations to better characterize the gas penetration physics and to improve the design of the MGI gas deliver system on NSTX-U.

A review of the literature [MS-DM-1,2,3] shows that the amount of gas injected in MGI experiments in present tokamaks varies from $100 \text{ Pa}\cdot\text{m}^3$ to over $2000 \text{ Pa}\cdot\text{m}^3$, considerably less than the projections for ITER. The fraction of this gas that penetrates the separatrix also varies widely, with penetration efficiencies of over 20% being reported for cases that have a short MGI pulse [MS-DM-4]. To better quantify the amount of gas required in a MGI pulse we have initiated a DEGAS-2 Monte-Carlo code simulation effort to understand the extent of gas penetration through the SOL region and private flux regions. In addition to supporting NSTX-U needs, this simulation effort focuses on fundamentally studying the edge penetration issues to the separatrix, which is needed for predicting gas penetration efficiencies in ITER. This work complements other 3-D MHD modeling, initiated by the ITER organization, of the gas dissipation inside the separatrix..

The results presented here are preliminary, and at an early stage with the goal of eventually incorporating some of the important physics that is required for a more complete model. The code employed is not yet capable of simulating energetic SOL flows and so does not yet correctly reflect edge conditions that would exist in a high power discharge. A higher energy plasma in the SOL would increase the gas ionization rate in this region and reduce gas penetration. Development of the detailed modeling of the edge SOL flows is underway but may be beyond the scope of our limited manpower capability.

As the first step in developing the full model to simulate the effect of increasing the SOL parameters we have conducted simulations in which the background plasma density and temperature are artificially increased, such as would happen when the auxiliary power of a plasma discharge is increased. In these simulations, deuterium molecules are launched at the injection port with a 300 K thermal energy distribution and a cosine angular distribution about the normal to the surface. As the molecules penetrate the plasma, they undergo ionization, dissociation, and elastic scattering; resulting molecular ions are assumed to be ionized, dissociated, or recombined immediately. Any product atoms are then tracked through the plasma and can undergo ionization and charge exchange [MS-DM-5,6,7]. The particle track terminates upon ionization of the atom. Along the particles' paths, the volumetric source of plasma ions is accumulated in each computational zone. The penetration fraction is then the ratio of the volume integrated sum of those source rates over zones inside the separatrix to the gas puff rate.

For these simulations plasma parameters from NSTX discharge 128339, a lower single null 1 MA discharge with 1 MW of neutral beam power was used. The computational mesh needed for DEGAS-2 has been generated by the UEDGE code [MS-DM-8,9] for this discharge and was previously used in a different study [10]. Plasma conditions at 300 ms are used. At the midplane,

the total mesh width is 5.5 cm. The outer edge of the mesh is 8.1 cm from the vessel wall, which is also the location for the mid-plane gas injection location. The separatrix is located 9.9 cm from the gas puff location. Outside the UEDGE mesh, between that mesh and the vessel wall, there is a coarser DEGAS-2 mesh. Here, DEGAS-2 subroutines break the background region into a series of small interlocking triangles. Within each of these triangular “zones”, all parameters (source rates, densities, temperatures, etc.) are constant.

The background plasma is located between the UEDGE mesh and the vessel walls. In this region, a reference plasma density of $5 \times 10^{18} \text{ m}^{-3}$ and electron temperature of 25eV was assumed. The background plasma density and temperature were each then increased to 2 times, 5 times and 25 times the reference values.

Figure MS-DM-1 shows the deuterium ionization rate for the four cases. The vertical line marks the location of the separatrix. The rapidly decreasing ionization rate inside the separatrix for the cases with background plasma means that there is that much less neutral deuterium in this region for ionization.

Because the ionization fraction would depend both on the plasma parameters and the depth over which this condition exists, this study should crudely approximate the effect of increasing SOL

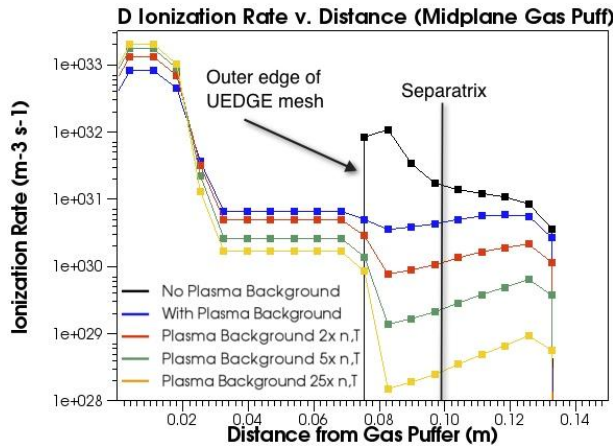


Figure MS-DM-1: Ionization rates for the case of mid-plane gas injection with increasing plasma density and temperature in the region between the outer UEDGE mesh and vessel walls. The ionization rates are for a molecular deuterium injection rate of 10^{30} molecules/s.

density and temperature. The results show that the gas penetration fraction drops dramatically even for a factor of two increase in the plasma parameters. The gas penetration fraction is 33% for the case with no background plasma. It drops to 16% for the case with the reference plasma and to 7%, 3% and 1% respectively for the cases of increasing plasma density and temperature.

These results would suggest that more energetic plasma conditions in the SOL should make it more difficult for gas injected from the mid-plane to penetrate past the separatrix. However, if gas is injected directly into the private flux region, and does not need to cross the

SOL, the penetration fraction should be higher so long as the private flux region plasma is much less energetic than plasma in the SOL. This should be the case as the bulk of the exhaust power from tokamak plasmas flows through the SOL, eventually being deposited on divertor plates.

To put this in perspective, the private flux region in ITER is predicted to have an electron temperature of less than 2eV and an electron density of below $2 \times 10^{20} \text{ m}^{-3}$ [MS-DM-11]. Representative values for these two parameters for detached DIII-D plasmas are an electron temperature of less than 1eV and electron density less than $5 \times 10^{19} \text{ m}^{-3}$ [MS-DM-12]. The relatively low electron temperature in the private flux region in both ITER and DIII-D is due to active gas puffing in the divertor region to obtain a detached divertor configuration, which is

necessary to reduce divertor heat loads. The electron temperature and electron density in the SOL at the mid-plane region of ITER is predicted to be about 100eV and $2 \times 10^{19} \text{ m}^{-3}$ [MS-DM-13]. The corresponding values for DIII-D are an electron temperature less than 20eV and an electron density less than $3 \times 10^{18} \text{ m}^{-3}$ [MS-DM-14]. The parameters for the NSTX-U could be expected to be similar to those for DIII-D.

In summary, the planned experiments and simulations are expected to contribute to the understanding of important physics questions related to the MGI experiments in support of NSTX-U, ITER and future ST based machines. The primary study to be conducted would be to understand the gas penetration efficiency as a function of poloidal gas injection location and variations in plasma parameters, especially at the edge. The second objective would be assessing the resulting reduction in divertor heat loads and halo currents. Supporting DEGAS-2 studies would contribute to quantifying the MGI system requirements aimed at minimizing the gas throughput and maximizing the gas penetration through the separatrix.

Development of Electromagnetic Particle Injector (EPI) for NSTX-U and ITER

This section describes on-going work for developing a new system for safely terminating discharges in ITER. The system, referred to as an Electromagnetic Particle Injector (EPI) propels a coaxial projectile, containing particulate matter of various sizes and composition, in a coaxial electromagnetic rail gun, then shatters it prior to injecting a dust of particles into the tokamak. At present this is a design activity that will be completed by December 2012. After that the plans will be discussed with NSTX-U management and the US-DOE to obtain guidance on how to proceed with the next step, which involves fabricating a proto-type and testing it off-line during 2013.

At the recent US Disruption Mitigation Workshop (GA, March 12-13, 2012) it was concluded that although the Massive Gas Injection system is the best understood for safely terminating discharges in ITER, both the time response of this system and the controllability of the amount of gas and impurities injected by this system for variations in the initial plasma current at which a disruption initiates may be inadequate to fully rely on this system. It was decided that other faster acting systems should also be tested and developed. During this meeting, we presented the EPI concept. It was noted that this system was more complex as compared to a conventional gas gun, but no technical flaws were identified. It was also suggested that a proto-type should be built and tested before considering it for ITER.

The proposed system, shown in Figures MS-DM-2 and MS-DM-3, is now under design. It has several advantages over other disruption mitigation systems being considered for ITER.

- Well suited for long stand-by mode operation
 - Large particle inventory
 - All particles are delivered at nearly the same time
 - Particles are tailored to contain multiple elements in different fractions and sizes
 - Tailored particles fully ionized only in higher current discharges (to control current quench rates)

- Toroidal nature and conical disperser ensures that,
 - The capsule does not enter the tokamak intact
 - The capsule will fragment symmetrically and deliver a uniform distribution of particles (or via tapered final section)
 - Particle penetration is not impeded by magnetic fields
- Coaxial Rail Gun is a fully electromagnetic system with no moving parts, so should have high reliability from long stand-by mode to operate on demand
 - Conventional gas guns will inject gas before capsule and trigger pre-mature thermal quench

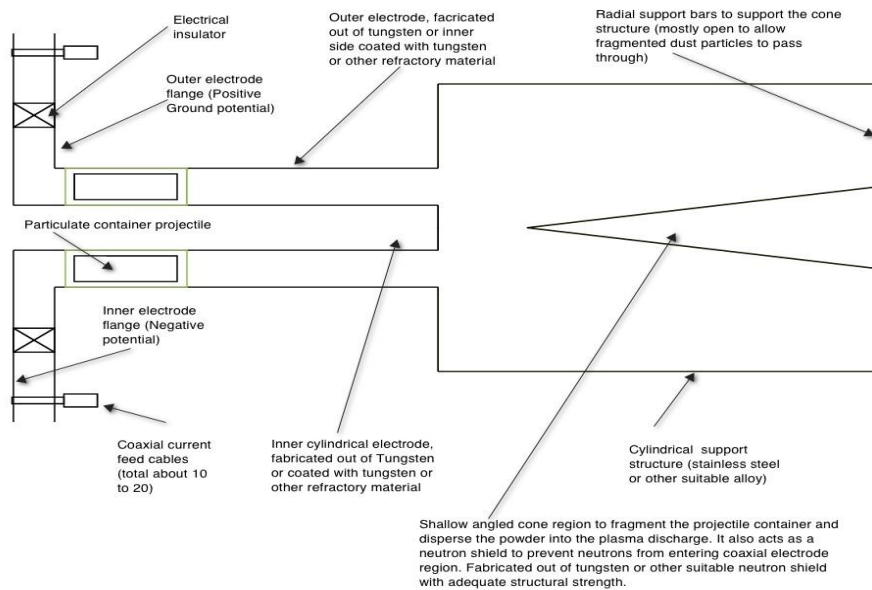


Figure MS-DM-2: Electromagnetic Particle Injector (EPI) using a coaxial electromagnetic rail gun

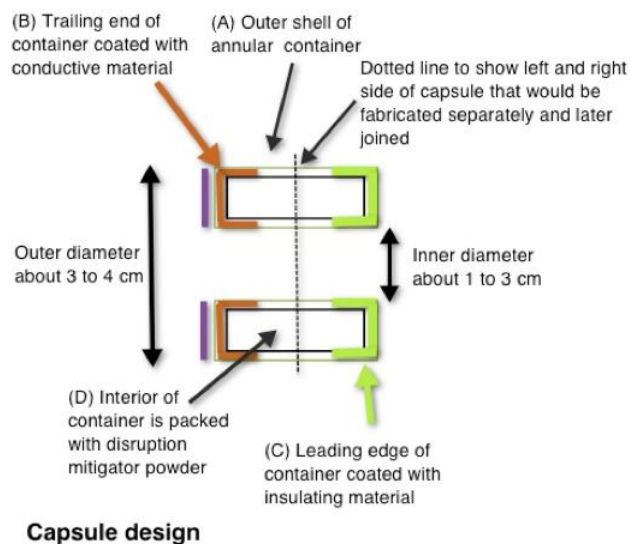


Figure MS-DM-3: Shown are the primary elements of the capsule design. The purple ring at the trailing end of the capsule serves two purposes. In an electromagnetic accelerator it is used to increase the inertial strength of the capsule. If the capsule is used in a conventional gas gun it could be fabricated out of a non-conductive material.

References

- [MS-DM-1] D. G. Whyte, et al., Journal of Nuc. Materials, **363-365** (2007) 1160-1167
- [MS-DM-2] G. Pautasso, et al., Plasma. Phys. Cntrl. Fusion **51** (2009) 124056
- [MS-DM-3] E.M. Hollmann, et al., Physics of Plasmas **17**, 056117 (2010)
- [MS-DM-4] D.G. Whyte, D.A. Humphreys, A.G. Kellman, Fus. Sci.Tech., **48** (2005) 954
- [MS-DM-5] D. P. Stotler and C. F. F. Karney, Contrib. Plasma Phys. **34**, 392 (1994).
- [MS-DM-6] D.P. Stotler, et al., J. Nucl. Mater., **196-198** (1992) 894
- [MS-DM-7] D. P. Stotler, C. S. Pitcher, C. J. Boswell, B. LaBombard, J. L. Terry, J. D. Elder and S. Lisgo, in "Atomic Processes in Plasmas, 13th APS Topical Conference on Atomic Processes in Plasmas", (Gatlinburg, Tennessee, April 22–25, 2002) (American Institute of Physics, Melville, New York, 2002), p. 251
- [MS-DM-8] T.R. Rognlien, et al., Contrib. Plasma Phys. **34** (1994) 362
- [MS-DM-9] T.R. Rognlien, et al., J. Nucl. Mater. **266-269** (1999) 654
- [MS-DM-10] D. P. Stotler, R. Maingi, L. E. Zakharov, H. W. Kugel, A. Yu. Pigarov, T. R. Rognlien, and V. A. Soukhanovskii, Contrib. Plasma Phys. **50**, 368 (2010)
- [MS-DM-11] V. Kotov, D. Reiter and A.S. Kukushkin, "Numerical study of the ITER divertor plasma with the B2-EIRENE code package," Bericht des Forschungszentrums Julich, Jul-4257, November (2007)
- [MS-DM-12] S.L. Allen, Rev. Scientific Instrum. **68** (1997) 1261
- [MS-DM-13] A.S. Kukushkin, et al., Nuclear Fusion, **47** (2007) 698
- [MS-DM-14] D.L. Rudakov, et al., Nuclear Fusion, **45** (2005) 1589

Transport and Turbulence Physics Research

In FY2012, NSTX transport and turbulence studies, in the absence of operation, focus on analyzing existing data and performing experiment-theory comparisons. In supporting FY2012 JRT, a specific emphasis was to simultaneously assess turbulence and transport in electrons and particles.

Collisionality Scan in H-mode

a. Energy transport

It was recently found that the unlithiated and lithiated discharges in NSTX scale differently with engineering parameters; the lithiated discharges revealed confinement dependences on I_p and B_T that are dissimilar from the early NSTX observations, but which are similar to those in conventional aspect ratio tokamaks, as embodied in the ITER98y,2 scaling, scaling as $I_p^{0.86} B_T^0$ [TT-1]. Now we find that these differing dependences could be reconciled by an underlying collisionality variation, which unifies both sets of data and which exhibits a strong improvement of normalized energy confinement with decreasing ν_e^* [TT-2].

The discharges used for this study are all H-modes based on I_p , B_T scans in both lithiated and unlithiated plasmas, and a lithium deposition scan at fixed I_p and B_T . The unlithiated discharges cover the range of I_p from 0.7 to 1.1 MA, B_T from 0.35 to 0.55 T, had deuterium neutral beam (NB) heating powers of ~ 4 MW into Lower Single Null (LSN) deuterium plasmas, elongation, κ , ~ 2.2 and plasma densities up to $6 \times 10^{19} \text{ m}^{-3}$. All of these discharges exhibited small ELMs, which did not affect confinement significantly. The lithiated discharges were obtained from results of several different experiments, all in the LSN configuration. I_p and B_T scans were performed in sets of discharges for which the between-shots lithium evaporation was held to between 90 and 270 mg. These discharges covered the range $I_p=0.7$ to 1.3 MA, $B_T=0.34$ to 0.54 T, $\kappa \sim 2.3$, and had NB heating powers of approximately 3 MW. Another set of discharges was taken from a lithium evaporation scan (Li scan), covering the range from 0 to 1000 mg of lithium evaporated between shots at fixed $I_p=0.8$ MA, $B_T=0.44$ T and $\kappa=1.8$. The NB heating power in this latter set varied from 2.2 to 4.2 MW. While there were repetitive Type I ELMs at low levels of lithium, the ELMs disappeared at higher levels [TT-3]. Confinement and transport levels for the analysis presented here were taken during inter-ELM periods (for lower deposition values), and thus the direct effect of ELMs was removed.

The primary reason for the strong improvement in confinement time with decreasing collisionality was the broadening of the temperature profile with decreasing ν_e^* . Figure TT-1a and 1b show the how T_e changes with changing collisionality. Fig. TT-1(a) shows the color-coded sequence of T_e profiles themselves, plotted as a function of the square root of the normalized toroidal flux, x , while Fig. TT-1(b) is a spectrogram of the T_e profile as a function of x and ν_e^* . This data was taken from a collection of lithiated and unlithiated discharges in which dimensionless parameters other than ν_e^* were held as fixed as possible. For this series, $q_{r/a=0.5} = 2$ to 2.5 and $\langle \beta \rangle$ was between 8.5 and 12.5%. Both panels clearly show the broadening of the T_e profiles with decreasing collisionality.

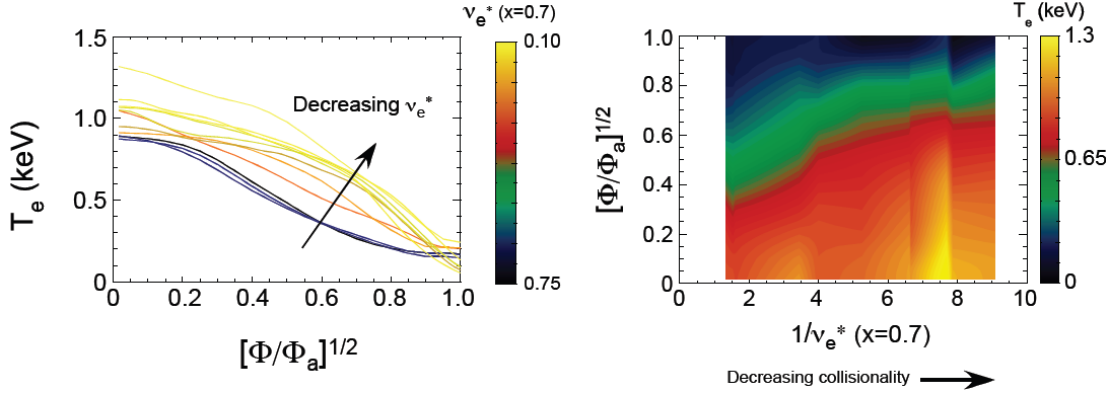


Figure TT-1: (a) T_e profiles color coded by collisionality and (b) T_e profile contour plot.

The electron temperature profile broadening reflects a progressive reduction in the electron thermal diffusivity in the outer region of the plasma as collisionality decreases. The decrease of the electron thermal diffusivity can be seen clearly in Fig. TT-2(a). The curves are color-coded to be proportional to the collisionality for that discharge within the collisionality range studied. As can be seen in the figure, the electron thermal diffusivities decrease by approximately an order of magnitude over the range of collisionality at $x=0.7$, going from 10 m^2/s at the highest collisionality to 1 m^2/s at the lowest.

The change in electron thermal diffusivity with collisionality can also be examined in a relative sense by normalizing χ_e to $\chi_{e,\text{gyroBohm}} = \rho^{*2} c_s/a$. This normalization takes into account changes in ρ^* and ion sound speed c_s due to changes in T_e to reflect the transport levels relative to what may be expected by gyroBohm transport. The profiles of $\chi_e/\chi_{e,\text{gyroBohm}}$ are shown in Fig. TT-2(b) in arbitrary units, and similar to the trend observed for χ_e alone, the normalized transport also decreases approximately an order of magnitude.

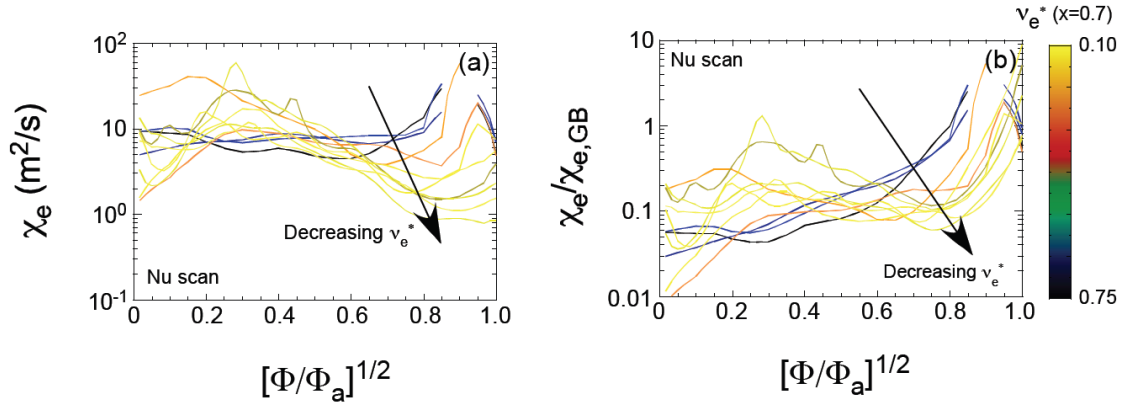


Figure TT-2: (a) Electron thermal diffusivity profiles and (b) χ_e normalized by $\chi_{e,\text{gyroBohm}}$ in arbitrary units color coded by collisionality

Ion transport behaves differently from that of electrons. A comparison of the ion thermal diffusivity to the neoclassical ion thermal diffusivity as computed by NCLASS for both scans at $x=0.60$ shows that at the highest collisionality, $\chi_i/\chi_{i,\text{neo}} \sim 0.5$, which we take to be at a neoclassical level when the differences among neoclassical theories and the uncertainty in χ_i are taken into

account and the ions become more anomalous, reaching a factor of four to five at lowest collisionality. The increase of ion thermal transport at lower collisionality is found to be correlated with reduction of local flow shear at low collisionality.

b. Impurity transport

The transport of carbon is determined with respect to predicted neoclassical transport. Departures between measured (measured on the low field side) and predicted profiles are possible indications of anomalous (i.e., turbulence-driven) processes. The tools used for the impurity transport calculations include MIST [TT-4] and NCLASS [TT-5], the latter two describing local and non-local neoclassical transport respectively. One of the approaches taken is to use interpretive/predictive MIST runs in which experimental profiles are first input into NCLASS to determine the neoclassical particle diffusivity, D , and then, the particle convective velocity, v , is adjusted for both carbon and lithium to arrive at the best match between predicted carbon and lithium profiles (using the D and v combinations) and the time evolution of the experimental impurity profiles. Another approach is to use fully predictive MIST runs in which time-dependent neoclassical values for both D and v are determined from NCLASS, and are used as input for fully predictive MIST calculations to derive the full neoclassical prediction of the impurity charges states. Analysis has been carried out for both low and high collisionality discharges.

The results of hybrid and predictive MIST calculations for the high collisionality discharge are shown in Fig. TT-3 where the experimental carbon density profile at various times is compared to those calculated by the two methods. In the hybrid calculation (labeled “Interpretive (MIST)”), D is determined from neoclassical theory and the particle convection velocity v is determined from the best fit between the measured and calculated carbon density profiles. In the predictive calculation, both D and v are calculated from neoclassical theory. It is clear from Fig. TT-3 that there is much better agreement in the hybrid calculation, where the measured and calculated profiles (solid and dashed curves respectively in the right column of Fig. TT-3) show much better agreement than the profiles determined in the fully predictive calculation. The comparison in the predictive case shows that the early development of the carbon profiles is relatively in agreement with neoclassical predictions, but outboard peaking at later times is farther inward for the prediction than for the measurement (see lower right panel in Fig. TT-3). In addition, peaking is predicted in the very core of the plasma, especially at later times; this core peaking is not seen in the measured profiles. The results suggest that processes, such as turbulent transport, may be important; neoclassical transport alone cannot explain the carbon density profile evolution. A similar comparison was made for the low collisionality discharge and the results are similar to those shown in Fig. TT-3; neoclassical transport alone is insufficient to describe the transport necessary for agreement between measured and predicted carbon density profiles.

In summary, it is seen that collisionality has a strong influence on the electron and ion energy transport, with a strong decrease in electron transport, especially in the outer portion of the plasma, with decreasing collisionality. Ion transport with respect to neoclassical estimates actually increases going to lower collisionality, with neoclassical transport at the high collisionality but several times greater than neoclassical at the lowest collisionality. This trend may, in fact, also be due to decreasing rotation (and ExB) shear as collisionality is reduced,

instead of collisionality itself, and future experiments in NSTX-U will help resolve this uncertainty. Particle transport, as gauged from impurity transport, does not show the strong dependence on collisionality that is seen in the thermal ion species. Hybrid and predictive calculations indicate that neoclassical transport alone cannot account for the characteristic peaking near the edge of the plasma of the measured carbon density profile as the discharges evolve temporally; purely neoclassical transport would predict outer region peaking farther in than is measured, and an additional strong peaking in the very core. Consequently, some turbulent process may be important.

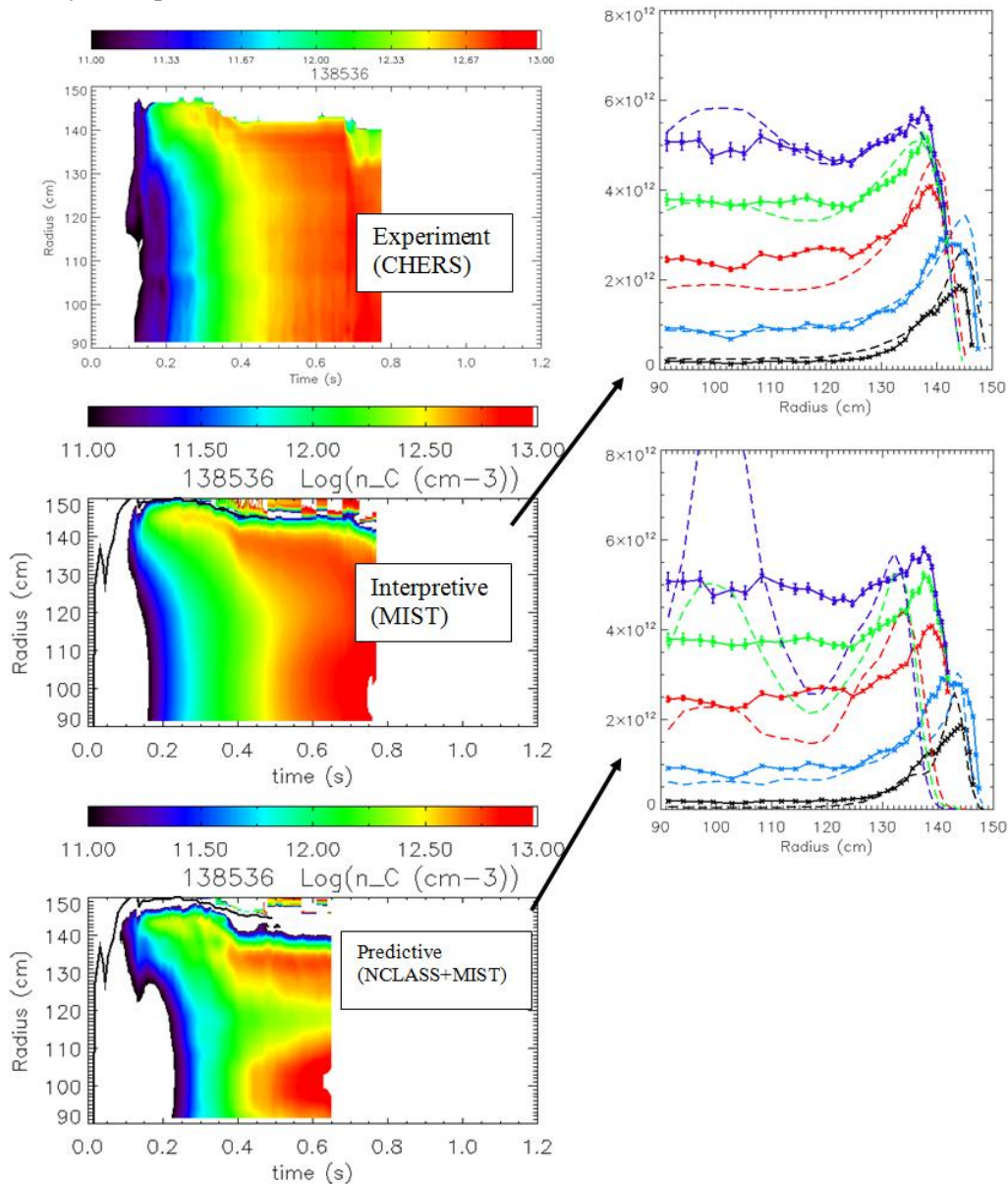


Figure TT-3: (Left column) Evolution of the carbon density profile vs time and radius for the experimental measurement (top panel), Hybrid MIST calculation (middle panel) and predictive MIST calculation (bottom panel) for the high collisionality discharge. The direct comparisons between the respective MIST calculations (dashed lines) and experimental profiles (solid curves) are shown at increasing times in the Right column. Curves are plotted for $t=0.2$ to 0.6 s in increments of 0.1 s.

L-Mode Transport Studies

a. Energy Transport: Effect of ExB Shear on High-k Fluctuations/Turbulence Characteristics

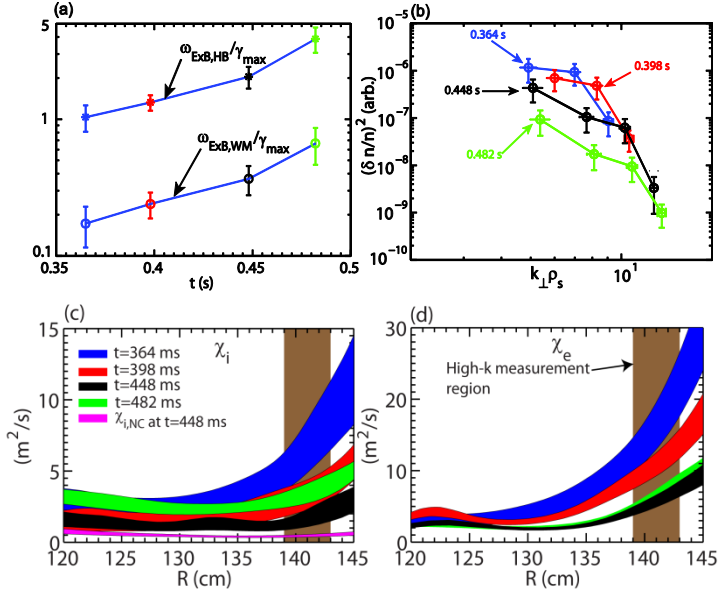


Figure TT-4: (a) The ratio between the ExB shear rate and the maximum linear growth rate for ITG instability (both the Hahn-Burrell ($\omega_{\text{ExB,HB}}$) and Waltz-Miller ($\omega_{\text{ExB,WM}}$) ExB shearing rates are shown); (b) k_{\perp} spectra in arbitrary unit at the 4 time points shown in (a); (c) and (d): The radial profiles of Ion (c) and electron (d) thermal diffusivity at $t=364$ ms (blue), 398 ms (red), 448 ms (black), 482 ms (green). The ion neo-classical thermal diffusivity, $\chi_{i,NC}$ (magenta) is also shown in (c). The vertical width of the colored bands denotes the experimental uncertainty mainly due to the uncertainty in ohmic heating and measured kinetic profiles (applicable to χ_i and χ_e). The rectangular shaded region denotes the high-k measurement region.

the outer half of the plasma ($r/a \gtrsim 0.5$). Turbulence spectrum was measured by a high-k scattering system [TT-6].

The change in ExB shearing rate and measured electron-scale wavenumber spectra are shown in Fig. TT-4 (a) and (b) at 4 time points of interest. The ion and electron thermal diffusivity profiles at the same times of interest are plotted in Fig. TT-4(c) and (d), respectively. (We note that the uncertainty in χ_i and χ_e in Fig. TT-4 is mainly due to uncertainties in ohmic heating and measured kinetic profiles). To model ExB shear effect on microturbulence, nonlinear gyrokinetic simulations are needed. However, here we use linear stability analysis to provide some initial assessment of the ExB shear effect in the experiment, motivated by the studies on ExB shearing rate and linear growth rate reported in Refs [TT-7,8]. In Fig. TT-4(a), $\omega_{\text{ExB}}/\gamma_{\text{max}}$ averaged in the high-k measurement region is plotted as a function of time (Note that both Hahn-Burrell shearing rate, $\omega_{\text{ExB,HB}}$, [TT-8] and Waltz-Miller shearing rate, $\omega_{\text{ExB,WM}}$, [TT-9] are used and

Recent analysis lead us to identify the first experimental observation of a progressive change in electron-scale turbulence k spectrum and thermal confinement at the core-edge transition region of a set of NSTX NBI-heated L-mode plasmas ($r/a \sim 0.66-0.78$), as the ExB shearing rate is continuously increased due to plasma toroidal velocity increase from Neutral Beam Injection (NBI). Observations on continuous ExB shear ramping-up were made in a set of center-stack limited and NBI-heated L-mode plasmas. These plasmas have a toroidal field of 5.5 kG, a plasma current of 900 kA and a two-phase NBI with the first 2 MW NBI pulse from about 100 ms to 200 ms and the second 2 MW NBI pulse from about 350 ms to the end of discharges. During the second phase of NBI, plasma continuously spins up, which leads to a simultaneous increase in the ExB shearing rate in

they differ by about a factor of 5), and γ_{max} is the maximum linear growth rate for the most unstable ion-scale instability (ITG modes) calculated with the GS2 code [TT-10]. We note that the gradual increase of $\omega_{ExB}/\gamma_{max}$ from t=364 to 448 ms is due to the increase of ω_{ExB} , while the faster increase of $\omega_{ExB}/\gamma_{max}$ after t= 448 ms is due to both the increase of ω_{ExB} and decrease of γ_{max} . Figure TT-4(b) shows the measured k_{\perp} spectra at time points used in Fig. TT-4(a). From t=364 to 398 ms, the measured maximum spectral power (at $k_{\perp}\rho_s \approx 5$) decreases by about 40% while $\omega_{ExB,WM}/\gamma_{max}$ increases from about 0.17 to 0.24. Meanwhile, the spectral power at larger wavenumbers ($k_{\perp}\rho_s \gtrsim 8$) has about a factor of 2 increase, and it appears that the slope of the spectra (at $k_{\perp}\rho_s \gtrsim 7$ for t=364 ms and at $k_{\perp}\rho_s \gtrsim 8$ for t=398 ms) is preserved. Larger decreases, about 60-80%, in spectral power at $k_{\perp}\rho_s \lesssim 10$ occur while $\omega_{ExB,WM}/\gamma_{max}$ approaches 0.4 at t=448 ms and 0.7 at t=482 ms. We note that from t=398 to 448 ms the k spectra seem to preserve the shape and power at $k_{\perp}\rho_s \gtrsim 10$, but at t=482 ms the spectral power at $k_{\perp}\rho_s \gtrsim 10$ also starts to drop. This overall decrease in spectral power with the large $\omega_{ExB,WM}/\gamma_{max}$ (~ 0.7) at t=482 ms is consistent with being close to the quenching threshold $\omega_{ExB,WM} \approx (1.1 - 1.2)\gamma_{max}$ calculated using the quenching rule in [TT-11] with $A \approx 1.9-2.1$ and $\kappa \approx 2$. Since the maximum ETG growth rate in the high-k measurement region, $\gamma_{max} \sim 10 - 20C_s/a$ (C_s is the sound speed and a is the plasma minor radius), is much larger than the experimental ExB shearing rate [$(0.1 - 0.4)C_s/a$], ETG turbulence is unlikely to be affected by the experimental amount of ExB shear. However, as we have shown in Fig. TT-4(b), electron-scale turbulence indeed decreases as ExB shearing rate is increased, and this motivate us to speculate that some of the observed electron-scale turbulence is nonlinearly driven by the ion-scale turbulence and its power decreases as the ion-scale turbulence is progressively suppressed by the ExB shear. However, in order to fully investigate this multi-scale interaction, multi-scale gyrokinetic simulations are required and are planned and will be carried out in future work.

From Fig. TT-4(c) and (d), we can immediately see that the largest decrease in both χ_i and χ_e occurs at $R \gtrsim 130$ cm ($r/a \gtrsim 0.5$), which coincides well with where the ExB shear varies most in the experiment. It is also clear that from t=364 to 398 ms, χ_i decreases by about 50% and χ_e decreases by about 35% in the high-k measurement region, and a decrease in χ_i and χ_e by about 50% occurs from t=398 to 448 ms, which correlates well with the changes in $\omega_{ExB,WM}/\gamma_{max}$ shown in Fig. TT-4(a), i.e. about 40% increase from t=364 to 398 ms and about 50% from t=398 to 448 ms. χ_i is always anomalous since at its smallest at t=448 ms, it only approaches to a factor of about 2-3 of the ion neo-classical thermal diffusivity, $\chi_{i,NC}$, which is consistent with the ion-scale turbulence not being completely quenched. We also point out that χ_i becomes larger and χ_e remains essentially the same from t=448 to 482 ms, even though $\omega_{ExB}/\gamma_{max}$ is almost doubled. We note that an n=1 MHD mode which starts to grow at about t=450 ms and saturates at t=470 ms may be responsible for this observation.

b. Particle Transport

A series of shots was analyzed to assess the thermal deuterium particle transport in the core of the plasma. The study was confined to the core since that is where the particle source, dominated by beam fueling, is known best. The particle source beyond $r/a \sim 0.6$ is dominated by gas fueling, and

the precise source rates, including recycling, in this region are not well known. The discharges chosen have $I_p=0.9$ MA, $B_T=0.55$ T, line-averaged density of $\sim 4 \times 10^{19} \text{ m}^{-3}$, and injected heating powers of 2 MW. The range of effective particle fluxes, and predicted levels of neoclassical particle transport for the thermal deuterium ions is shown in Fig. TT-5. The experimental range is indicated by the brown shaded region, which has been plotted only out to $r/a=0.8$ for the reasons given above. The range of predicted neoclassical fluxes is given by the blue shaded region. This comparison indicates that the particle flux ranges are comparable to what would be expected from neoclassical transport within $r/a \sim 0.6$. A greater difference between the two is seen for larger radii, but the experimental determination of particle transport is very uncertain due to not knowing the source of neutrals from gas puffing. Ion thermal diffusivities are approximately a factor of several greater than neoclassical, as is seen in Fig. TT-4(c).

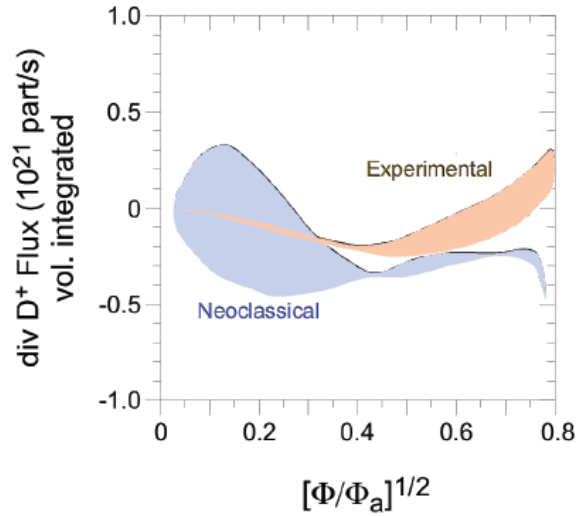


Figure TT-5: Inferred and neoclassical deuterium particle fluxes for L-mode scan

In summary, the energy transport in representative L-mode discharges is anomalous for both ions and electrons, with the ion energy transport becoming more anomalous as the plasma radius increases. The transport levels, however, decrease with increasing rotation (ExB) shear, and this is accompanied by a reduction in the mid-k range levels of microturbulence. It is believed that this mid-k range of turbulence is coupled to that at lower k. Particle transport of the main plasma species appears to be somewhat decoupled from the energy transport in that the particle transport appears to be consistent with neoclassical estimates in the core ($r/a < 0.5$) of the plasma. There is more of an anomalous behavior farther out.

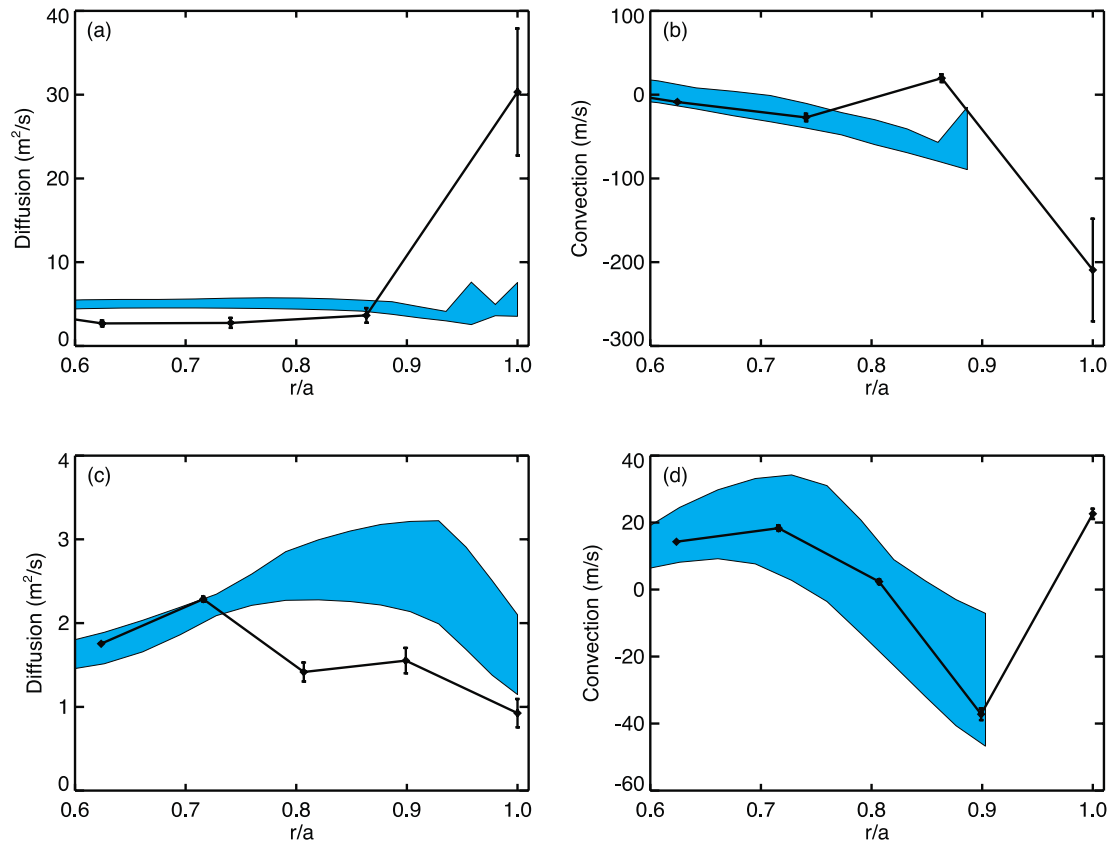
Particle transport in neon puff experiments

a. Edge Impurity Transport Measurements with a Multi-Energy SXR Diagnostic

Perturbative impurity transport measurements were performed in the NSTX plasma edge using short neon gas puffs and a multi-energy soft x-ray (ME-SXR) diagnostic which utilizes multiple filters to help distinguish low charge state emission from higher charge state emission, has been used to measure impurity transport in the ST plasma edge for the first time. Emission from low charge states, measured with thinner filters, provides the source terms for transport analyses of higher charge states.

To model the particle transport of an injected impurity, the STRAHL 1D impurity ion radial transport code [TT-12] is used. For a given impurity, the density evolution of each ionization state is described by a transport equation with a flux-surface averaged diffusion coefficient $D(r, t)$

and convective velocity $v(r, t)$ provided by the user. The particle source/sink term for each ionization state depends on n_e , T_e , and the density of neighboring states through the rate coefficients for ionization and the recombination coefficients for radiative and dielectronic recombination. Neutral deuterium density is not diagnosed in NSTX and is assumed to be negligible inside the separatrix, thus recombination coefficients due to charge exchange are not included in the model. The plasma parameters n_e and T_e are measured with Thomson scattering. Along with D and v , the third free parameter in this transport model is the source of neutral impurity atoms, both directly from the impurity injection and from divertor and vacuum vessel wall recycling. A simple synthetic diagnostic uses the densities of each charge state of an



impurity, calculated by STRAHL, to determine the filtered x-ray intensities that would be measured by the ME-SXR system.

Figure TT-6: (a) The resulting diffusion profile and (b) convection profile from the $I_p = 0.8$ MA, $B_T = 0.40$ T discharge. The shaded region represents the results from NCLASS neoclassical transport calculations. (c) Diffusion profile and (d) convection profile for the $I_p = 1.1$ MA, $B_T = 0.55$ T case. The radial knots are defined for fixed values of ρ_{pol} and thus shift radially between the two cases with different q profiles.

Perturbative impurity transport measurements were performed in NSTX using short 5 ms neon gas puffs at the outboard midplane, injecting about 2.5×10^{17} neon particles. Electrons from the neon puff accounted for only about 0.5% of the total plasma electron density, and Thomson scattering indicates that the perturbation to the bulk plasma was negligible. The impurity transport profiles calculated by STRAHL for an $I_p = 1.1$ MA and $B_T = 0.55$ T discharge, are shown in Figure TT-6. The error bars represent the uncertainty in the transport profiles due to uncertainty

in the ME-SXR and Thomson measurements and in the neoclassical values used to constrain core transport. For comparison, the results from the NCLASS neoclassical transport calculations are shown with shaded regions on the plots, covering the variation in the calculations during the time frame of the measurement. The results from the measurements roughly match neoclassical calculations, in agreement with previous results from the core [TT-13,14]. The diffusion coefficients obtained from measurements are within a factor of 2 of neoclassical transport across most of the plasma radius. Deviations from neoclassical diffusion in the edge region, particularly in the far edge of the low-field discharge, are likely due to edge turbulence and are the topic of ongoing studies. The convection profiles also roughly agree with neoclassical values, though NCLASS does not provide reliable convective velocities outside of $r/a \sim 0.9$. For the two cases shown, the neoclassical convective velocity remains outward far into the core, which is consistent with the hollow neon profile found in the STRAHL simulations at later times. Previous results from core measurements have shown that neon convection near mid-radius can be either inward or outward, depending on the ion temperature and density profiles, and that neon profiles can thus be either peaked or hollow [TT-13,14]. In conclusion, inside the pedestal region and under the conditions of these quiescent discharges, plasma turbulence is not sufficient to alter transport from neoclassical levels.

Electron Thermal Transport through Parametric Studies and Modeling

Following first nonlinear simulations of microtearing turbulence in NSTX [TT-15, 16], additional simulations (using the GYRO code) have been extended to test the influence of varying impurity (carbon) concentration and magnetic shear on resulting turbulence and transport. Simulations show that there is a dependence of transport somewhat consistent with linear analysis [TT-17], i.e. transport increasing with impurity concentration (n_c , or Z_{eff}) and magnetic shear. However, for some range of parameters the turbulence appears to transition (in time) from microtearing to instead a dominant electrostatic mode. For example, when artificially reducing the carbon density (n_c) from the experimental level to zero, the microtearing transport (EM component) is initially reduced as expected from a known reduction in linear growth rates. However, as the simulation progresses, the EM transport drops towards zero and instead an electrostatic-dominant turbulence emerges. Similar long-time behavior has been found for scans in magnetic shear, which may be indicative of a physically relevant transition in turbulence regimes as parameters are varied. Ongoing simulations are testing whether this behavior survives at increased resolution

a. ETG

The response of high- k turbulence to changes in local parameters has been studied using the coherent microwave scattering diagnostic [TT-6]. In one set of experiments the local core density gradient was increased by about a factor of 5 as a consequence of a large ELM [see the density gradient change in the high- k measurement region in Fig. TT-7(a) before and after the ELM]. Both the measured high- k turbulence spectral power and local electron heat flux was reduced with this increasing density gradient [see Fig. TT-7(b) and (c)], consistent with trends in linear ETG calculations [TT-18]. Nonlinear ETG simulations were able to predict transport approaching the experimental level for the low density gradient case, as well as the reduction in transport at increasing density gradient [see Fig. TT-7(c)] [TT-19]. Global, ion scale simulations

are being pursued to better understanding the discrepancy between experimental and simulated transport at the large density

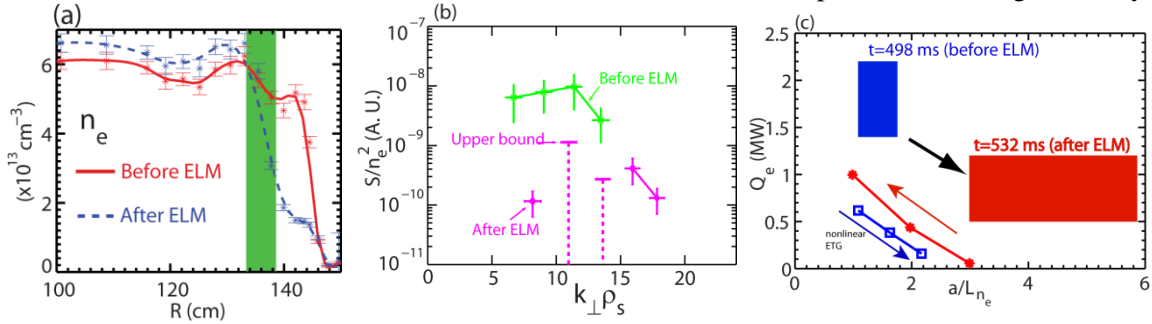


Figure TT-7: (a) Radial profiles of electron density before and after an ELM with the shaded region denoting the high- k measurement region; (b) The k_{\perp} spectra in arbitrary unit (normalized to n_e^2 and S is the spectral density calculated using the total scattered power in the spectra of each channel) before and after the ELM. The absolute upper bounds for the density fluctuation spectral power are denoted by horizontal solid lines on the tops of vertical dashed lines; (c) Electron heat flux from experiment (solid rectangles) and nonlinear ETG simulations (lines) at different observed density gradients before and after the ELM.

gradient.

Additional experiments were carried out to vary electron collisionality (ν_e^*) by more than a factor of two with other normalized parameters kept relatively constant. It is found that the measured high- k spectral power appears to increase with a reduction in collisionality [see Fig. TT-8(a)], even though the normalized confinement time increased with $\Omega\tau^E \sim \nu_e^{*-0.8}$ [TT-19]. (The difference in spectral power in lower wavenumber between the two low collisionality shots could be due to a difference in the ExB shearing rate [TT-19]). This anti-correlated dependence of the high- k turbulence with confinement is counterintuitive to expectations. Linear and nonlinear simulations illustrate the ETG instability is independent of collisionality for these parameters, but is sensitive to the small variations in other local parameters such as density gradient [see Fig. TT-8(b) for nonlinearly predicted electron heat flux as a function of density gradient] and magnetic shear. Furthermore, large profile variations in equilibrium quantities, e.g. ExB shear, actually may make the contribution from ion-scale turbulence possible, and global ion scale gyrokinetic simulations are needed to address this issue.

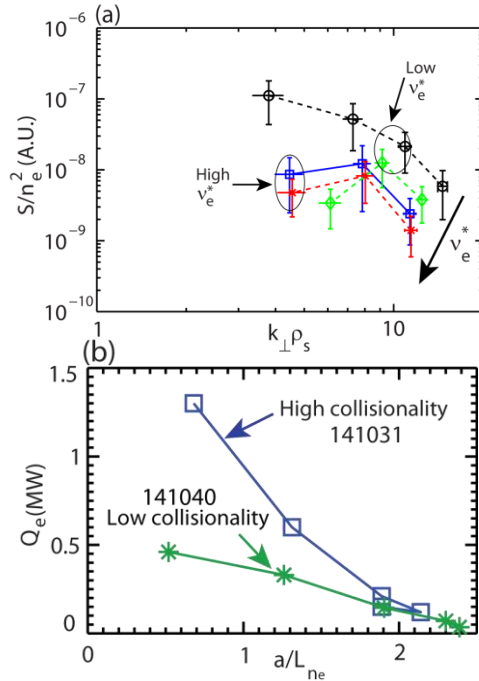


Figure TT-8: (a) The spectra in arbitrary unit (normalized to n_e^2 and S is the k_{\perp} spectral density calculated using the total scattered power in the spectra of each channel) for shots 141031 (blue square), 141032 (red asterisks), 141007 (black circle), and 141040 (green diamond). The direction of increase of collisionality is denoted by a black arrow; (b) predicted Q_e as a function of density gradient for shot 141040 (green asterisk) and shot 141031 (open square).

Electron internal transport barriers (e-ITBs) have been previously been reported to occur with strong negative magnetic shear ($s < -0.5$). For a large collection of discharges, both the large local electron temperature gradients (much larger than the linear ETG threshold) and the small

measured turbulence intensity from “high-k” scattering are strongly correlated with the largest magnitudes of negative magnetic shear. Recent non-local GYRO simulations have now verified that the ETG turbulence and transport is suppressed with strong negative magnetic shear in the region of the e-ITB, as shown in Fig. TT-9 (top, middle) [TT-20]. In the outer regions of the e-ITB the predicted ETG flux reaches experimental levels but turbulence cannot propagate past the barrier. Additional local simulations verify that this suppression results predominantly from a nonlinear stabilizing effect that occurs in the absence of strong $E \times B$ shear, confirming that negative magnetic shear alone is sufficient for ETG suppression. This nonlinear effect is very strong, with the threshold for significant transport approaching three times the linear critical gradient in some cases (Fig. TT-9, bottom).

b. KBM/TEM

As part of the FY12 JRT, linear stability calculations have been run for dozens of NSTX NBI heated H-modes (e.g. [TT-2]). In the locations of $r/a=0.6-0.8$ there are often multiple independent modes unstable simultaneously, an example of which is shown in Fig. TT-10 (top), where a microtearing instability is subdominant to a ballooning instability. (The symbols and dashed lines correspond to solutions from different numerical solvers or geometry assumptions.) Subsidiary scans for the $k_{\theta}\rho_s=0.37$ ballooning mode (Fig. TT-10, middle) illustrate the mode exhibits characteristics very similar to a TEM: driven unstable by electron density and temperature gradients (a/L_n , a/L_{Te}), weakly dependent on ion temperature gradient (a/L_{Ti}), and strongly stabilized by increasing collisionality (ν_{ei}). However, unlike a traditional electrostatic TEM instability, this mode is extremely sensitive to β_e with the appearance of an effective threshold ($\beta_{e,crit} \sim 0.8\%$) similar to that expected for a KBM instability. The fact that the scaling of the growth rates are unified by the MHD alpha parameter (Fig. TT-10, bottom), $\alpha_{MHD} = -q^2 R \nabla \beta$ [where $\beta = \Sigma(n_s T_s) \cdot 2\mu_0 / B^2$], highlights the KBM nature of the instability, so we refer to it as a “hybrid” KBM/TEM. Similar KBM behavior has been predicted in GS2 simulations near the top, and inside of, the pedestal region [21].

First nonlinear simulations based on this case [22] (not including flow shear) show a number of interesting features (Fig. TT-11). First, the predicted heat fluxes are experimentally significant ($\sim 2-4$ MW) although the transport is very bursty. Second, there is a significant contribution to heat and particle fluxes from the compressional magnetic perturbations ($B_{||}$). One can also see around $t=100-150 a/c_s$ there is a burst in electron thermal transport from the $A_{||}$ perturbations, which eventually subsides. This is likely a consequence of the subdominant microtearing instability at higher $k_{\theta}\rho_s$ that is ultimately unable to compete with the strong KBM/TEM turbulence, although we have not run a proper convergence in radial resolution to verify the microtearing physics is sufficiently represented. The time-averaged transport fluxes peak around $k_{\theta}\rho_s \sim 0.4$ (not shown), and total predicted transport is reduced with a reduction in beta, as would be expected from the linear scalings in Fig. TT-10 (middle).

It is also interesting to note that the KBM/TEM turbulence can predict significant momentum transport, although in this particular case the turbulence is strongly reduced with the inclusion of finite $E \times B$ shear. Nevertheless, the KBM/TEM turbulence provides one possible mechanism that

could account for both anomalous electron and momentum transport, with near neoclassical ion thermal transport. Additional simulations are underway to test the sensitivity of these predictions, and at other locations where the $E \times B$ shear suppression is not as strong.

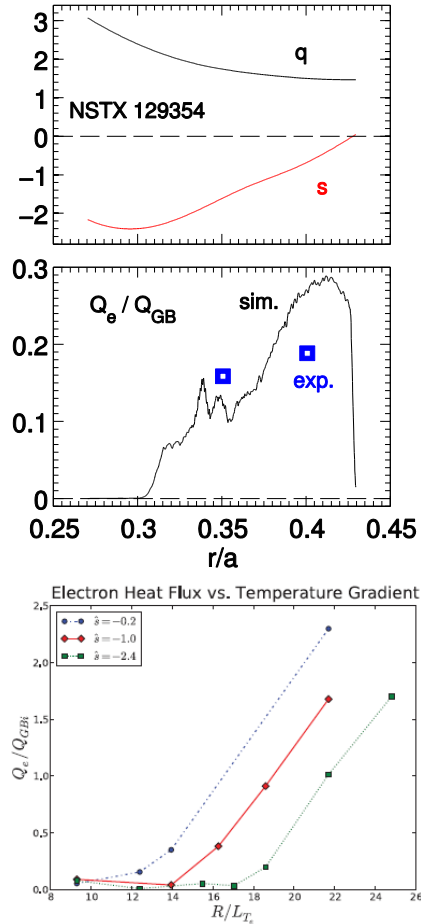


Figure TT-9: (top) Safety factor (q) and magnetic shear (s) profiles for e-ITB discharge. (middle) Predicted normalized electron heat flux in a global simulation. (Bottom) Predicted heat flux vs. temperature gradient for various values of negative magnetic shear.

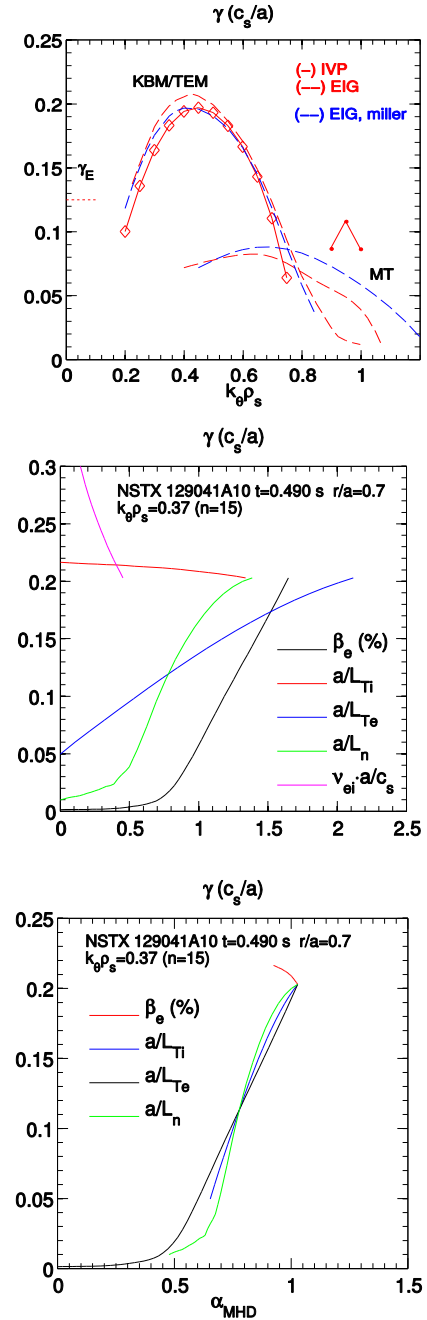


Figure TT-10: (top) Linear spectra of overlapping MT and KBM/TEM instabilities. (middle) Scaling of ballooning mode growth rate with β_e , a/L_{Ti} , a/L_{Te} , a/L_n , v_{ei} . (Bottom) Ballooning growth rates vs. α_{MHD} .

Development of the in-vessel Multi-Energy Soft X-ray (ME-SXR) diagnostic

The first generation ME-SXR diagnostic was designed, built, and implemented on NSTX by the Johns Hopkins University (JHU) group for the late 2010 and 2011 experimental campaigns [TT-23]. While total run time was limited by the early transition into the NSTX upgrade phase, the acquired data measuring ‘edge’ impurity transport provided a strong contribution to the 2012 JRT milestone as shown in the previous section [TT-24]. The goal of the in-vessel ME-SXR is to



Figure TT-11: In-vessel, atmospheric re-entrant ME-SXR for NSTX-U showing cable access port, PCB electronics inside housing, vacuum diode arrays, and pinhole assembly

maintain and expand the capability to measure filtered SXR emission to provide high time (>10kHz) and spatial resolution (~1-3cm) electron temperature, density, and impurity profiles from the edge to the plasma core. The addition of another neutral beam, along with a reshuffling of port diagnostic allocation, necessitated a new ME-SXR diagnostic design with the capability for in-vessel operation using a re-entrant, atmospheric housing for the ME-SXR electronics (Fig TT-11). The severe space constraints involved in placing a diagnostic between the vacuum vessel wall and the plasma edge make the engineering and design quite challenging; however, a preliminary design has been completed that provides adequate interior room for the amplifier electronics and cabling. The electronics will be similar to the first generation ME-SXR with ongoing development to test on-board A/D and serial conversion to significantly reduce the in-vessel cabling requirements for the system. Furthermore, the JHU group is developing advanced algorithms using neural network programming to incorporate ME-SXR data along with other plasma constraints to provide robust and fast electron temperature and density profile reconstructions with the potential for real-time feedback information.

ME-SXR collaboration with EAST

The capability of the ME-SXR system to provide high time and spatial resolution profiles generated interest from the EAST fusion research program. The JHU group was subsequently contacted by Dr. Gousheng Xu, leader of the edge physics group, to investigate possible collaborative opportunities to provide similar data for the EAST facility. With support from DoE, Dr. Kevin Tritz from the JHU group is working with EAST to design, build, and implement on EAST a high spatial resolution (<1cm) ME-SXR diagnostic to measure profiles in the plasma edge. Because the EAST ports have a long throat due to the existence of a cryostat necessary for the superconducting coils, this system must also be based on a re-entrant, atmospheric assembly to provide the required field of view of the plasma edge. The EAST ME-SXR design is complete, and more closely based on the physical assembly of the NSTX 1st generation system (Fig TT-12).

Present plans are to complete the construction by summer 2013 for delivery to EAST for testing and integration into the data acquisition system, with installation into the vessel scheduled for later that same year. This system will be used to study edge profile dynamics during ELMs, provide estimates of electron temperature profiles, and can also be used to study perturbative transport, ideally using the EAST molecular cluster injector. An expansion of the edge ME-SXR diagnostic on EAST to a full edge/core

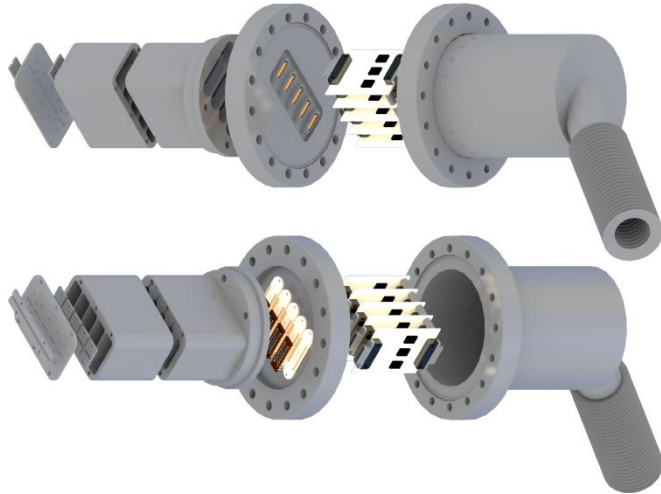


Figure TT-12: EAST ME-SXR in-vessel, re-entrant design for high spatial resolution (< 1cm) measurements of the plasma edge

system at multiple toroidal locations is planned for the future pending funding from a grant submitted to the ‘Collaborative Research in Magnetic Fusion Energy Sciences on International Research Facilities’ solicitation.

References

- [TT-1] S.P. Gerhardt, et al., Nucl. Fusion 51, 073031 (2011)
- [TT-2] S.M. Kaye, et al., IAEA FEC EX/7-1 (2012)
- [TT-3] M.G. Bell, et al., Plasma Phys. Controlled Fusion 51, 124054 (2009)
- [TT-4] R. Hulse, Nucl. Technol. Fusion 3 (259), (1983)
- [TT-5] W.A. Houlberg et al., Phys. Plasmas 4 (9), (1997)
- [TT-6] D.R. Smith, E. Mazzucato, W. Lee, et al., Jr., Rev.Sci. Instrum. 79, 123501 (2008)
- [TT-7] K.H. Burrell, et al., Phys. Plasmas 4, 1499 (1997)
- [TT-8] T. S. Hahm and K. H. Burrell, Phys. Plasmas 2, 1648 (1995)
- [TT-9] R.E. Waltz and R.L. Miller, Phys. Plasmas 6, 4265 (1999).
- [TT-10] M. Kotschenreuther et al., Comp. Phys. Comm. 88, 128 (1995)
- [TT-11] J. E. Kinsey, R. E. Waltz, and J. Candy, Phys. Plasmas 14, 102306 (2007)
- [TT-12] K. Behringer, Description of impurity code ‘STRAHL’, Technical Report JET-IR(87)08, JET Joint Undertaking, Oxfordshire: Abingdon (1987)
- [TT-13] L. Delgado-Aparicio, et al., Nucl. Fusion 49, 085028 (2009)
- [TT-14] L. Delgado-Aparicio, et al., Nucl. Fusion 51, 083047 (2011)
- [TT-15] W. Guttenfelder et al., Phys. Rev. Lett 106, 155004 (2011)
- [TT-16] W. Guttenfelder et al., Phys. Plasmas 19, 056119 (2012)
- [TT-17] W. Guttenfelder et al., Phys. Plasmas 19, 022506 (2012)
- [TT-18] Y. Ren et al., Phys. Rev. Lett (2011)
- [TT-19] Y. Ren et al., Phys. Plasmas 19, 056125 (2012)
- [TT-20] J.L. Peterson et al., Phys. Plasmas 19, 056120 (2012)
- [TT-21] J. Canik et al., IAEA FEC EX/P7-16 (2012)
- [TT-22] W. Guttenfelder et al., IAEA FEC TH/6-1 (2012)
- [TT-23] K. Tritz, et. al, Rev. Sci. Instrum. 83, 10E109 (2012)
- [TT-24] D. J. Clayton, et. al, “Multi-energy SXR technique for impurity transport measurements in the fusion plasma edge,” Plasma Phys. Control. Fusion, in press.

Energetic Particle Research

Energetic Particle Research in FY-2012 has been driven by two fundamental themes in the study of fast ion driven instabilities, which include Alfvénic modes (AEs), Energetic Particle modes (EPMs) and lower frequency MHD modes such as kinks and fishbones. The first theme is the dependence of the instabilities' behavior on modifications of the fast ion distribution function, F_{nb} , in energy and pitch (*phase space*), in addition to more obvious parameters such as the fast ion pressure or the radial fast ion density gradient. The second theme is the importance of non-linear effects in regulating stability and saturation mechanisms of AEs, as well as the multi-mode dynamics involving disparate classes of AEs.

Previous studies of the effects of Toroidal Alfvén eigenmodes (TAEs) on fast ion transport in NSTX have been extended to a broader set of conditions [EP-1], including H-mode plasmas [EP-2]. A statistical correlation between the bursting/chirping nature of the modes and some discharge parameters (e.g. ratio of fast ion to thermal plasma pressure) has been established. However, the available database should be further extended to reach more conclusive and quantitative results on the relationship between plasma parameters (such as q-profile, NB injection geometry), mode stability and specific regime of the instabilities [EP-1].

The effects of TAEs on the fast ion distribution have been investigated through numerical simulations based on the NOVA-K [EP-3] and ORBIT [EP-4] codes. Simulations indicate that TAE effects on fast ions are more complicated than a simple enhancement of radial diffusion. In the presence of multiple modes characterized by different helicity, fast ions are redistributed in energy as well as space [EP-2]. This is important, for example, to understand (and develop tools to predict) the effects of instabilities on NB-driven current. In the analysis, ideal eigenmodes obtained via NOVA-K are selected and re-scaled based on measurements of the radial mode structure from a multi-channel reflectometer array [EP-5]. The selected modes are then used in the gyro-center orbit following code ORBIT to simulate the fast ion response to the modes [EP-6]. Most analyses have been performed for so-called TAE *avalanches*, because of the large enhancement of fast ion transport and NB-driven current redistribution they can induce. ORBIT simulations for H-mode scenarios have shown the complex modifications of fast ion phase space caused by avalanche events [EP-2]. An important conclusion is that a depletion of the higher energy portion of F_{nb} can occur even without a noticeable loss of fast ions from the core plasma. From the experimental point of view, this indicates that the simple deduction of fast ion redistribution or loss from quantities like the neutron rate, that are sensitive to F_{nb} changes over limited regions of phase space, may be misleading.

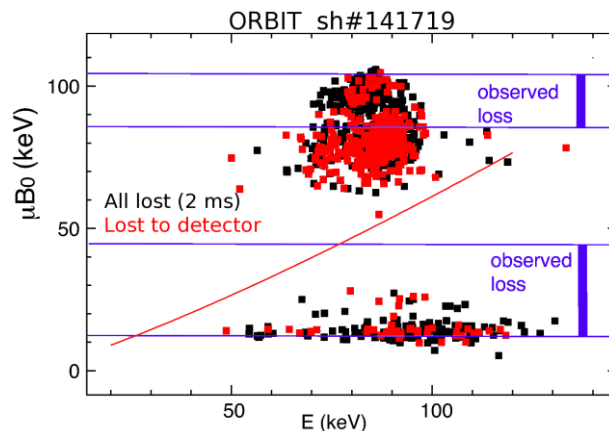


Figure EP-1: ORBIT simulations of lost beam ions in the $(E, \mu B_0)$ plane after 2 ms of motion through a TAE avalanche field perturbations. Black points are all guiding centers that reach the last closed surface. Red points are lost particles reaching the synthetic sFLIP detector. Losses seen by the detector are representative of the groups of lost particles. Marked blue are the extents of the two loss spots seen on the detector in the experiment.

Fast ion transport associated with TAE avalanches has been further investigated by comparing the measured and simulated response of a scintillator-based Fast Lost Ion Probe (sFLIP [EP-7]) during avalanches. Two discharges with similar avalanching TAEs and neutron rate drops but different observations from sFLIP are compared. For the first discharge, sFLIP does detect lost fast ions at the plasma edge. The measured energy spectrum and pitch range of the lost particles is in fair agreement with ORBIT predictions (Fig. EP-1), indicating that the model is capturing the essential features of fast ion transport from the core to the plasma edge up to the vessel wall, where sFLIP is located. In a second discharge, in spite of the similar level of TAE activity and neutron rate drop, no substantial loss is detected by sFLIP, which is consistent with the outcome of NOVA-K and ORBIT simulations [EP-8].

As pointed out previously, results from NOVA-K and ORBIT modeling confirm the importance of a detailed knowledge of F_{nb} modifications over extended regions of phase space to overcome simplistic conclusions on fast ion transport and redistribution and to provide more stringent constraints for code validation/verification, thus enabling accurate theory-experiment comparisons. The physical models of mode growth and saturation are being challenged to explain the avalanching behavior commonly observed for TAEs in NSTX plasmas with fast ion pressure greater than $\approx 30\%$ of the thermal pressure. To this purpose, codes that are capable of capturing the full non-linear dynamics of wave-particle interaction are being upgraded and applied to NSTX scenarios. For example, the self-consistent, non-linear code M3D-K [EP-9] is being

upgraded to use numerical fast ion distribution functions from the NUBEAM module within the TRANSP code. This is necessary for accurately modeling the details of a realistic beam ion distribution, which cannot be adequately captured by commonly used analytic distribution functions. In addition to M3D-K, simulations of NSTX plasmas with the gyro-kinetic code GTC [EP-11] have begun to verify whether the observed bursting/chirping TAE regime can be explained by the rapid formation and destruction of phase space structures, even in the absence of fast ion sources and sinks [EP-12]. Based on the improved understanding of TAE effects on fast ion transport, a project has started in FY-2012 to incorporate the physics of fast ion distribution modifications by resonant TAEs into the TRANSP code for improved simulations of heating and current drive by neutral beam injection.

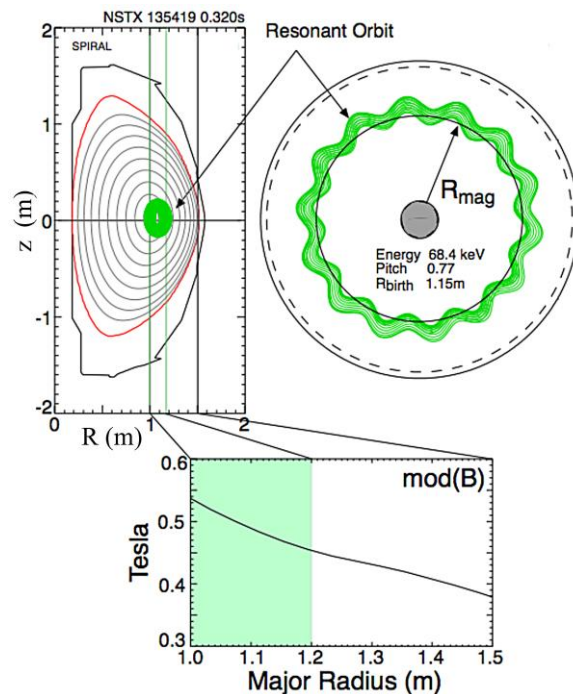


Figure EP-2: Orbit of a representative fast ion resonant with a GAE mode, (a) mapped on a poloidal cross-section of NSTX, (b) plan view on the equatorial plane and (c) $\text{mod}(B)$ on mid-plane. The shaded region shows the range spanned by the guiding centre.

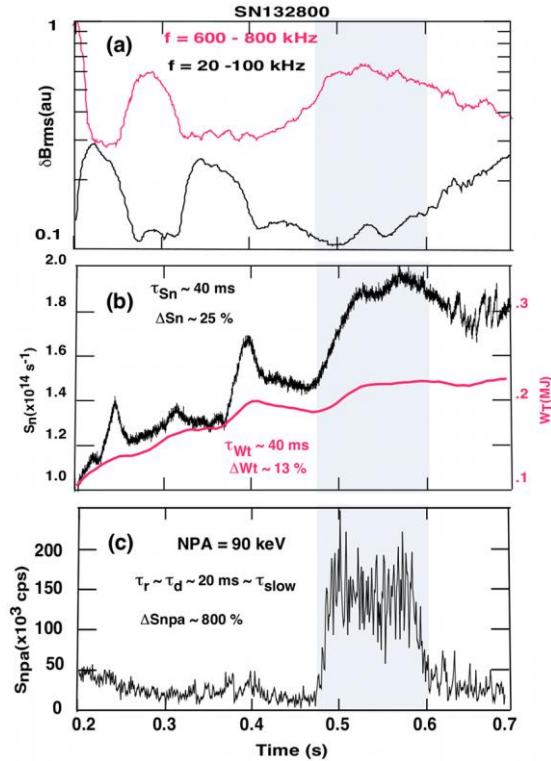


Figure EP-3: Example of enhanced NPA flux at the full NB energy $E=90$ keV (c) observed during a period (blue bar) of reduced low frequency and robust high frequency MHD activity (a) that is attended by increases in the neutron yield and stored energy (b).

to quantify the effect that GAE and CAE modes have on the fast ion distribution. Similarly to TAE modes, phase space modifications by GAE/CAEs are believed to be crucial to explain features such as an enhanced flux corresponding to full energy NB ions observed on the NPA diagnostic (Fig. EP-3). Redistribution of fast ions toward larger pitch (higher parallel velocity) by GAE/CAE modes is a candidate mechanism to explain this phenomenon [EP-16]. If confirmed, the same mechanism could be important to understand how (and if) conveniently stabilized/destabilized high-frequency AEs can be used to redistribute particles in phase space, for example to push trapped fast ions toward passing (better confined) orbits that are more favorable for NB current drive or to broaden the fast ion pressure profile.

In addition to TAE modes, a broad spectrum of Global and Compressional Alfvén eigenmodes (GAE/CAE) is commonly observed on NSTX at frequencies comparable to the ion-cyclotron frequency. An improved characterization of radial structure and temporal evolution of the modes has been achieved through analysis of data from reflectometers and Mirnov coils [EP-5]. A method to distinguish between GAE and CAE modes, based on a combination of toroidal mode number analysis and comparison of the mode frequency evolution with a local dispersion relation, has been developed [EP-13]. Progress has also been made in simulating and understanding the complicated Doppler-shifted cyclotron resonance drive for counter-propagating CAE and GAE modes, see Fig. EP-2. The full-orbit, particle-following code SPIRAL [EP-14] has been used to model fast ion orbits and verify the resonance conditions.

It seems likely that the relatively low ratio of the cyclotron frequency to the transit frequency in NSTX facilitates this type of resonance drive. More detailed simulations with the combined SPIRAL and HYM [EP-15] codes are planned

Fast ion phase space modifications are also believed to be responsible for a number of observations involving different classes of MHD modes. A first example is provided by the destabilization of high-frequency AEs that follows the appearance of low-frequency kink-like modes [EP-17], as shown in Fig. EP-4(a-b). Recent M3D-K simulations suggest that these long-lived kink modes are a saturated, non-resonant (1,1) kink mode. These modes can in turn flatten the radial beam ion profile and lead to significant broadening of beam-driven current [EP-18]. SPIRAL simulations have been performed with a kink radial structure obtained through the PEST code and validated by soft X-rays data. The simulation indicates that fast ions are scattered to larger pitch, cf. Fig. EP-4(c), into phase space regions where CAE resonances are expected. The depletion of the smaller pitch portion of F_{nb} is also consistent with a drop in signal observed on a Fast Ion D-Alpha profile diagnostic, that is mostly sensitive to pitch values around or below ~ 0.5 .

The application of $n=3$ external field pulses also alters the stability and behavior of high frequency instabilities. In the example shown in Fig. EP-5, beam ions drive persistent bursting/chirping modes between 400-700 kHz. The modes are probably Global Alfvén eigenmodes (GAE) with toroidal mode number $n=7-9$. When the $n=3$ pulse is applied, the GAE burst frequency triples, the mode amplitude halves, and the extent of the frequency sweep decreases from 100 kHz to 40 kHz. There is a delay between these changes and the application of the field perturbation, suggesting that a modification of the fast ion distribution function is responsible. In this case, analysis with the SPIRAL code indicates that the external field perturbation depletes the portion of phase space that

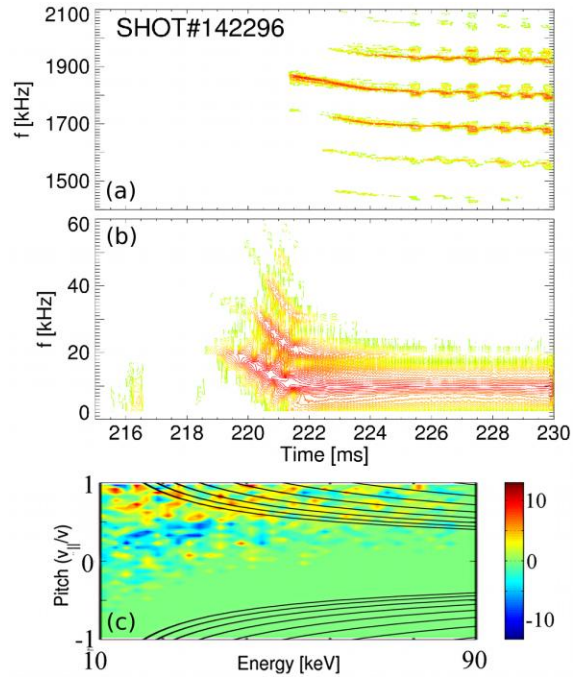


Figure EP-4: (a-b) Destabilization of CAE modes soon after low-frequency kink-like modes are destabilized. (c) SPIRAL simulation of fast ion redistribution, showing an increase in F_{nb} in regions where CAE resonances are expected.

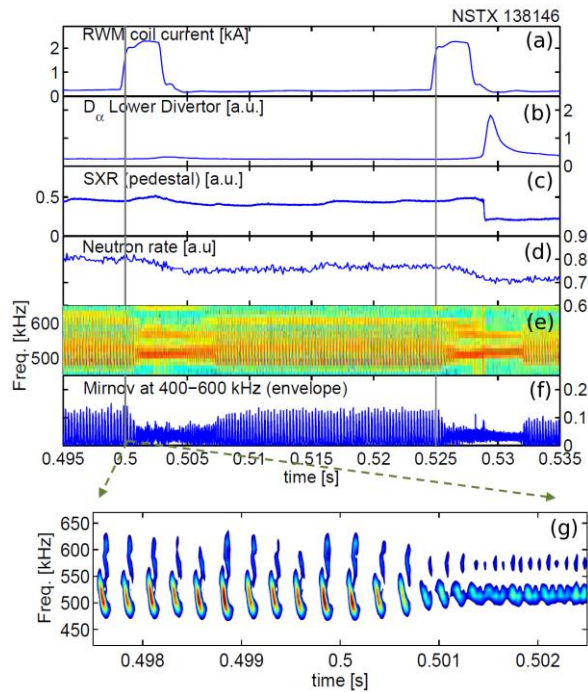


Figure EP-5: Modification of GAE activity during RMP pulses with $n=3$. (a-b) Time traces of RWM coil current I_a and SXR emission. (d) Measured neutron rate. (e-f) Frequency spectrum and rms signal amplitude of magnetic fluctuations from Mirnov coils. (g) Detail of mode evolution around $t \sim 0.5$ s.

drives the GAE instabilities. This interesting observation contributes to an overarching goal of EP research: Develop tools that can control fast-particle driven instabilities.

Possible coupling between different MHD and fast ion driven instabilities can further complicate the non-linear mode dynamics and their effect on the fast ion population on NSTX. For instance, otherwise (linearly) stable modes can be destabilized through non-linear coupling. The non-linear saturation level of Alfvénic instabilities can be significantly affected by non-linear coupling. Experiments on NSTX have evidenced non-linear, three-wave coupling between pairs of TAE modes and a $n=1$ kink. This appears to be a direct mode-mode coupling between TAEs and the kink mode. Coupling of Global Alfvén Eigenmodes to TAE modes through the fast ion distribution is also observed, with GAE avalanches triggering TAE avalanches. Likewise, low-frequency MHD activity (kinks or tearing modes) is suspected of redistributing fast ions and destabilizing high frequency CAE modes, as discussed before. In general, the broad spectrum of Alfvénic activity on NSTX potentially interacts both directly, through wave-wave coupling, as well as indirectly, through modifications of the fast ion distribution. In turn, the latter affects stability and saturation of energetic particle driven modes. Further improvements in theoretical models, numerical codes and diagnostics are required to untangle this complex web of interactions.

References

- [EP-1] M. Podestà et al, Nucl. Fusion 52, 094001 (2012)
- [EP-2] E. D. Fredrickson et al, "Fast ion energy loss during TAE avalanches in the National Spherical Torus Experiment", Nucl. Fusion (2012), submitted.
- [EP-3] C. Z. Cheng, Phys. Rep. 1, 211 (1992)
- [EP-4] R. B. White et al, Phys. Fluids 27, 2455 (1984)
- [EP-5] N. A. Crocker et al, Plasma Phys. Control. Fusion 53, 105001 (2011)
- [EP-6] E. D. Fredrickson et al, Phys. Plasmas 16, 122505 (2009)
- [EP-7] D. S. Darrow, Rev. Sci. Instrum. 79, 023502 (2008)
- [EP-8] D. S. Darrow, "Stochastic orbit loss of neutral beam ions from NSTX due to Toroidal Alfvén eigenmode avalanches", Nucl. Fusion (2012), submitted
- [EP-9] W. Park et al, Phys. Plasmas 6, 1796 (1999)
- [EP-10] G.-Y. Fu et al, "M3D-K simulations of beam-driven Alfvén modes in NSTX", Joint EU-US Transport Task Force Meeting, San Diego CA (2011)
- [EP-11] Z. Lin et al, Science 281, 1835 (1998)
- [EP-12] H. S. Zhang et al, Phys. Rev. Lett. 109, 025001 (2012)
- [EP-13] N. A. Crocker et al, Proceedings of the 24th Int. Conf. San Diego CA, 2012, paper IAEA EX/P6-02 (International Atomic Energy Agency, Vienna, 2012).
- [EP-14] G. J. Kramer et al, "Description of the full particle orbit following SPIRAL code for simulating fast-ion experiments in tokamaks", PPPL report no. 4788 (2012); Plasma Phys. Control. Fusion (submitted, 2012)
- [EP-15] E. V. Belova et al, Proceedings of the 24th Int. Conf. San Diego CA, 2012, paper IAEA 302-TH/P6-16 (International Atomic Energy Agency, Vienna, 2012).
- [EP-16] S. S. Medley et al, Nucl. Fusion 52, 013014 (2012)
- [EP-17] A. Bortolon et al, "Fast ion losses and redistribution induced by low frequency MHD in NSTX plasmas, based on FIDA observations and full-orbit simulations", 12th IAEA Technical Meeting on Energetic Particles in Magnetic Confinement Systems, Austin TX (September 2011)
- [EP-18] F. Wang et al, International Sherwood Fusion Theory Conference, Atlanta GA (March 31-April 3, 2012)

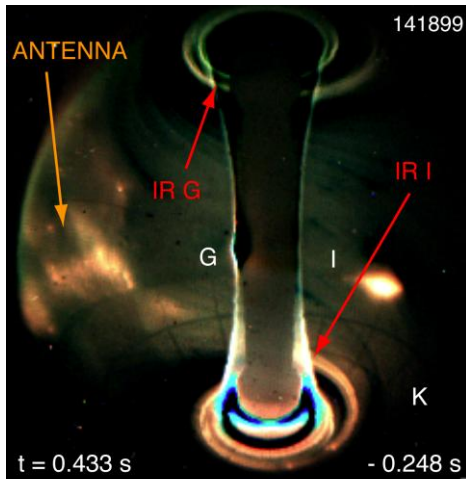
Wave Heating and Current Drive

HHFW SOL/Divertor Interactions in NSTX

Ion-cyclotron range of frequency (ICRF) heating and current drive can provide an important tool that supports the development of burning plasma science. Twenty megawatts of ICRF heating are currently planned for ITER. Furthermore, FNSF designs based on the spherical torus (ST) do not

have a central solenoid to drive the plasma current so the plasma must be initiated, ramped-up and sustained fully non-inductively.

High-harmonic fast wave (HHFW) power can, in principle, effectively ramp-up the plasma current through bulk plasma heating and bootstrap current enhancement in an FNSF ST device, even at low plasma currents where neutral beam current drive is ineffective due to poor fast-ion confinement. HHFW power is also a good candidate for on-axis non-inductive current generation in future fusion reactors. HHFW heating and current-drive efficiencies on NSTX can be significantly lowered by interactions of the HHFW with the edge plasma in the scrape-off layer (SOL) [RF-1-5]. In such cases, the heating efficiency has been shown to be related to the location of the onset density for perpendicular fast wave propagation, and it is



B

Figure RF-1: Camera view of “hot” RF produced spiral for shot 141899 with a edge magnetic pitch of $\sim 40^\circ$. Conditions are D_2 , $B_T = 4.5$ kG, $I_p = 1$ MA, $P_{RF} = 1.4$ MW, Antenna $k_\phi = -8$ m^{-1} , $P_{NB} = 2$ MW, H-mode with $n_e(0) \sim 5 \times 10^{19}$ m^{-3} , antenna-LCFS gap ~ 6.7 cm. Locations for antenna, ports B, G, I, K, and IR camera views are noted.

hypothesized that surface waves are being excited just beyond this onset density [RF-1, 2]. These edge interactions result in RF power deposition from the antenna to both the lower and upper divertor regions where bright spirals are produced, as shown in Fig. RF-1. The location of the spirals in the divertor regions is consistent with the hypothesis that HHFW power flows through the SOL to the divertor regions along magnetic field lines that pass in front of the antenna [RF-6]. This includes the field lines across the SOL between the antenna and the last closed flux surface (LCFS) as indicated in Fig. RF-2, that shows that the HHFW power flow to the divertor regions occurs across the width of

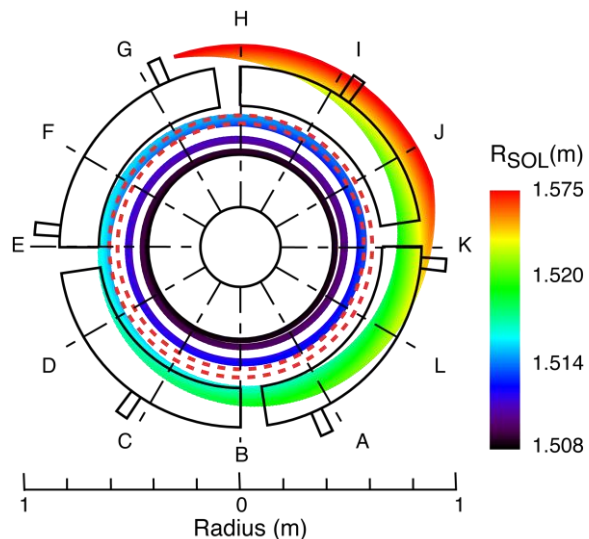


Figure RF-2: Magnetic field line strike points on lower divertor region for field lines originating between the antenna and the LCFS in the SOL at the midplane of the antenna for shot 141899 at $t = 0.435$ sec. (LRDFIT04 and conditions for Fig. RF-1.)

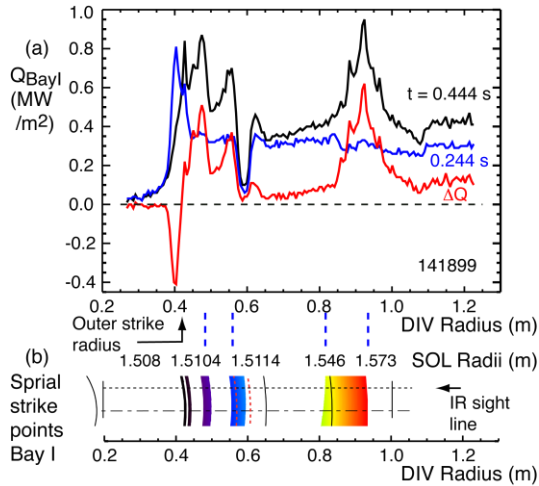


Figure RF-3: (a) IR heat flux to bottom divertor region at Bay I along sight line shown in (b). (b) Spiral strike points at Bay I. CHI gap is indicated with dashed red lines. (Conditions of Fig. RF-1.)

optimizing HHFW performance and fast wave performance in general, especially for high-power long-pulse ICRF heating in ITER.

Interaction of HHFW RF Power and NBI Fast-Ions

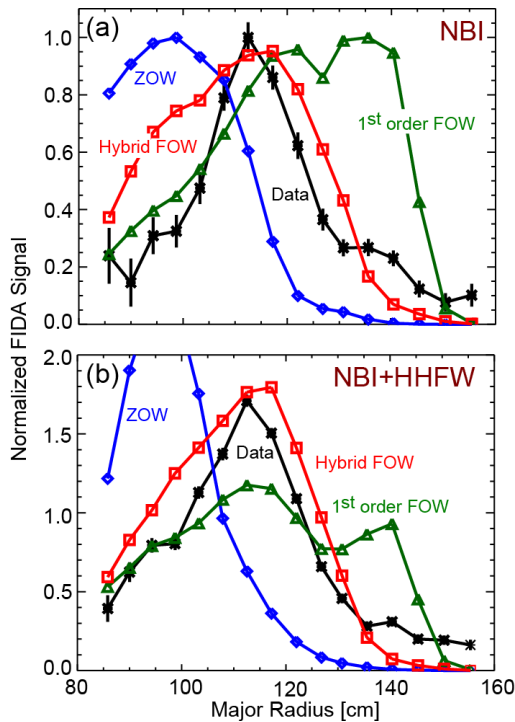


Figure RF-4: Comparison of FIDA fast ion profile data (black) with CQL3D simulation results: ZOW (blue), 1st order FOW (green) and Hybrid FOW (red). (a) for a discharge with NBI (shot 129842) and (b) for a discharge with NBI and HHFW (shot 128739).

the SOL. Comparisons of measurements of power deposition in the divertor regions to SOL field strike patterns for magnetic field lines passing through the SOL midplane in front of the antenna (as in Fig. RF-3) show good agreement between divertor infrared (IR) and optical camera data (IR camera views shown in Fig. RF-1). These results support the hypothesis that the HHFW power is flowing along SOL field lines and gives an indication of the RF power deposition radial profile across the SOL [RF-7, 8]. These results are important for benchmarking advanced RF codes for predicting the amount of fast-wave power coupled to the SOL [RF-9]. Fully understanding the underlying mechanisms behind this loss mechanism is critical for

Accurate numerical simulation of the interaction between fast waves and neutral-beam-injected (NBI) fast-ions is important for future fusion devices that will use a combination of neutral beam injection and fast-wave heating, such as ITER, since significant fast-ion profile broadening can result in the generation of less thermonuclear power. Fast ion profile broadening caused by HHFW heating during NBI has been measured by a 16-channel fast-ion D-alpha (FIDA) diagnostic [RF-10, 11] on NSTX. The measured FIDA spatial profile has been compared with the prediction of the synthetic diagnostic code “FIDASim” using the fast-ion distribution function from the CQL3D Fokker–Planck code [RF-12].

In an earlier study where CQL3D used a zero-banana-width (ZOW) model, CQL3D predicted a fast-ion profile that was inboard of the measured profile [RF-13]. Later CQL3D simulations used a first-order finite-orbit-width (FOW) model that calculates the bounce-average radial location of the ions versus radius, and then uses these orbit shifts to self-consistently obtain the fast-ion distribution. CQL3D simulations using this first-order FOW

model predicted a large outward radial shift, due to large orbit shifts, that was not seen in the experimental NSTX FIDA data. Recent CQL3D simulations have used a more accurate “hybrid” FOW model based on guiding center orbits. FOW features were implemented for the neutral beam source, the RF quasi-linear diffusion operator, and diagnostics. The FOW collisional operator is implemented but not applied in the FOW-hybrid calculation. Together this full feature set provides a full-orbit FOW neoclassical calculation. These latest simulations however do not include transport across the trapped-passing boundary; this feature is currently being implemented in CQL3D. A comparison of the FIDA data to the ZOW, first-order FOW, and hybrid FOW CQL3D simulations is shown in Fig. RF-4 for a case with neutral beam injection only (Fig. RF-4(a)) and with neutral beam injection and HHFW heating (Fig. RF-4(b)). Simulated FIDA data are normalized to the FIDA experimental data for the NBI only case (Fig. RF-4(a)), the same normalization factors are then used for the case with NBI and HHFW (Fig. RF-4(b)). The hybrid FOW model predicts the peak of the fast ion profile well, although the simulated profile is wider than the measured profile, especially for the case with only NBI. The predicted FIDA energy spectra, NPA energy spectra, and neutron rate are also roughly consistent with observations. Future CQL3D simulations with more accurate fast ion starting points and full banana-regime CQL3D FOW neoclassical transport may help to distribute more fast ions towards the plasma edge.

Non-Maxwellian Ion Plasma Dielectric Contributions in the HHFW version of TORIC

Ongoing experimental studies in the HHFW regime on NSTX and DIII-D have indicated that the fast ion population from neutral beam injection (NBI) is significantly modified by interactions with the HHFWs. Though the contribution of the non-Maxwellian fast ions to the plasma susceptibility was included previously in the 1D all orders METS code [RF-14] and the 2D AORSA code [RF-15], it was not yet implemented in the TORIC_HHFW code, which is utilized within the TRANPS code for time-dependent analysis of various NSTX discharges. Over the past year, various modules in the TORIC-HHFW code have been generalized to include gyrotropic but otherwise arbitrary fast ion distributions in the plasma dielectric response. As with similar calculations in AORSA [RF-15], TORIC IC [RF-16] and TORIC LH codes [RF-17], because of the large number of velocity space integrations required to generate the plasma dielectric tensor elements of a non-Maxwellian species, the dielectric tensor is pre-computed and input to TORIC, so that the field and power deposition routines need only use a look-up table for the fast ion contributions to the local plasma dielectric tensor elements. The routines are analogous to those utilized in related work in the low harmonic ICRF regime. The results of the modified plasma dielectric tensor modules for a numerically specified Maxwellian distribution function accurately reproduce the response obtained previously for an analytic Maxwellian distribution. Details of this code development were presented at the APS-DPP meeting in November 2011 [RF-18].

Continuing Studies of the Short Wavelength Slow Mode Identified in High Resolution Simulations of the HHFW and ICRF Wave fields in NSTX and C-Mod

Previous AORSA and TORIC-HHFW simulations of HHFW wave heating and current drive in NSTX have found that mode conversion to a slow wave structure is present if enough expansion elements are retained to resolve small-scale spatial structures. Simulations with these state-of-the-art full wave codes indicate that this new mode is also seen in the wave electric fields in the ICRF regime in C-Mod. Theoretical analysis indicates that the origin of the propagating slow mode can

be attributed to warm electron effects, $\omega < k_{\parallel} v_{te}$, which allow the propagation of the additional wave. In close collaboration with ORNL and the PSFC-MIT, the dependence of this mode on finite electron temperature and k_{\parallel} upshift, due in particular to the poloidal magnetic field, was verified in a range of AORSA and TORIC-HHFW simulations. Localized strong electron damping, as well as kinetic flux, was found to be associated with the new mode. In addition, the presence or absence of finite ion temperature did not have a significant effect on the structure or damping of the short wavelength mode. Though all of these features are consistent with the theoretical model, the model predicts a smaller wavelength for the mode than is found in the simulations. Furthermore, though the new slow mode appears first in the E_{\parallel} field solutions, as expected from the theoretical model, as the solution grid is further refined, it then appears in the E_{+} and E_{-} fields and the power convergence tests degrade and eventually fail. Because the mode is found in two different regimes (ICRF and HHFW) and since it is observed in the solutions of two independently written full wave codes with rather different algorithmic approaches and some differences in the underlying physics content, it is probably a real mode rather than a numerical artifact [RF-19]. More detailed comparisons will continue between the wave structure predicted by analytic models and that seen in the simulations to determine how much of the launched HHFW power may be absorbed by this mode, and identify the reason why both TORIC and AORSA have convergence difficulties at ultra high spatial resolutions when this mode is present.

NSTX-U HHFW Simulations

NSTX-U will operate with toroidal magnetic fields up to 1 T, nearly twice the value used in the experiments on NSTX. While the dominant radio-frequency heating mechanisms in NSTX were found to be Transit Time Magnetic Pumping damping on electrons and fast ion damping at high cyclotron harmonics, at the mid-harmonic range expected on NSTX-U the power partitioning may change. Initial simulations with the AORSA, TORIC, METS and GENRAY codes indicate significantly more thermal deuterium damping, in addition to NBI fast-ion damping, may occur in NSTX-U.

Figure RF-5 shows calculated power deposition from GENRAY ray tracing [RF-20] and CQL3D Fokker-Planck HHFW simulations [RF-12] that were performed on a prospective NSTX-U NBI-heated H-mode discharge. This plasma had a $B_T(0) = 1$ T, $I_p = 1.1$ MA, 6.3 MW of 90 keV NBI, $T_e(0) = 1.3$ keV, $n_e(0) = 9 \times 10^{19} \text{ m}^{-3}$ and a 0.06 m

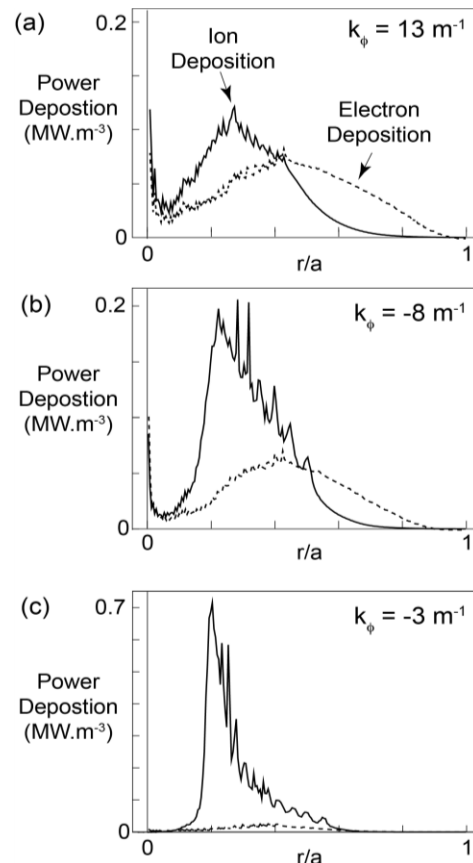


Figure RF-5: Ion (solid line) and electron (dashed line) RF power deposition profiles calculated by GENRAY/CQL3D for a NSTX-U plasma with $B_T(0) = 1$ T, $I_p = 1.1$ MA, 6.3 MW of 90 keV, $T_e(0) = 1.3$ keV, and $n_e(0) = 9 \times 10^{19} \text{ m}^{-3}$. Results are shown for (a) $k_{\phi} = 13 \text{ m}^{-1}$, (b) $k_{\phi} = -8 \text{ m}^{-1}$ and (c) $k_{\phi} = -3 \text{ m}^{-1}$ antenna phasing.

outer gap, compatible with HHFW heating. Modeling results for three antenna phasing are shown; $k_\phi = 13 \text{ m}^{-1}$ (heating antenna phasing) (Fig. RF-5(a)), $k_\phi = -8 \text{ m}^{-1}$ (Fig. RF-5(b)) and $k_\phi = -3 \text{ m}^{-1}$ (Fig. RF-5(c)) (both current drive antenna phasings). Strong single pass damping was predicted for the three antenna phasings. For $k_\phi = 13 \text{ m}^{-1}$ heating, 52% of the HHFW power was absorbed directly by electrons and 48% was absorbed by ions. For $k_\phi = -8 \text{ m}^{-1}$ heating, 35% of the HHFW power was absorbed directly by electrons and 65% was absorbed by ions. For $k_\phi = -3 \text{ m}^{-1}$ heating, only 5% of the HHFW power was absorbed directly by electrons and 95% was absorbed by ions. Simulations of HHFW heating in other NSTX-U plasma scenarios is ongoing.

First H-Mode Discharges Generated in EAST by ICRF Heating Alone

Sustained H-mode discharges produced by ICRF power alone have been produced for the first time in the EAST superconducting tokamak in China. The first H-mode plasmas generated in EAST used lower hybrid wave (LHW) heating alone and H-mode access was made possible through the extensive use of lithium-wall coatings [RF-21]. H-mode discharges had also previously been generated in EAST by a combination of LHW heating and hydrogen-minority

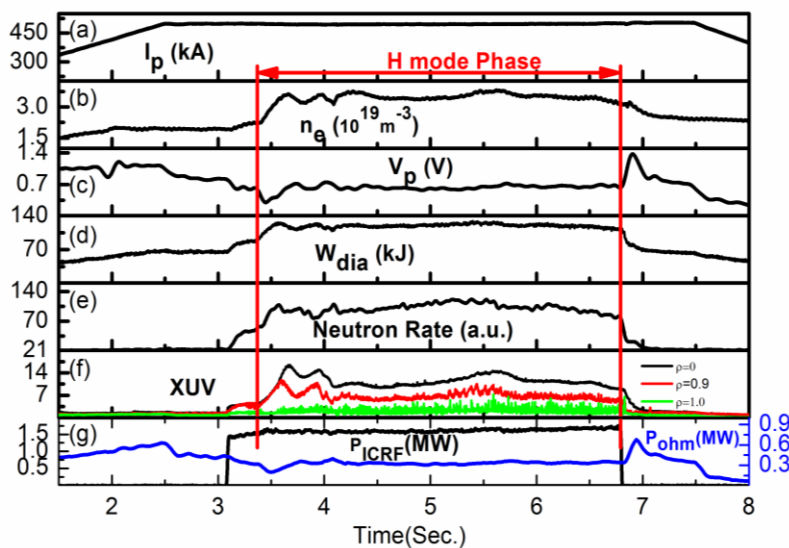


Figure RF-6: Time traces of plasma parameters for a typical H mode discharges with ICRH only. (a) plasma current, (b) the line average density, (c) the loop voltage, (d) the stored energy, (e) the neutron rate, (f) XUV radiations at $\rho = 0, 0.9$ and 1. (g) ICRF injection power. The plasma is sustained in H-mode for 3.45s.

ICRF heating, after baking the plasma facing components (PFCs) and extensive lithium wall coating reduced the hydrogen to deuterium ratio to 5-10%. LHW heating was used in these experiments to increase the electron beta and hence the ICRF power absorption. However, until recently the maximum ICRF power coupled to EAST plasmas was insufficient to generate an H-mode discharge with ICRF power alone.

On NSTX an almost fully non-inductive $I_p = 300 \text{ kA}$ deuterium H-mode plasma was generated in 2010 with only 1.4 MW of 30 MHz HHFW heating power using current drive antenna phasing and extensive lithium conditioning [RF-22]. In 2012 the NSTX HHFW team submitted an experimental proposal to EAST that aimed to produce and study H-mode plasmas generated by ICRF heating alone. While many of the goals of that proposal were not met during the ICRF experiments on EAST in 2012, these experiments did yield the first H-mode discharges heated by ICRF waves only (that is without using LHW heating). These ICRF-only H-mode discharges were sustained for up to 3.45 s (Fig. RF-6).

The H-mode phase during the longest duration H-modes was only terminated when the ICRF power was turned off. During the EAST experimental campaign 25 ICRF H-mode discharges were obtained in total [RF-23]. H-modes were only obtained in double null discharges that had an elongation of ~ 1.7 and a triangularity ~ 0.45 . H-mode plasmas with ICRF heating alone were produced in a narrow range of operation parameters, with plasma currents between 0.4 MA and 0.6 MA, line averaged density between $1.83 \times 10^{19} \text{ m}^{-3}$ and $2.35 \times 10^{19} \text{ m}^{-3}$, and axial toroidal fields between 1.85 - 1.95 T. The total ICRF power was varied from 1.6 to 1.8 MW. Note that a higher plasma density is needed for effective coupling of ICRF power into the core plasma. Normally, arcing was encountered in the RF transmission line when the line averaged plasma density was less than $1.8 \times 10^{19} \text{ m}^{-3}$. This was due to increased reflection of RF power back into the antennas causing standing waves in the transmission line.

Unlike EAST H-mode discharges generated by LHW heating alone, that exhibit a decrease of the core electron temperature, the electron temperature measured by an X-ray crystal spectrometer showed an increase of 300 eV in the plasma core of a H-mode discharge heated only by ICRF power, even though the density and radiated power loss during the H-mode phase were greatly enhanced. H-modes started with a short ELM-free period, lasting ~ 500 ms, followed by type III ELMs (Fig. RF-7(a)) with frequencies from 200 to 500 Hz (Fig. RF-7(b)).

Arcing in the transmission lines between the RF sources and the antennas was one of the main issues limiting the RF power that could be coupled into the plasma during the 2012 EAST experimental campaign. More coupled ICRF power will be required to achieve H-mode access over a wider parameter range than was possible during this first EAST ICRF H-mode campaign.

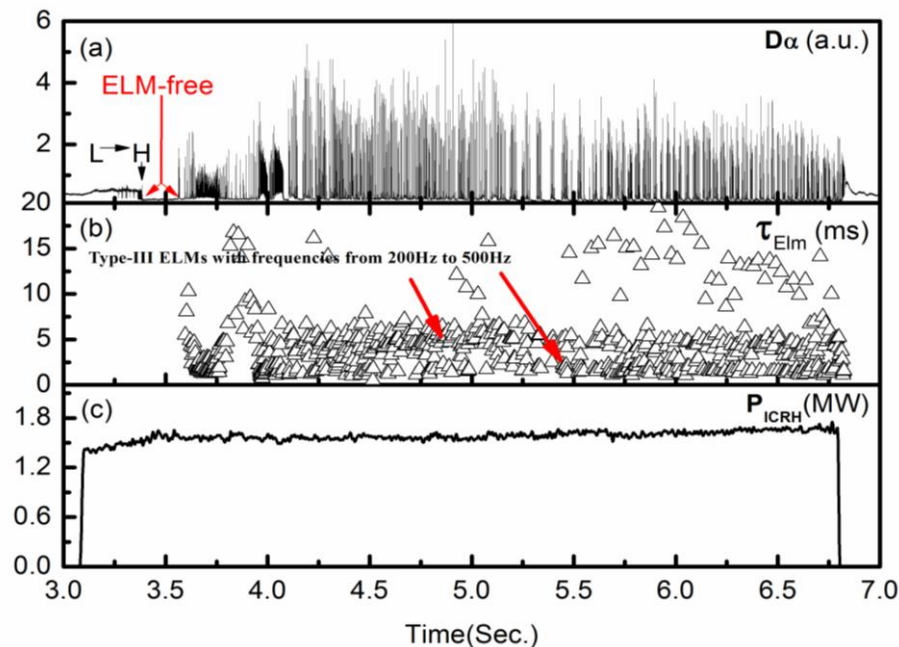


Figure RF-7: (a) D_α emission, (b) ELM repetition time and (c) ICRF heating power versus time during the ICRF-heated H-mode discharge shown in Fig. 5. Type III ELMs, with frequencies between 200 and 500 Hz, were observed during most of the H-mode phase.

EBW Modeling for a NSTX-U Advanced Scenario H-Mode Discharge

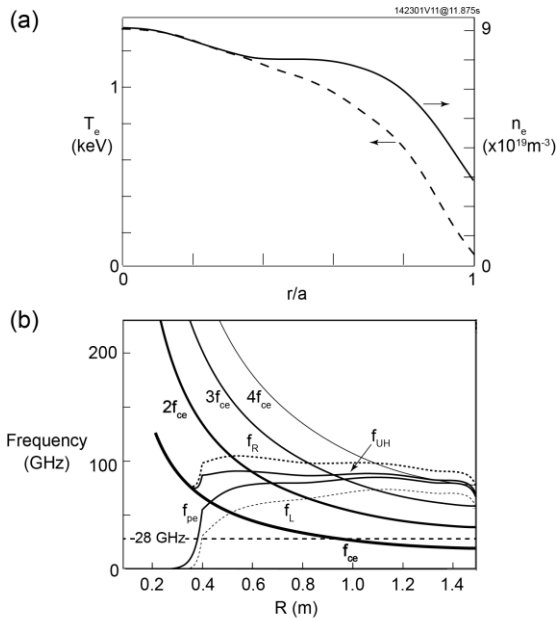


Figure RF-8: (a) Profiles of electron temperature (dashed line) and electron density (solid line) used for modeling EBW heating and current drive, and (b) electron cyclotron resonances and cutoffs for NSTX-U TRANSP run 142301V11 at 11.875 s.

TRANSP run 142301V11 at 11.875 s and the results are summarized in Fig. RF-9. The maximum O-X-B mode conversion efficiency was obtained for a poloidal angle of ± 10 degrees and a toroidal angle of ± 38 degrees, corresponding to $n_{||} = \pm 0.7$. Modeling of the EBW heating and current drive assumed a launched $n_{||} = \pm 0.7$. The EBW rays were launched at the LCFS and the vertical location of the launched rays was scanned above and below the midplane. The optimum location for providing localized heating and current drive was found between 15 and 25 degrees above and below the midplane.

Figure RF-10 summarizes GENRAY-ADJ modeling results for 1 MW of EBW power launched 20 degrees below the midplane with $n_{||} = 0.7$. EBWs propagate to just inside the magnetic axis (Fig. RF-10(a)) and travel about a third of the way toroidally around the machine (Fig. RF-10(b)). EBW power deposition peaks at $r/a \sim 0.25$. In this case the EBW-driven

A 1 MW, 28 GHz ECH system on NSTX-U is planned for installation in 2016-17. It will initially be used to heat non-inductive start-up discharges in NSTX-U. Later it will be upgraded to a 2 MW electron Bernstein wave (EBW) heating and current drive system [RF-24]. GENRAY-ADJ modeling [RF-20] was conducted for a 1.1 MA advance scenario NSTX-U H-mode plasma with an axial toroidal field of 1 T (TRANSP run 142301V11 at 11.875 s). The density and temperature profiles used for the modeling are shown in Fig. RF-8(a). The electron cyclotron resonances and cutoffs for this plasma are shown in Fig. RF-8(b). 28 GHz EBWs are resonant with f_{ce} at $R \sim 0.95$ m, close to the magnetic axis.

The O-X-B (ordinary mode to slow extraordinary mode to EBW) double mode conversion efficiency was calculated as a function of poloidal and toroidal angle for

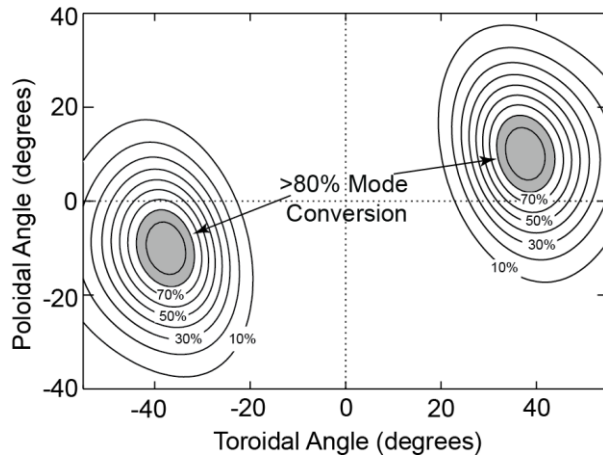


Figure RF-9: O-X-B mode conversion efficiency versus poloidal and toroidal angle for NSTX-U TRANSP run 142301V11 at 11.875 s. GENRAY-ADJ modeling was performed assuming a launched $n_{||} = \pm 0.7$, corresponding to alignment of the mirror launcher with the indicated regions of maximum mode conversion.

current is 25 kA and it is driven counter to the ohmic plasma current. Launching 20 degrees above the midplane drives a similar current but in the same direction as the ohmic plasma current. Launching the EBW power less than 10 degrees above and below the midplane resulted in little or no net current drive since the n_{\parallel} of the propagating EBWs oscillated between positive and negative values as they were absorbed, and as a result drove current in both directions. Launching the EBW power more than 30 degrees above and below the midplane resulted in large Doppler shifts, so that the EBW power was absorbed well off axis and the EBW power deposition profile became very broad.

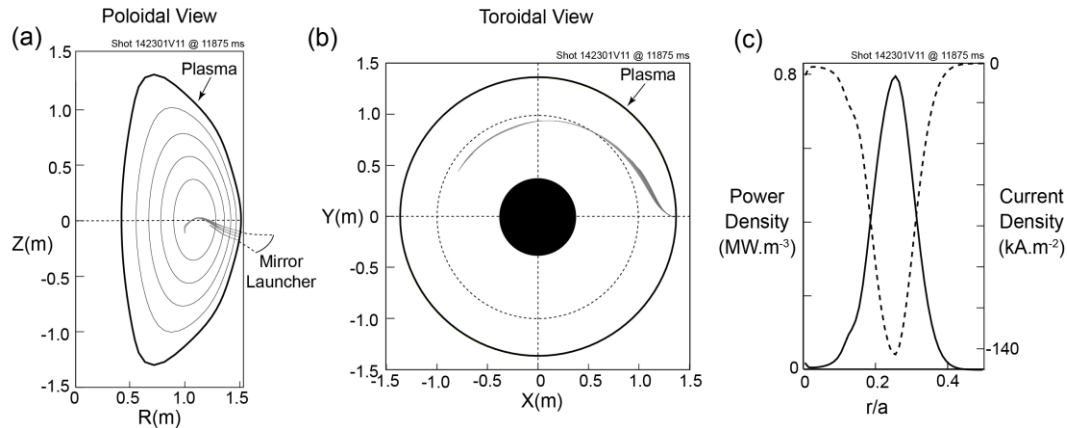


Figure RF-10: EBW ray trajectories calculated by GENRAY-ADJ plotted in (a) the poloidal and (b) the toroidal midplane for a case with maximum OXB conversion efficiency for NSTX-U TRANSP run 142301V11 at 11.875 s. EBW rays were launched 20 degrees below the midplane with $n_{\parallel} = 0.7$. (c) EBW power deposition and EBW-driven current density versus r/a calculated by GENRAY-ADJ for 1 MW of 28 GHz EBW power.

Previously B-X-O radiometric measurements on NSTX had yielded 50-60% EBW coupling efficiency from H-mode plasmas with lithium conditioning [RF-25]. The coupling efficiency significantly degraded by EBW collisional losses near the B-X-O mode conversion layer, located in the SOL, when lithium conditioning was not used. The higher magnetic field in NSTX-U should yield higher scrape off temperatures and lower EBW collisional losses, and as a result a better O-X-B coupling efficiency.

References

- [RF-1] J.C. Hosea, et al., *Phys. Plasmas* **15**, 056104 (2008)
- [RF-2] C.K. Phillips et al., *Nucl. Fusion* **49**, 075015 (2009)
- [RF-3] J.C. Hosea et al., *AIP Conf Proceedings* **1187**, 105 (2009)
- [RF-4] G. Taylor et al., *Physics of Plasmas* **17**, 056114 (2010)
- [RF-5] J.C. Hosea, et al., *AIP Conf. Proceedings* 1406, 333 (2011)
- [RF-6] R.J. Perkins et al., *Phys. Rev. Lett.* **109**, 045001 (2012)
- [RF-7] R.J. Perkins, et al., *Proc. 39th EPS Conf. on Plasma Physics* **36F** (Stockholm 2012) paper P-1.011
- [RF-8] R.J. Perkins, et al., *IAEA Fusion Conference* (San Diego 2012)
- [RF-9] D.L. Green, et al., *Phys. Rev. Lett.* **107**, 145001 (2011)
- [RF-10] W.W. Heidbrink, et al., *Rev. Sci. Instrum.* **77**, 10F120 (2006)

- [RF-11] M. Podesta, et al., *Rev. Sci. Instrum.* **79**, 10E521 (2008)
- [RF-12] R.W. Harvey and M.G. McCoy *Proc. IAEA Technical Committee Meeting on Advances in Simulation and Modeling of Thermonuclear Plasmas* (Montreal 1992) (Vienna: IAEA)
- [RF-13] D. Liu, et al., *Plasma Phys. and Control. Fus.* **52**, 025006 (2010)
- [RF-14] R.J. Dumont, C. K. Phillips and D.N. Smithe, *Phys. Plasmas* **12**, 042508 (2005)
- [RF-15] E.F. Jaeger, et al., *Phys. Plasmas* **13**, 056101 (2006)
- [RF-16] E.J. Valeo, et al., <http://meetings.aps.org/link/BAPS.2006.DPP.VP1.47>
- [RF-17] E.J. Valeo, et al., *Radio Frequency Power in Plasmas: Proc. of the 17th Topical Conference. AIP Conf Proc.* **933**, [AIP, NY, 2007], p. 297
- [RF-18] N. Bertelli, et al., <http://meetings.aps.org/link/BAPS.2011.DPP.NP9.64>
- [RF-19] C.K. Phillips, et al., *Radio Frequency Power in Plasmas: Proc. of the 19th Topical Conference, AIP Conf Proc.* **1406**, (AIP, NY, 2011) p. 341
- [RF-20] A. P. Smirnov, et al., *Proc. 15th Workshop on ECE and ECRH*, (World Scientific 2009), p. 301
- [RF-21] G.S. Xu, et al., *Nucl. Fusion* **51**, 072001 (2011)
- [RF-22] G. Taylor, et al., *Phys. Plasmas* **19**, 042501 (2012)
- [RF-23] Y.P. Zhao, et al., “*First Results from H-Mode Plasmas Generated by ICRF Heating Alone in the EAST Superconducting Tokamak*”, to be submitted to *Nucl. Fusion Lett.* (2012)
- [RF-24] G. Taylor, et al., *Proc. 17th Workshop on ECE ECRH*, (EPJ Web of Conferences 2012) **32**, 02014 <http://www.epj-conferences.org/>
- [RF-25] S.J. Diem, et al., *Phys. Rev. Lett.* **103**, 015002 (2009)

Advanced Scenarios and Control

Modeling of Equilibrium Scenarios for NSTX-U

Analysis was completed and a paper published [ASC-1] exploring a range of high-performance equilibrium scenarios achievable with neutral beam heating in the NSTX-Upgraded [ASC-2] device. NSTX-Upgraded is a substantial upgrade to the existing NSTX device [ASC-3], with significantly higher toroidal field and solenoid capabilities, and three additional neutral beam sources with significantly larger current-drive efficiency. Equilibria were computed with free-boundary TRANSP, allowing a self-consistent calculation of the non-inductive current-drive sources, the plasma equilibrium and poloidal-field coil currents, using the realistic device geometry. The thermal profiles are taken from a variety of existing NSTX discharges, and different assumptions for the thermal confinement scalings are utilized. The no-wall and ideal-wall $n = 1$ stability limits are computed with the DCON code. The central and minimum safety factors are quite sensitive to many parameters: they generally increase with large outer plasma-wall gaps and higher density, but can have either trend with the confinement enhancement factor. In scenarios with strong central beam current drive, the inclusion of non-classical fast-ion diffusion raises q_{\min} , decreases the pressure peaking, and generally improves the global stability, at the expense of a reduction in the non-inductive current-drive fraction; cases with less beam current drive are largely insensitive to additional fast-ion diffusion. The non-inductive current level is quite sensitive to the underlying confinement and profile assumptions. For instance, for $B_T = 1.0$ T and $P_{\text{inj}} = 12.6$ MW, the non-inductive current level varies from 875 kA with ITER-98y,2 thermal confinement scaling and narrow thermal profiles to 1325 kA for an ST specific scaling expression and broad profiles. Scenarios are presented which can be sustained for 8–10 s, or 20–30 τ_{CR} , at $\beta_N = 3.8$ –4.5. The value of q_{\min} can be controlled at either fixed non-inductive fraction of 100% or fixed plasma current, by varying which beam sources are used, opening the possibility for feedback control of the current profile. In terms of quantities like collisionality, neutron emission, non-inductive fraction, or stored energy, these scenarios represent a significant performance extension compared with NSTX and other present spherical torii.

References

- [ASC-1] S.P. Gerhardt, et al., Nucl. Fusion **52** (2012) 083020
- [ASC-2] J.E. Menard, et al., Nucl. Fusion **52** (2012) 083015
- [ASC-3] M. Ono, et al., Nucl. Fusion **40** (2000) 557

Steps Toward More Accurate Predictions of Vertical Instability Growth Rates in NSTX

Studies of NSTX control have focused on understanding discrepancies between calculated and experimentally derived growth rates. The growth rate of a VDE can be predicted by the plasma response codes rzig and Gspert [PC-1] which are part of the GA TokSys computational environment for control design and analysis. Gspert is a nonrigid plasma response model based on the linearized Grad-Shafranov equation. For DIII-D, these predictions have been in very good agreement with observed growth rates after triggered VDE's for a range of growth rates. However, for VDE's in NSTX the same codes predict values that are 3 times smaller than

observed. One of the reasons for the observed discrepancy, and possibly the most significant, can be that the models make incorrect assumptions about how the current and pressure profiles are affected when the applied flux changes. Figure PC-1 is an example of predictions made by Gspert. The example shows the flux at a point named “isoflux point 5”, which is an arbitrary point on the boundary.

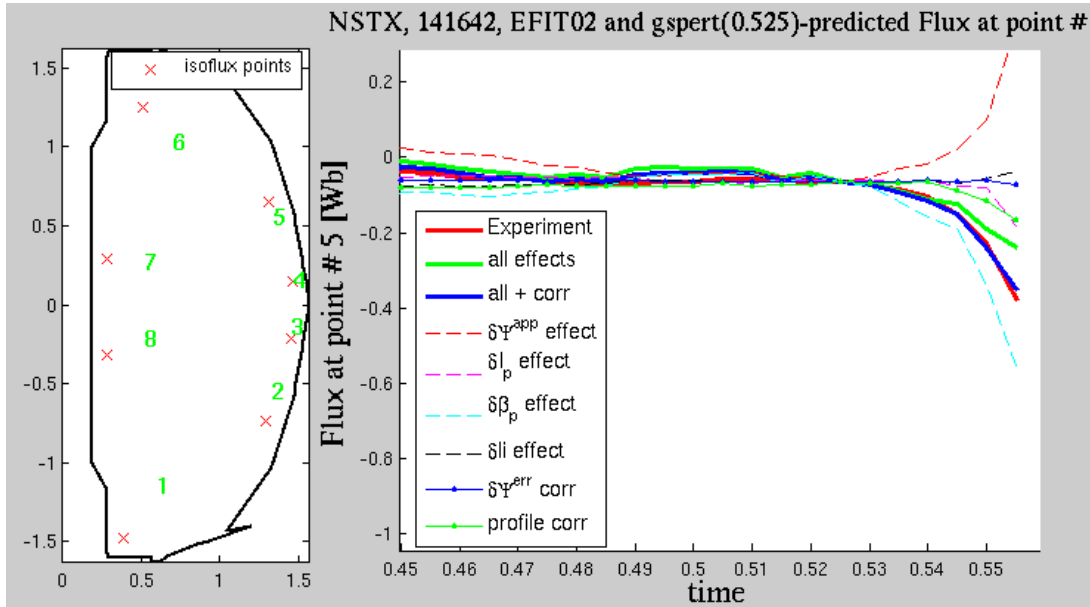


Figure PC-1: Validation of NSTX isoflux response during a VDE using Gspert and EFIT.

In this plot RED is the EFITs from the experiment, GREEN is Gspert predictions, BLUE is Gspert prediction with corrections for profile variation and convergence errors, dashed lines are individual effects from applied flux, li, betap, ip, dashed lines with diamonds show effects from profile variations and convergence errors. The two remaining sources for discrepancies between Gspert predictions and EFITs are due to the finite grid size and non-linearities in the plasma response. These are not shown. The VDE occurs at 0.53 seconds in the shot. As can be seen, the Gspert prediction in green is slower than the EFITs from the experiment in red. The blue line with Gspert prediction corrected for details of the profile behavior is in good agreement with EFIT. The Gspert model is usually calculated with the assumption that li, betap, ip are unaltered by perturbations of the applied flux (with specific recipes for the details of the profiles). Any changes of these quantities are regarded as external influences, and shown by the dashed lines in Figure PC-1. If a model is developed that correctly includes the detailed response of the current and pressure profiles to changes in the applied flux then the prediction in blue would follow without the addition of any “external influences” and the growth rate should therefore be correctly predicted.

In addition to the Gspert calculations, the free-boundary equilibrium and transport code Corsica [PC-2] has also been used for NSTX vertical stability calculations for benchmarking purposes. Such benchmarking is important, since NSTX vertical plasma motion shows non-linear characteristics in agreement with previous spherical tokamak data from MAST. Figure PC-2

shows the result of comparison between the simulations and the experimental data. There is a large error bar in the growth-rate calculations due to the uncertainty that results from fitting an exponential curve to the experimental data.

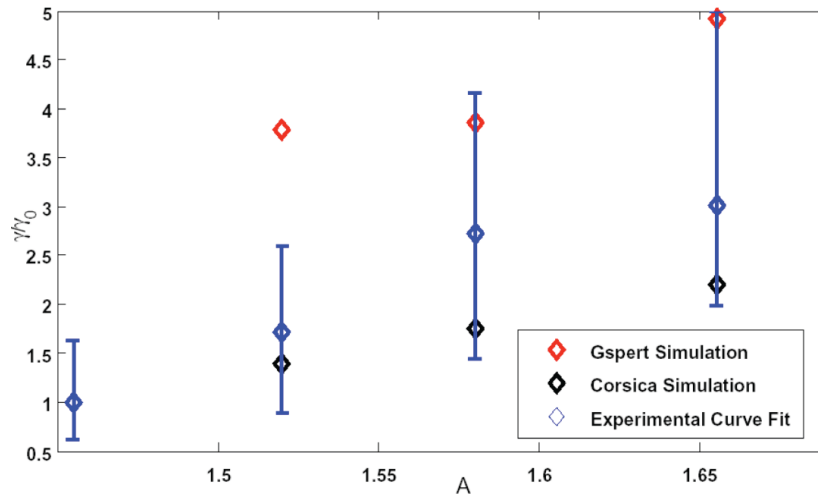


Figure PC-2: NSTX VDE growth rate versus aspect ratio for Gspert and Corsica simulations and for experiment (shots 141639-141642)

While the error bars are large, both the experimental data and the simulations show a clear trend in the increase in the growth rate as an increase in A. The statistical analysis of the NSTX-U vertical motion via Gspert and Corsica simulations is obtained based on the results from the NSTX data. The controllability of the VDEs for a variety of parameters is assessed for NSTX-U under the current control algorithm. Results of these studies show that since NSTX-U will be operating at higher A, the vertical growth-rate will be higher, which in turn will make control more difficult. Also, the acceleration in the growth-rate as the plasma drifts as shown in Figure PC-3 leads to the prioritization of early detection and faster control over more control power.

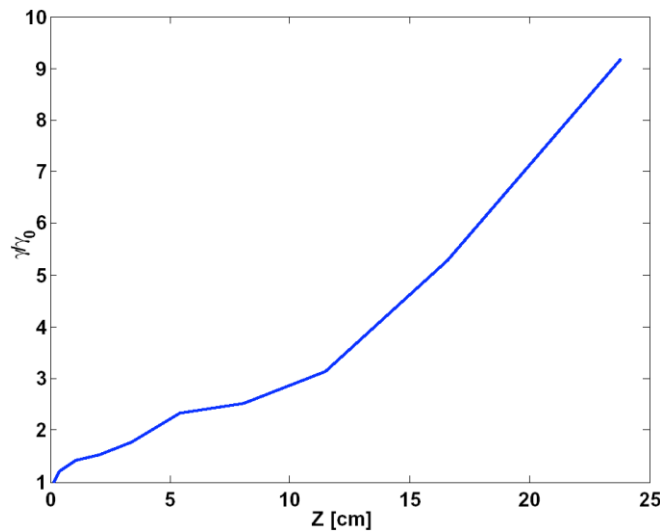


Figure PC-3: VDE grow-rate versus the displacement in the plasma vertical location (#127077)

With these considerations in mind, there are currently three improvements planned for the NSTX-U. First, a new, more sophisticated vertical position estimator will enable early and more accurate detection. Second, RWM coils, which are much faster than the poloidal field coils, were put in the vertical control loop, which will reduce control action delay against VDEs. Improvements to the control algorithm are also under development.

NSTX Inboard Midplane Gap Controllability Study

The effectiveness of the NSTX PF coil-set for gap control has been assessed using recently revalidated system and plasma response models. The assessment was done using a “decoupling” controller, produced by inverting the mapping matrix from coil currents to isoflux errors and plasma current. Figure PC-4 shows that this decoupling matrix controller produces poor decoupling of the inboard midplane gap (isoflux segment 7 in Figure PC-1) error, and even this poor degree of decoupling requires unrealistically large coil current variation from the equilibrium values.

A key result of the recent model validation process is that the representation of experimental response appears accurate enough to enable reasonable calculation of high order matrix controllers produced using the decoupling approach or other model-based design method.

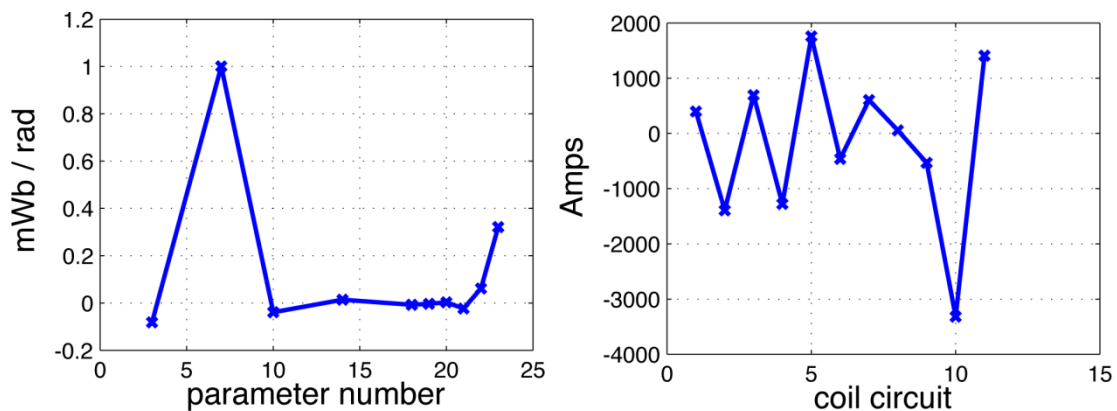


Figure PC-4. Errors corresponding to best decoupling of isoflux segment 7 (inboard midplane gap) from other isoflux segments and corresponding coil current vector.

References

- [PC-1] Welander et al., 52nd APS/DPP Meeting, Chicago, Illinois, 8-12 Nov., 2010
- [PC-2] Lodestro and Pearlstein, Phys. Plasmas 1 (1994) 90

NSTX-U Publications in FY2012 (October 2011-September 2012)

- 1) Gerhardt SP, Fredrickson E, Guttadora L, et al
Techniques for the measurement of disruption halo currents in the National Spherical Torus Experiment
REVIEW OF SCIENTIFIC INSTRUMENTS 82 (10) 103502 (October 2011)
- 2) Hong BG, Hwang YS, Kang JS, et al
Conceptual design study of a superconducting spherical tokamak reactor with a self-consistent system analysis code
NUCLEAR FUSION 51 (11) 113013 (October 2011)
- 3) Raman R, Jardin SC, Menard J, et al
Transient CHI start-up simulations with the TSC
NUCLEAR FUSION 51 (11) 113018 (October 2011)
- 4) Kaye SM, Maingi R, Battaglia D, et al
L-H threshold studies in NSTX
NUCLEAR FUSION 51 (11) 113019 (October 2011)
- 5) Kolemen E, Gates DA, Gerhardt SP, et al.
Plasma modelling results and shape control improvements for NSTX
Nucl. Fusion 51 113024 (November 2011)
- 6) GERHARDT SP, Mastrovito D, Bell M et al.
Implementation of beta(N) control in the National Spherical Torus Experiment
Fusion Science and Technology 61 11 (January 2012)
- 7) PARK J-K, Menard JE, Gerhardt SP et al.
Sensitivity to error fields in NSTX high beta plasmas
Nucl. Fusion 52 023004 (January 2012)
- 8) GUTTENFELDER W, Candy J, Kaye SM, et al
Scaling of linear microtearing stability for a high collisionality National Spherical Torus Experiment discharge
Phys. Plasmas 19 022506 (February 2012)
- 9) PODESTÀ M, Bell RE, Diallo A, et al.
Measurements of core lithium concentration in a Li-conditioned tokamak with carbon walls
Nucl. Fusion 52 033008 (March 2012)

- 10) ONO M, Bell MG, Hirooka Y, et al.
Conference Report on the 2nd International Symposium on Lithium Applications for Fusion Devices
Nucl. Fusion 52 037001 (March 2012)
- 11) HEIM B, Gonderman S, Taylor CN, et al.
The Materials Analysis particle Probe (MAPP) Diagnostic System in NSTX
IEEE Transactions on plasma science 40 735 (March 2012)
- 12) PODESTÀ M and Bell RE
A real-time velocity diagnostic for NSTX
Rev. Sci. Instrum. 83 033503 (March 2012)
- 13) FREDRICKSON ED, Gorelenkov NN, Belova E, et al.
Observation of global Alfvén eigenmode avalanche events on the National Spherical Torus Experiment
Nucl. Fusion 52 043001 (March 2012)
- 14) TAYLOR G, Hosea JC, Kessel CE, et al.
High non-inductive fraction H-mode discharges generated by high-harmonic fast wave heating and current drive in the National Spherical Torus Experiment
Phys. Plasmas 19, 042501 (April 2012)
- 15) GUTTENFELDER W, Candy J, Kaye SM, et al
Simulation of microtearing turbulence in the National Spherical Torus Experiment discharge
Phys. Plasmas 19 056119 (April 2012)
- 16) MYRA JR, Russell DA, D'Ippolito DA
Diffusive–convective transition for scrape-off layer transport and the heat-flux width
Plasma Phys. Controlled Fusion 54 055008 (April 2012)
- 17) GERHARDT SP, Menard J, Sabbagh S, et al.
Characterization of disruption halo currents in the National Spherical Torus Experiment
Nucl. Fusion 52 063005 (April 2012)
- 18) PETERSON JL, Bell RE, Candy J et al.
Suppressing electron turbulence and triggering internal transport barriers with reversed magnetic shear in the National Spherical Torus Experiment
Phys. Plasmas 19 056119 (May 2012)
- 19) REN Y, Guttenfelder W, Kaye SM, et al.
Experimental study of parametric dependence of electron-scale turbulence in a spherical tokamak
Phys Plasmas 19 056125 (May 2012)

- 20) ALLAIN JP, Taylor CN
Lithium-based surfaces controlling fusion plasma behavior at the plasma-material interface
Phys. Plasmas 19 056126 (May 2012)
- 21) CANIK JM, Hirshman SP, Sanchez R, et al.
First use of three-dimensional equilibrium, stability and transport calculations for interpretation of ELM triggering with magnetic perturbations in NSTX
Nucl. Fusion 52 054004 (May 2012)
- 22) LORE JD, Canik JM, Feng Y, et al.
Implementation of the 3D edge plasma code EMC3-EIRENE on NSTX
Nucl. Fusion 52 054012 (May 2012)
- 23) KUMAR D, Finkenthal M, Stutman D, et al.
Impurity analysis of NSTX using a transmission grating-based imaging spectrometer
Plasma Phys. Controlled Fusion 54 065010 (May 2012)
- 24) La HAYE RJ, Buttery RJ, Gerhardt SP, et al.
Aspect ratio effects on neoclassical tearing modes between DIII-D and NSTX
Phys. Plasmas 19 062506 (June 2012)
- 25) A.G. McLean AG, J-W. Ahn J-W, R. Maingi R, et al.
A dual-band adaptor for infrared imaging
Rev. Sci. Instrum. 83 053706 (June 2012)
- 26) MAINGI R, Boyle DP, Canik JM, et al.
The effect of progressively increasing lithium coatings on plasma discharge characteristics, transport, edge profiles and ELM stability in the National Spherical Torus Experiment
Nucl. Fusion 52 083001 (June 2012)
- 27) SMITH DR, Fonck RJ, McKee GR, et al.
Diagnostic performance of the beam emission spectroscopy system on the National Spherical Torus Experiment
Rev. Sci. Instrum. 83 10D502 (June 2012)
- 28) TAYLOR CN, Heim B, Gonderman S, et al.
Materials analysis and particle probe: A compact diagnostic system for in situ analysis of plasma-facing components (Invited)
Rev. Sci. Instrum. 83 10D703 (June 2012)
- 29) RAMAN R, Mueller D, Jardin SC et al.
Transient CHI Plasma Start-up in NSTX and CHI Program Plans on NSTX-U
IEEJ Transactions on Fundamentals and Materials 132 462 (July 2012)

- 30) RAMAN R., Stotler DP, Abrams T, et al.
Massive Gas Injection Plans for Disruption Mitigation Studies in NSTX-U
IEEJ Transactions on Fundamentals and Materials 132 468 (July 2012)
- 31) Perkins RJ, Hosea JC, Kramer GJ, et al.
High-harmonic fast-wave power flow along magnetic field lines in the scrape-off layer of NSTX
Phys. Rev. Lett. 109 045001 (July 2012)
- 32) MENARD JE, Gerhardt S, Bell MG, et al.
Overview of the physics and engineering design of NSTX upgrade
Nucl. Fusion 52 083015 (July 2012)
- 33) SKINNER CH, Gentile CA, and Doerner R
Simultaneous imaging/reflectivity measurements to assess diagnostic mirror cleaning
Rev. Sci. Instrum. 83 10D512 (July 2012)
- 34) CLAYTON DJ, Jaworski MA, Kumar D, et al.
Divertor electron temperature and impurity diffusion measurements with a spectrally resolved
imaging radiometer
Rev. Sci. Instrum. 83 10D521 (July 2012)
- 35) LeBLANC BP, Diallo A, Labik G, et al.
Radial resolution enhancement of the NSTX Thomson scattering diagnostic
Rev. Sci. Instrum. 83 10D527 (July 2012)
- 36) SOUKHANOVSII VA, Gerhardt SP, Kaita R, et al.
Diagnostic options for radiative divertor feedback control on NSTX-U
Rev. Sci. Instrum. 83 10D716 (July 2012)
- 37) TRITZ K, Clayton DJ, Stutman D, et al.
Compact “diode-based” multi-energy soft x-ray diagnostic for NSTX
Rev. Sci. Instrum. 83 10E109 (July 2012)
- 38) SOUKHANOVSII VA, Bell RE, Diallo A, et al.
Snowflake divertor configuration studies in National Spherical Torus Experiment
Phys. Plasmas 19 082504 (August 2012)
- 39) DIALLO A, LeBlanc BP, Labik G, et al.
Prospects for the Thomson scattering system on NSTX-Upgrade
Rev. Sci. Instrum. 83 10D532 (August 2012)

- 40) SCOTTI F, Roquemore AL and Soukhanovskii VA
Full toroidal imaging of non-axisymmetric plasma material interaction in the National Spherical Torus Experiment divertor
Rev. Sci. Instrum. 83 10E532 (August 2012)
- 41) KIM K, Park J-K, Kramer GJ, et al.
 δf Monte Carlo calculation of neoclassical transport in perturbed tokamaks
Phys. Plasmas 19 082503 (August 2012)
- 42) Manickam J, Boozer A and Gerhardt SP
Kink modes and Surface currents associated with vertical displacement events
Phys. Plasmas, Vol. 19 082103 (August 2012)
- 43) S.P. Gerhardt, R. Andre and J.E. Menard
Exploration of the equilibrium operating space for NSTX-Upgrade
Nucl. Fusion 52 083020 (August 2012)
- 44) PODESTA M, Bell RE, Bortolon A et al.
Study of chirping toroidicity-induced Alfvén eigenmodes in the National Spherical Torus Experiment
Nucl. Fusion 52 094001 (September 2012)
- 45) ZWEBEN SJ, Campanell MD, Lyons BC, et al.
Local effects of biased electrodes in the divertor of NSTX
Plasma Phys. Cont. Fusion 54 105012 (September 2012)
- 46) Clayton DJ, Tritz K, Stutman D, et al.
Multi-energy soft-x-ray technique for impurity transport measurements in the fusion plasma edge
Plasma Phys. Control. Fusion 54 105022 (September 2012)